Evolution of Size Independent Fracture Energy through Characterization of Fracture Process Zone in Concrete Structures

By

Neha Trivedi

(Enroll. No. ENGG01201204016)

Bhabha Atomic Research Centre, Mumbai, India

A thesis submitted to the Board of Studies in Engineering Sciences
In partial fulfillment of the requirements
for the Degree of

DOCTOR OF PHILOSOPHY

of

HOMI BHABHA NATIONAL INSTITUTE

May 2016

Homi Bhabha National Institute

STATEMENT BY AUTHOR

This dissertation has been submitted in partial fulfillment of requirements for an advanced degree at Homi Bhabha National Institute (HBNI) and is deposited in the library to be made available to borrowers under rules of the HBNI.

Brief quotations from this dissertation are allowable without special permission, provided that accurate acknowledgement of source is made. Requests for permission for extended quotation from or reproduction of this manuscript in whole or in part may be granted by the Competent Authority of HBNI when in his or her judgment the proposed use of the material is in the interests of scholarship. In all other instances, however, permission must be obtained from the author in writing.

Neha Trivedi

DECLARATION

I, hereby declare that the investigation presented in the thesis has been carried out by me. The work is original and has not been submitted earlier as a whole or in part for a degree / diploma at this or any other institution / University.

Neha Trivedi

List of Publications arising from the thesis

International Journal: 04

1. Size independent fracture energy evaluation for plain cement concrete. N. Trivedi, R. K. Singh and J. Chattopadhyay. *Fatigue and Fracture of Engineering Materials and Structures*. **2015**. 38. 789-798.

2. Characterization of concrete specimen fracture response: 2D numerical study. N. Trivedi, R. K. Singh and J. Chattopadhyay. *Structures*. **2015**. 1. 39-50.

3. A comparative study on three approaches to investigate the size independent fracture energy of concrete. N. Trivedi, R. K. Singh and J. Chattopadhyay. *Engineering Fracture Mechanics*. **2015**. 138. 49-62.

4. Investigation on fracture parameters of concrete through Optical Crack Profile (OCP) and size effect studies. N. Trivedi, R. K. Singh and J. Chattopadhyay. *Engineering Fracture Mechanics*. **2015**. 147. 119-139.

International Conference: 02

1. Size Independent Concrete Fracture Energy Investigation. N. Trivedi, R. K. Singh and J. Chattopadhyay. 5th *International Congress on Computational Mechanics and Simulation* (ICCMS).10-13 December. **2014**. SERC Chennai. India.

2. Numerical Modelling For Characterizing Concrete Fracture Parameters. N. Trivedi, R. K. Singh and J. Chattopadhyay. 5th *International Congress on Computational Mechanics and Simulation* (ICCMS). 10-13 December. **2014**. SERC Chennai. India.

Neha Trivedi

DEDICATIONS

I dedicate this thesis to

My grandmothers

Late Smt. Kanti Devi Trivedi and Late Smt. Uma Agnihotri

ACKNOWLEDGEMENT

First and foremost, I express my sincere regards and deep sense of gratitude to my research guide Prof. Ram Kumar Singh, former Associate Director, Reactor Design and Development Group, whom I have been associated right from day one of my professional career. Without his support, work of this magnitude would have been difficult to undertake and finish. He willingly took the pain, shouldered the responsibility of providing me guidance despite the day-to-day office activities and encouraged me to pursue my research interests. I am extremely thankful to my co-guide Prof. J. Chattopadhyay, Reactor Safety Division for his invaluable suggestions emanating from several discussions and his able guidance has finally ensured that this research work sees the light of the day. I thank both of them for their keen interest, constructive suggestion, valuable guidance in hours of need, constant encouragement, and motivation throughout my entire research tenure. I am also grateful to them for critically reviewing this thesis. This work would not have been possible without their enthusiastic involvement in every aspect of it. They have been a source of great inspiration who always advised me to maintain a balance between academic interest and the application aspects of new research.

It gives me immense pleasure to acknowledge my doctoral committee chairman Prof. G. R. Reddy, Head, Structural and Seismic Engineering Section, Reactor Safety Division, for constant support and for critically evaluating my research activities time to time. I greatly acknowledge the contributions of the doctoral committee members Dr. D. C. Kar, Dr. K. Bhargava and Dr. A. Vinod Kumar who spared their valuable time for periodical critical assessment of my work.

I gratefully acknowledge the help rendered by all my colleagues and friends of Reactor Design and Development Group. My special thanks are due to Mr. S. Raviprakash, MD and CEO, Pyrodynamics-Bengaluru, Prof. B. K. Raghuprasad, IISc Bangalore and Dr. S. Muralidhara, BMS College of Engineering-Bangalore for their invaluable guidance.

I am thankful to all the reviewers of my published papers whose comments on my manuscript always upgraded my scientific thought and led me toward a novel way of thinking. Though they may never know, I would like to thank all those researchers whose publications provided useful information and understanding related to my research problem. I thank with apology all those people whose contributions to this work have escaped my attention and, thus, have gone unnoticed. Direct or indirect support received from BARC-Mumbai and IISc-Bangalore is gratefully acknowledged.

Finally, big thanks to my family for always being there for me. Without their constant support I would have not been able to concentrate and complete my work. Sincere gratitude and indebtedness to my parents, mother in law, brother and sister for their blessings, love and support to me. I am extremely thankful to my spouse Mr. Sudhanshu Pandey for understanding and continuous support to complete the thesis. Thanks are due to all my family members and friends for their support, and continuous encouragement during my research period.

Neha Trivedi

CONTENTS

Abstract

Fracture in concrete, results from the coalescence of micro-cracks and formation of a Fracture Process Zone (FPZ) and further development of macro-cracks leading to fracture propagation. The size of the FPZ in front of an existing crack or notch determines the extent of energy dissipated during fracture. Studies on the concrete fracture energy, FPZ, the behavior of concrete during fracture process and size effect are at the forefront of research on concrete fracture. The main objective of this study is to present various approaches for the investigation of the size independent fracture energy (G_F) of concrete and characteristics of FPZ to address the important features of crack formation and its propagation in quasi-brittle material like concrete. This study leads to establish a size independent fracture energy that can be used as a material parameter in the numerical analysis of concrete structures.

The fracture energy and FPZ are the most useful parameters for characterizing the fracture behavior and analysis of concrete structures. The numerical modelling of Three Point Bend (TPB) concrete beams that are geometrically similar having constant length to depth ratio with varying range of notch to depth (a/D) ratios is performed. The unique non-linear behavior of concrete material is incorporated through fracture energy based softening model in the finite element numerical simulation. In the numerical study of concrete components, mesh sensitivity is an extremely important issue, which has been addressed in this work. In the present finite element analysis of TPB fracture test, the performance of triangular elements is investigated and observed to be superior over the quadrilateral elements for fracture analysis. The RILEM fracture energy (G_f) values evaluated by load-load line displacement responses obtained experimentally and through the numerical simulation of several set of experiments are beset with size effects. G_f values are utilized to determine G_F by Hu and Wittmann method based on bilinear model. In

addition, the fact as reported in literature that ratio of fracture energy to the uncracked ligament length almost becomes constant at larger uncracked ligament lengths is proved in this study. Further, relationship based on fracture energy release rate is developed to assess the G_F. Another methodology based on averaging of G_f values associated with geometrically similar beams, is developed for the evaluation of size independent fracture energy of concrete.

The fracture parameters through Bazant's size effect studies and Jenq-Shah size effect law are investigated. FPZ is visualized for notched concrete beams under bending using a testing scheme called Digital Image Correlation (DIC). A new approach known as Optical Crack Profile (OCP), based on DIC experiments, is proposed to quantify the fracture parameters such as crack opening displacement, width of FPZ, length of FPZ and fracture energy. A comprehensive analysis of fracture energy estimated from various methodologies such as bilinear model, fracture energy release rate, G_f averaging for geometrically similar beams, Bazant size effect laws, Jenq-Shah model and OCP technique have been carried out to obtain a unique value of the size independent fracture energy of concrete.

List of Figures

List of Tables

Nomenclatures

a	Notch length in three point bend beam
b	Exponential constant of energy release rate function
C	Constant of energy release rate function
D	Depth of three point bend beam
E	Modulus of elasticity of concrete
S	Span of three point bend beam
t	Thickness of three point bend beam
u	Displacement component in X direction
v	Displacement component in Y direction
w	Crack opening displacement
a_c	Notch depth of beam at maximum load P_c
Bf_{t}	Empirical parameter identified by optimum fitting of measured σ_{Nu}
c_f	Effective length of fracture process zone
c_n	Dimensionless coefficient
d_a	Maximum size of aggregate in mm
D_0	Empirical parameter identified by optimum fitting of measured σ_{Nu}
f_{ck}	Compressive strength of concrete
f_t	Tensile strength of concrete
g_f	Local fracture energy at crack tip
G_f	RILEM fracture energy
G_F	Size independent fracture energy
K_{Ic}	Critical stress intensity factor/ Fracture Toughness

P_c	Peak/fracture load of beam
w_c	Critical crack opening displacement
W_h	Self-weight of the beam
α	Notch to depth ratio of three point bend beam
δ	Load point displacement
ν	Poisson's ratio
σ	Bridging stress
α_0	Ratio of initial notch depth to beam depth
γ_{xy}	Shear strain
ε_x	Strain in X direction
ε_y	Strain in Y direction
σ_{Nu}	Nominal strength of structure for maximum load P_c

Abbreviations

COD	Crack Opening Displacement
CST	Constant Strain Triangular Element
FEA	Finite Element Analysis
FPZ	Fracture Process Zone
OCP	Optical Crack Profile
RILEM	International Union of Laboratories and Experts in Construction Materials, Systems and Structures
TPB	Three Point Bend

Chapter 1

INTRODUCTION

1.1 Fracture mechanics approach

As is well known that concrete is the most commonly used building material in the world for most of the civil engineering structures because of their beneficial fire rating, long service life under normal and accidental conditions and ease in construction with relatively lower cost; in addition they are suitable for nuclear industry due to excellent shielding capability. In-spite of such salient features, the concrete structures generally consist of pores, air voids and shrinkage cracks that create the inherent flaws/micro-cracks and affect the performance of concrete structures. The numerous micro-cracks might result in fracture of the concrete structures under service loads, accidental load and/or exposure to regular environmental conditions and at times harsh environmental conditions. Thus a micro-crack in concrete may become a potential source of crack propagation leading to a probable catastrophic failure. In order to prevent such accidents, it is necessary to predict the failure mechanisms of structures, so that the safety of concrete structures throughout the service life can be assured. The failure mechanism can be studied by quantifying the energy dissipated in crack propagation and formation of new crack surfaces. Fracture mechanics based on energy criterion provides a fundamental basis for understanding the phenomenon of concrete fracture. In a concrete structure, the crack growth requires a certain amount of energy that can only be studied through an energy based propagation criterion, which provides a fundamental basis for understanding the phenomenon of concrete fracture mechanism. The fracture results in complex cracking zone characterized by the failure mechanisms like micro-crack shielding, aggregate bridging, crack deflection, crack tip blunting, crack closure induced by surface roughness and crack branching as shown in **Fig. 1.1**. These mechanisms are also known as toughening mechanism.

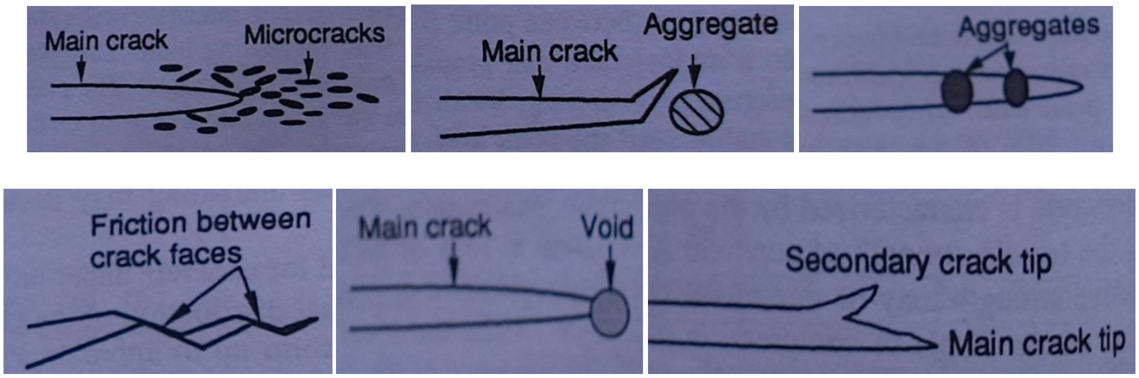

Fig. 1.1 Toughening mechanism showing: Crack shielding, crack deflection, aggregate bridging, crack surface roughness induced closure, crack tip blunted by void and crack branching [**Shah et. al. (1995)**]

The toughening mechanisms can be reasonably quantified by the dissipated energy during the fracture process of concrete. Due to anisotropic and heterogeneous nature of concrete, the cracking should be described through the energy criteria. Even though cracks play an important role, concrete structures have been successfully designed and built without any use of fracture mechanics. The risk in the current design practice for concrete structures is that inherent flaws in the material might grow under loading to unacceptable lengths. It is therefore, imperative that necessary steps should be taken to enhance the current understanding and improve the design practices associated with concrete in order to reliably account for the possible failure mechanisms, which could be achieved by introducing the fracture mechanics concepts. The major reasons for the application of fracture mechanics to concrete are as follows **[Shah et. al. (1995), Bazant** and **Planas (1998),** and **Shailendra** and **Barai (2011)]**:

(i) In a concrete structure, the crack growth requires a certain amount of energy that can only be studied through an energy based propagation criterion. The fracture process in quasi-brittle material involves the material separation that is better described by fracture mechanics based energy principles than by stress or strain criterion.

(ii) The finite element formulation based on limiting stress or strain criteria showed the dependency on mesh size. However, by incorporating the fracture criteria based concrete model in finite element analysis, the observed response is found to be free from mesh sensitivity.

(iii) In a quasi brittle material that exhibits softening, the failure process does not result in the formation of plastic hinges at isolated locations, but the fracture zone propagates throughout the structure leaving behind a wake zone of reduced stress due to lack of yield plateau. Due to absence of yield plateau in concrete, the limit analysis solution grossly overestimates the failure load because it does not consider the reduced stress in its wake zone that can be accounted for by describing the concrete softening. The softening governed by the complex cracking can be utilized by introducing the concept of concrete fracture mechanics.

(iv) The structural size effect is the most important issue in the fracture mechanics of quasi-brittle material. The prediction of the structural size effect on the failure load, from the fracture mechanics approach is quite different from the strength criteria as is clear from **Fig. 1.2**, in which the x axis represents the log of characteristic dimension of the structure and y axis characterizes the nominal stress at failure load. The size effect **[Shah et. al. (1995), Bazant and Planas (1998),** and **Shailendra** and **Barai (2011)]** appears on the mechanical response of the concrete structures. The elastic analysis with allowable stress, plastic limit analysis, or any theory based on strength limit, predicts the load capacity of structure in which the material failure criterion is expressed in terms of stress/strain. The load capacity of structure predicted using these theories is independent of the structure size, which came to be known as the case of no size effect. This is what is still assumed in most of the design codes and standards for concrete. The size effect represents the deviation of actual load capacity of structure from the load capacity predicted by limiting strength based theories. It is characterized in term of nominal strength representing the value of nominal stress at ultimate load. The size effect on structural strength in terms of the nominal strength σ_{Nu} of structure, which is a parameter of maximum load P_c having the dimension of stress, is described as:

$$\sigma_{Nu} = \frac{c_n P_c}{tD} \qquad \text{Eq. (1.1)}$$

Where D = characteristic size of the specimen or structure, t = specimen thickness and c_n = dimensionless coefficient. The plot of log σ_{Nu} vs. log D always gives a horizontal line according to the strength criterion; exhibit no size effect as shown in **Fig**. **1.2**. The failure governed by Linear Elastic Fracture Mechanics (LEFM) exhibit a rather strong size effect which is described by inclined line of slope (-1/2) in **Fig**. **1.2**. The reality for concrete structures in the intermediate size range is a transitional behavior illustrated by the solid curve.

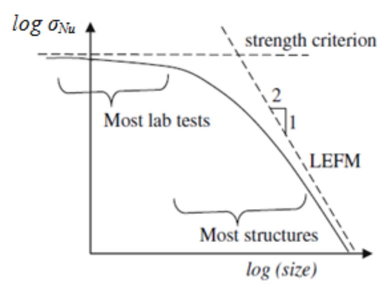

Fig. 1.2 Size effects in quasi-brittle material [**Bazant** and **Planas (1998)**]

1.2 Objectives and Research significance

Concrete shows a stable non-linear fracture response in tension loading, when tested under displacement control mode. The reason for the non-linearity is the development of a fracture process zone (FPZ) due to the micro-crack initiation, crack formation and its propagation in concrete structures. In a quasi brittle material like concrete the energy dissipated for the formation of FPZ ahead of the crack tip, is termed as fracture energy. The fracture energy and

FPZ characteristics are the most useful parameters for characterizing the fracture behavior and analysis of concrete structures. Studies on the concrete fracture energy, FPZ, the behavior of concrete during fracture process and size effect are at the forefront of research on concrete fracture. The main objective of this study is to present various approaches for the investigation of the size independent fracture energy and characteristics of FPZ that can be used as a material parameter in the numerical analysis of concrete structures.

The present study deals with the numerical simulation of the geometrically similar Three Point Bend (TPB) beams having constant length to depth ratio. The mesh sensitivity is an extremely important issue in concrete due to its post peak softening, that has been addressed in the present work by performing a number of computational studies. The fracture energy based concrete softening model yields the consistent finite element results independent of the mesh size. By incorporating the fracture energy based softening model for concrete in the analysis, the results are observed to be mesh insensitive as reported by **Singh et. al. (2009)** and **Trivedi et. al. (2013)**. The observed kinks, due to directional bias or induced anisotropy in finite element modeling using the quadrilateral elements, have been investigated. Further, based on the completeness of interpolation function and discretization technique, the superiority of triangular elements over quadrilateral elements is explained and illustrated by considering the benchmark problems of TPB concrete fracture tests.

The fracture test on geometrically similar (same length to depth ratio) TPB plain concrete beam specimens, made of aggregates, sand, cement and water, were performed by **Raghu Prasad (2009)** and **Muralidhara (2010)** as per RILEM (English acronym of original French abbreviation RILEM: The International Union of Laboratories and Experts in Construction Materials, Systems and Structures) recommendation. The displacement controlled test on the universal TPB specimens was conducted for varying notch to depth (*a/D*) ratio = 0.05, 0.25 and

0.33. The present work involves the numerical modelling of fracture tests of geometrically similar TPB beams having constant length to depth ratio for various *a/D* ratios. The simulation of TPB specimen performed by the finite element analysis incorporating the concrete softening behavior, predicts the load-load line displacement curves. RILEM fracture energy (G_f) values evaluated through the numerically predicted and experimentally observed load-load line displacement curves are beset with size effects. Therefore, the present study investigates the easy and robust techniques for the determination of the size independent fracture energy (G_F) of concrete.

G_f values are utilized to determine G_F by popular Hu and Wittmann method based on bilinear model. In addition, the fact as reported in literature that ratio of fracture energy to the un-cracked ligament length almost becomes constant at larger un-cracked ligament lengths is proved in this study. Further, the relationship based on fracture energy release rate is developed to evaluate G_F. In another approach, G_f values have been averaged out at various *a/D* for geometrically similar beams to develop a methodology for assessment of G_F of concrete.

A quantitative evaluation of fracture parameters is required to improve the understanding on phenomenon of fracture propagation and FPZ. The notched concrete beams subjected to quasi-static three-point bending are considered to measure displacement and strain fields using the Digital Image Correlation (DIC) experimental technique. Attention is paid to develop a new methodology known as Optical Crack Profile (OCP) scheme, based on DIC experiments, which can assess the characteristics of FPZ appearing above the notched concrete beams. DIC allows the analysis of continuous real time data acquisition, and thus the various fracture parameters such as crack opening displacement, width of FPZ, length of FPZ and fracture energy can be evaluated through OCP. FPZ is an already formed crack whose adjacent surfaces can still transmit stresses due to the crack bridging effect of material heterogeneities **[Luigi** and **Gianluca**

(2008)]. The softening curve as shown in **Fig. 1.3** shows the relationship between bridging stresses (σ) versus crack opening displacements (w). The area under the initial tangent of the softening curve represents the fracture energy which is governed by the failure load of test specimens. As the crack grows, the σ-w relation changes along the projected ligament. At critical load the bridging stress is close to tensile strength of concrete, f_t. Using the concept shown in **Fig. 1.3**, the σ-w relation at various stages of crack growth along the projected ligament is established through OCP technique. Thus the variation of fracture energy along the projected ligament using the concept of area under the initial tangent of the softening curve can be estimated, from which the average fracture energy can be assessed.

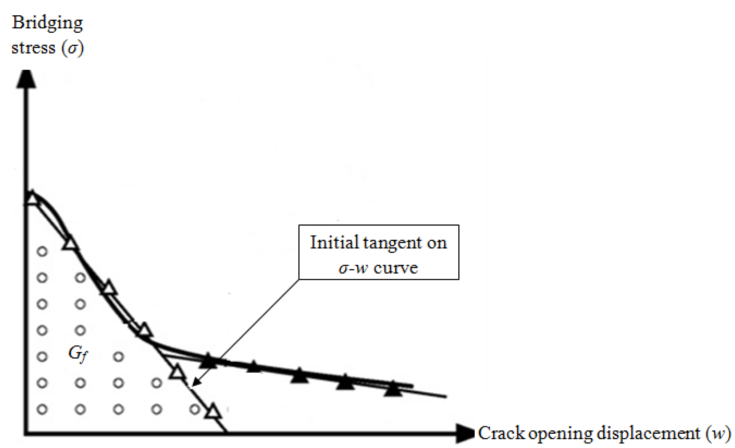

Fig.1.3 Softening curve: bridging stress (σ) vs. crack opening displacement (w) curve

Further, fracture parameters using three regression approaches based on Bazant size effect laws **[Shah et. al. (1995), Bazant and Planas (1998),** and **Shailendra** and **Barai (2011)]** and Jenq-Shah law **[Shah et. al. (1995)]** are evaluated.

1.3 Organization of thesis

This thesis deals mainly with the investigation of size independent fracture energy of concrete and characteristics of FPZ. Chapter 1 consists of three sections. The first section describes the toughening mechanism of concrete and major reasons for application of fraction mechanics in concrete structures. The next section in Chapter 1 explains the objectives and research significance. The last section contains the organization of the thesis.

The detailed literature reviews on fracture mechanics and finite element studies are presented in Chapter 2. The limitations of existing literature and scope of present work are also mentioned in Chapter 2.

The finite element simulation of the benchmark problems of **Sancho et. al. (2007), Shailendra** and **Barai (2011)** are presented in Chapter 3. The comparison of experimental responses with those of numerical predictions, based on RILEM recommendation is also described in Chapter 3.

The assessment of size independent fracture energy values with various methodologies based on Hu and Wittmann bilinear model, energy release rate and averaging of RILEM fracture energy have been addressed in Chapter 4.

Chapter 5 describes the size effect through the three regression approaches based on Bazant's size effect law and Jenq-Shah model for assessment of the fracture parameters.

Chapter 6 deals with development of scheme for quantification of characteristics of Fracture Process Zone (FPZ) using the Optical Crack Profile (OCP) technique. The evaluation of fracture propagation, FPZ characteristics, fracture energy and crack opening displacement have been addressed.

Comments on the Size Independence of Fracture Energy and Innovativeness in the Present Research are described in Chapter 7.

The summary and conclusions drawn from the study are explained in Chapter 8. Scope for further research is also presented in this chapter.

Chapter 2

LITERATURE REVIEW

The application of fracture mechanics to assess the integrity of a structure is based on the postulation of a pre-existing crack from which failure starts. Cracks lead to high stresses near the crack tip and it should receive particular attention because from here the further crack growth takes place. The original concept of fracture was initiated by Griffith through the investigation of fracture of glass sheets [**Griffith (1920)**]. **Griffith (1920)** proposed that the weakening of glass material due to presence of crack could be treated as an equilibrium problem in which the reduction in strain energy due to crack propagation could be equated to the increase in surface energy because of increase in surface area. Griffith's theory originated from the hypothesis that for glass like brittle materials containing elliptical micro-cracks introduce the high stress concentrations near crack tip. He developed a relationship between the crack length, surface energy connected with traction free crack surfaces and applied stress. Griffith theory could not account for the zone of yielding developed at the blunted fracture front in case of metals. Therefore, the first major contribution of **Irwin (1948)** was to modify the Griffith's approach to metals by including the energy dissipated in the local plastic flow. On loading, the inelastic deformation and the nonlinear effects are produced near the crack tip. However, for brittle materials, the amount of inelastic deformation is very small and localized as compared to the crack size and characteristic length of the body. In such cases, the linear theory is adequate to address the problem of stress distribution in the cracked body. Linear Elastic Fracture Mechanics (LEFM) allows the stress to approach infinity at a crack tip due to stress field singularity. Since infinite stress cannot develop in real materials, a certain range of inelastic zone must exist at the crack tip [**Perez (2004)** and **Gdoutos (2005)**]. The nonlinear region consists of two zones, namely, Fracture Process Zone (FPZ) and yielding zone. The fracture process zone is characterized by the progressive softening for which the stress decreases at increasing deformation. This zone is surrounded by yielding zone characterized by hardening plasticity or perfect plasticity, for which the stress increases at increasing deformation or at least remains constant. For metallic materials, this inelastic zone is mainly dominated by plasticity, which is often termed as yielding zone. In case of concrete, which is a heterogeneous material, the inelastic zone around a crack tip is primarily governed by softening behavior, which is termed as FPZ, and is further surrounded by a very small plasticity zone. Depending on the relative sizes of these two zones and structures, one may distinguish three types of fracture behavior. In the first type of behavior of brittle material, the whole nonlinear zone is small compared to structure size as shown in **Fig. 2.1a**. Then the entire nonlinear zone is almost confined to the crack tip in case of brittle material. The whole body is elastic and LEFM can be used. In the second and third types of behavior, the ratio of nonlinear zone size to the structure size is not sufficiently small, and LEFM is inapplicable. In the second type of behavior shown in **Fig. 2.1b** where most of the nonlinear zone consists of elastic-plastic hardening or perfect yielding and the size of the actual fracture process zone is still small. Many ductile metals fall into this category and its general type is defined as ductile. This kind of behavior is best treated by specialized branch of fracture mechanics –elastic-plastic fracture mechanics. The third type of behavior shown in **Fig. 2.1c** which is of main interest here in the context of concrete fracture includes situations in which a major part of the non linear zone undergoes progressive damage with material softening due to micro-cracking, void formation, friction and aggregate bridging. The zone of plastic hardening or perfect yielding in this type of behavior is often negligible. There is rather abrupt transition from elastic response to damage. This happens for concrete, rock, cemented sand and ceramics etc. These materials are called quasi-brittle because even if no appreciable plastic deformation takes place the size of fracture process zone is large enough to be taken into account in calculations.

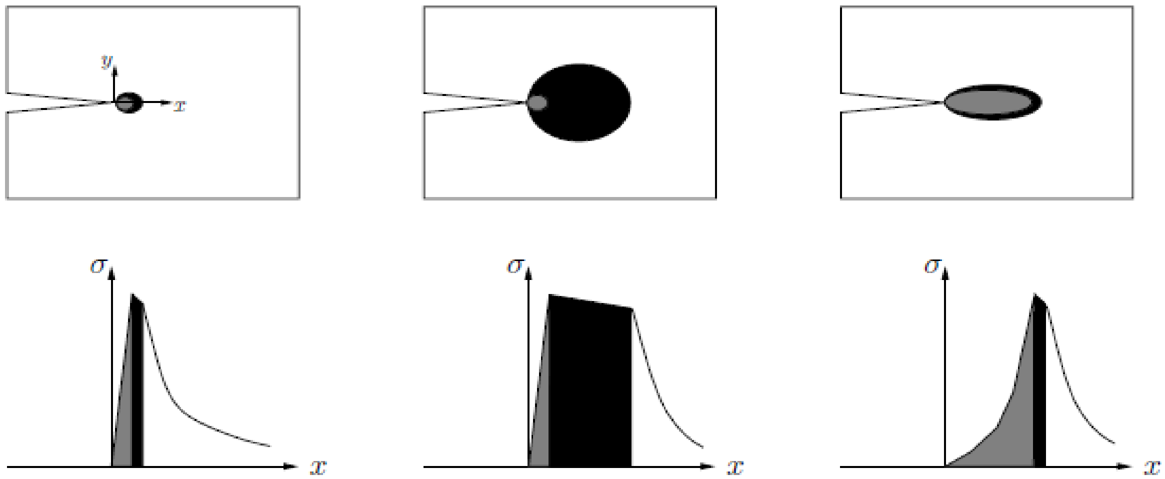

(a) (b) (c)

Fig. 2.1 Stress variation along ligament for three types of fracture behavior (a) brittle (b) ductile (c) quasi-brittle [**Bazant and Planas (1998)**]

Concrete is a quasi-brittle material that shows a post peak softening behavior, which may be characterized between a brittle, and a ductile material behavior. The micro-crack initiation, crack formation and crack propagation in concrete consumes the energy, which results in the formation of FPZ. FPZ consists of scattered micro-cracks formed in front of a pre-crack or a notch tip. The size of the FPZ in front of an existing crack or notch determines the type of failure and extent of energy dissipated during fracture as reported by **Bazant** and **Oh (1988)**, **Karihaloo (1995)**, **Koji** and **Date (2000)**. Studies on the concrete fracture energy, FPZ, the behavior of concrete during fracture process, size effect are still under extensive research as elaborated in the subsequent sections.

2.1 Existing literature on concrete fracture

The studies performed to characterize the concrete fracture behavior are described below.

A review study by **Elices** and **Planas (1996)** was carried out on the cohesive model. It was observed that the theoretical and experimental aspect of cohesive model was able to explain and predict most of the experimental results with concrete samples. The equivalent elastic crack model was also discussed in this study.

The fictitious crack method was applied to determine the response of notched plain concrete beams under three-point bending by **Sundara et. al. (1996)**. The load-deflection diagrams of concrete beams using the various forms of strain softening relations were determined. The results show that there is a need to determine a realistic softening relationship.

The concept of non-constant distribution of the fracture energy along the crack growth path and boundary effect was introduced by **Duan et. al. (2003)** to explain the size-dependence of the fracture energy. The characteristics of FPZ in the middle and close to the back boundary of a specimen are observed to be different. A first approximation assuming a bilinear fracture energy distribution was considered to account for the boundary effect on the propagation of a fictitious crack in concrete.

The size effect, two parameter, and fictitious crack models were employed to determine the fracture toughness values of concrete by **Hanson** and **Ingraffea (2003)**. The results indicated that the fracture toughness values for the size effect and two parameter models tend to be less than those predicted by the fictitious crack model.

The experimental investigation to study the size effect was performed by **Karihaloo et. al. (2003)** on three point bend specimens. The hardened cement paste with nominal compressive strength of 40 MPa and high strength concrete of nominal compressive strength 110 MPa were used to cast the beams. Failure loads were analyzed according to the size effect laws for the un-notched and notched beams.

The study by **Karihaloo et. al. (2003)** stated that size independent fracture energy of concrete could be obtained by testing three point bend or wedge splitting specimens. Twenty-six test data sets existing in literature were re-evaluated on fracture energy of concrete to assess the validity of this observation. The re-evaluation is found to support this observation.

The two fracture properties of concrete i.e. true fracture energy and corresponding softening relation are required for the analysis of cracked concrete structures. A simple method for determination of true fracture energy and corresponding softening relation was proposed by **Abdalla and Karihaloo (2004)** through the fracture tests conducted on three point bend and wedge split concrete specimens.

The study by **Karihaloo et**. **al**. **(2006)** mainly focuses on identifying and quantifying the deterministic size effect in the cracked concrete structures. The strength of geometrically similar pre-cracked specimens of varying sizes prepared from three concrete mixes were measured in three point bend and wedge splitting geometries to study the size effect. Also, the size-independent fracture energy and the corresponding tension softening diagram of each of the three mixes are independently established in order to exclude their influence on the strength size effect.

The experimental study using a non-destructive method called Digital Image Correlation (DIC) technique was performed by **Kozicki and Tejchman (2007)** on notched concrete specimens under three point bending. Three different beam sizes and two different concrete mixes were used. The strong size effect and the evolution of fracture process zone were observed.

The study by **Luigi** and **Gianluca (2008)** deals with the identification of concrete fracture parameter through the size effect experiments. The tensile strength and initial fracture energy was determined from size effect curve i.e. structural strength vs. structural size methods utilize the size effect curve. The peak and the initial post peak slope of the cohesive crack law is characterized by tensile strength and initial fracture energy.

The fracture test on geometrically similar (constant length to depth ratio) three point bend (TPB) plain concrete beam specimens, made of aggregates, sand, cement and water, were performed by **Raghu Prasad (2009)** and **Muralidhara (2010)**.

The study by **Skarzynski** and **Tejchman (2010)** describes the investigations on fracture process zones at meso scale in notched concrete beams subjected to quasi static three point bending using the finite element analysis (FEA) and DIC method. The isotropic damage constitutive model was incorporated in FEA. The evolution of strain localization was captured using the numerical simulation results and were observed to be in reasonable agreement to the DIC method.

Acoustic emission technique on three point bend specimen was used to capture the FPZ as reported in study by **Muralidhara (2010)** and **Muralidhara et. al. (2010)**. Considering the variation of relative size of FPZ with the characteristic dimension of three point bend beam, an expression is derived by **Muralidhara et. al. (2013)** to compute the size-independent fracture energy of concrete.

The study by **Karihaloo et. al. (2013)** proposed a tri-linear model for the determination of the fracture energy for three different concrete mixes ranging in compressive strength from 57 MPa to 122 MPa.

In this study of **Cifuentes et. al. (2013)**, an experimental comparative analysis of the size-independent fracture energy has been carried out by two methods based on the local fracture energy model and the curtailment of the tail of load-deflection curve.

An experimental investigation on notched and un-notched beams cast from one batch of concrete was performed to obtain nearly complete post peak softening load–displacement curves by **Hoover et. al. (2013)**. The size effect studies were performed and the fracture energy was evaluated.

The mode I crack propagation was investigated by **Fayyad** and **Lees (2014)** using DIC. The tests were performed on small scale reinforced concrete specimens in three point bending. By means of the DIC technique the visualization and quantification of the crack opening displacements in reinforced concrete.

In this paper, fracture process in geometrically scaled concrete beams under bending test is analyzed through two techniques in coupled position i.e. Acoustic emission (AE) and DIC by **Alam et**. **al**. **(2014)**. The AE technique is useful to identify the location of fracture growth due to microcracks and macrocrack, however, DIC is useful to measure the fracture length.

Gencturk et. **al**. **(2014)** explained the advantages and limitations of the DIC through the full scale testing of pre-stressed I-shaped concrete beam. Two ultimate load tests were conducted and the measurements collected from both conventional instruments (displacement transducers) and a pair of high definition cameras was compared. It was observed that the DIC technique could provide very accurate and detailed information, which is not possible to obtain using conventional techniques. The limitations of the DIC technique when used in testing of concrete structures such as the sensitivity to external light sources, preparation of the measurement surface and loss of data points after spalling of cover concrete were also mentioned.

2.2 Superiority of triangular elements over the quadrilateral elements in finite element analyses of concrete fracture problems

Finite Element (FE) is a numerical technique to find the approximate solutions of the differential equations that describe the physical phenomenon encountered in engineering mechanics. FE method calculates nodal displacements, and then uses the displacement information to calculate the strains and finally the resulting stresses with a constitutive law. **Fig. 2.2** shows a finite element mesh of a continuum using triangular and quadrilateral elements.

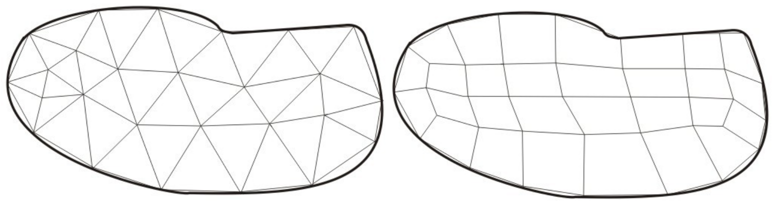

(a) (b)

Fig.2.2 FE discretization (a) Triangular mesh (b) Quadrilateral mesh [**Cook et. al. (2007)**]

A constant strain triangle (CST) is a plane triangle whose field quantity varies linearly with Cartesian co-ordinate x and y. The stress analysis of a linear displacement field produces a constant strain field, so the element is known as constant strain triangle. In CST element, strain inside the element has no variation and hence element size should be small enough to obtain accurate results. The CST element shown in **Fig. 2.3** is perhaps the earliest and simplest finite element. In terms of generalized coordinates β_i its displacement field is expressed as:

$$u = \beta_1 + \beta_2 x + \beta_3 y \qquad \text{Eq. (2.1)}$$

$$v = \beta_4 + \beta_5 x + \beta_6 y \qquad \text{Eq. (2.2)}$$

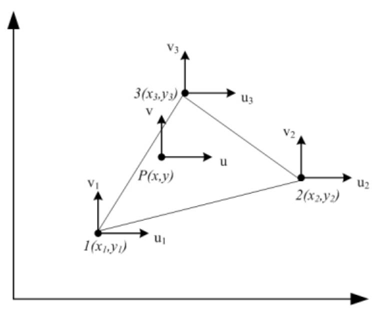

Fig. 2.3 Constant strain triangular element [**Cook et. al. (2007)**]

And from the two-dimensional strain-displacement relation, the resulting strain field is:

$$\varepsilon_x = \frac{\partial u}{\partial x} = \beta_2 \qquad \text{Eq. (2.3)}$$

$$\varepsilon_y = \frac{\partial v}{\partial y} = \beta_6 \qquad \text{Eq. (2.4)}$$

$$\gamma_{xy} = \frac{\partial u}{\partial y} + \frac{\partial v}{\partial x} = \beta_3 + \beta_5 \qquad \text{Eq. (2.5)}$$

Here, as clear from **Eqs**. **2.3-2.5**, the strain does not vary within the element hence named as "constant strain triangle". A quadratic rectangle (Q8) shown in **Fig. 2.4** is obtained by adding the side nodes to the linear rectangle. The Q8 notation is used for the eight node quadrilateral element. In terms of generalized coordinates a_i the displacement field is expressed as:

$$u = a_1 + a_2 x + a_3 y + a_4 x^2 + a_5 xy + a_6 y^2 + a_7 x^2 y + a_8 xy^2 \qquad \text{Eq. (2.6)}$$

$$v = a_9 + a_{10} x + a_{11} y + a_{12} x^2 + a_{13} xy + a_{14} y^2 + a_{15} x^2 y + a_{16} xy^2 \qquad \text{Eq. (2.7)}$$

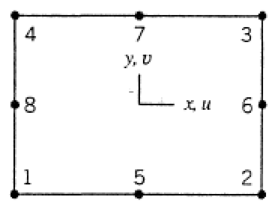

Fig. 2.4 Quadratic element [**Cook et. al. (2007)**]

For a three noded triangular element, the linear displacement field is chosen as is clear from **Eqs. 2.1-2.2**. The linear field is able to display the rigid body motion, constant strain state and mesh refinement produces the convergence towards the correct results. Thus, the lowest order term must not be omitted. For a three noded triangular element, the necessary constant strain and rigid body motion capabilities can't be provided by the higher order terms of the polynomial ~ $\left(a_1 x^2 + a_2 xy + a_3 y^2\right)$.

Another important attribute of satisfactory polynomial displacement fields is balance, that is, the displacement function should not represent direction bias with chosen frame of reference (x-y coordinates for a two dimensional problem). In addition, the element formulation should ensure geometric isotropy or frame invariance, so that the behavior of an FE structure is independent of the orientation of the local coordinates of its element are oriented with respect to a global coordinate system. FE model that does not have a balanced field is sensitive to coordinate system orientation, and as a result, it displays the artificial directional bias or induced anisotropy. An element, whose displacement expression is a complete polynomial, has automatically a balanced field. The CST element uses a linear polynomial as per **Fig. 2.5**. A salient feature of CST element is that their interpolations are based on complete polynomial expansions as is clear from **Eqs**. **2.1-2.2**. A Q8 element has an incomplete cubic terms expansion as is clear from **Eqs**. **2.6-2.7** (x^3 and y^3 missing as per **Fig. 2.5**). Since the completeness of polynomials avoids kinks formation and intrinsic directional bias, the performance of triangular elements with respect to smeared crack propagation have been found to be superior over the quadrilateral elements which is illustrated in the next chapter.

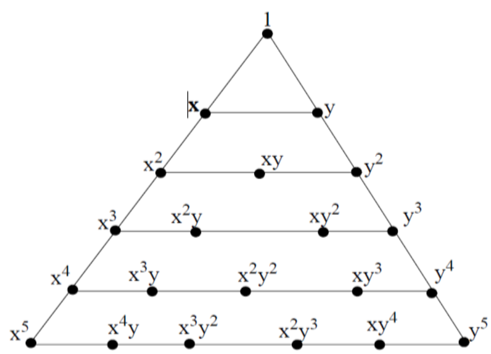

Fig. 2.5 Pascal triangle: complete polynomial in two independent variables *x* and *y* [**Zienkiewicz (2006)**]

2.3 Limitations in existing literature

It can be concluded from the extensive literature review that the investigation undertaken so far involved limited concrete fracture tests on laboratory size concrete specimens. Based on the existing literatures on proposed analytical models and fracture tests on concrete specimens, the basic understanding developed so far is still contradictory due to the complex fracture behavior of concrete. The exact quantification of size independent fracture energy remains elusive. FPZ is very complex since it consists of main cracks with various branches, secondary cracks and micro-cracks. Therefore, qualitative description of the FPZ based on Digital Image Correlation (DIC) experimental technique, which is available in literature does not provide any detailed information on characteristics of FPZ. The structural size effect is the most important issue in the fracture mechanics of quasi-brittle material, which has been addressed in the existing literature. But so far the link between the fracture parameters based on size effect studies with the other approaches of Hu and Wittmann model, fracture energy release rate, G_f averaging for geometrically similar beams and Optical Crack Profile (OCP) technique (which is based on DIC experiments) have not been addressed.

2.4 Scope of the present work

The limitations mentioned above have been addressed in the present work as follows:

- The numerical simulation of displacement controlled fracture tests of the geometrically similar TPB beams having constant length to depth ratio is performed. The issue of mesh sensitivity and the superiority of triangular finite elements over quadrilateral finite element have been addressed.
- RILEM fracture energy (G_f) values evaluated through load-load line displacement curves are beset with the size effect. Hence, the size-independent fracture energy (G_F) of concrete is estimated through Hu and Wittmann method based on bilinear model. G_F is also estimated from developed relationship on fracture energy release rate. G_f values associated with geometrically similar beams have been utilized to develop another methodology for assessment of G_F.
- A quantitative study on characteristics of FPZ, fracture energy and crack opening displacement is performed using OCP technique. Further, the characteristics of FPZ identified by OCP is compared with conventional technique of strain gauge and ACI guideline.

- The size effect studies are performed and fracture parameters are evaluated. A comparative analysis of fracture parameters based on Hu and Wittmann model, fracture energy release rate, G_f averaging for geometrically similar beams, Bazant size effect laws, Jenq-Shah model and OCP technique have been carried out.

Chapter 3

FRACTURE TEST AND NUMERICAL SIMULATION

3.1 General Introduction

Three-point bend (TPB) test, compact tension test, and wedge splitting test specimens are the commonly used shapes of geometry for conducting fracture tests [**Shah et. al. (1995), Bazant and Planas (1998),** and **Shailendra** and **Barai (2011)]**. The most common specimen is three-point bending geometry, as recommended by RILEM, for determination of the fracture parameters as is shown in **Fig. 3.1**. 'P', 'D', 'S' and 'a' are applied load, beam depth, beam span, and notch depth respectively. TPB geometry has great advantage over compact tension and wedge splitting test since its testing can be performed with the standard testing machines. TPB testing involves the bending test on notched beams. However, the large-size structures require the special care during fracture experiments due to handling problems of test specimens.

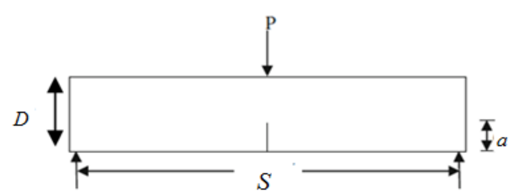

Fig.3.1 TPB geometry

3.2 RILEM test for concrete fracture energy

RILEM technical committee recommended the guidelines for determination of fracture energy of cementitious materials by conducting TPB test on notched beam as shown in **Fig.3.1**. In order to obtain a complete load and load point displacement curve, a closed loop servo controlled testing machine is recommended. Based on the obtained load and load point displacement curve, the fracture energy G_f can be calculated. The influence of the self weight is represented by an additional equivalent force P_w. Therefore, the total load P on the beam is represented by $P = P_w + P_a$, where P_a is the load applied by the testing machine, provided that load and displacement are both along the direction of gravity. The energy absorbed by the beam is represented by the area under P-δ curve, as shown in **Fig 3.2.** where δ is the load point displacement. The total area under the P- δ curve is referred to as W_t, which may be divided into three parts, W_0, W_1, and W_2, as shown in **Fig. 3.2**. Here W_0 is the area under the P_a- δ curve and $W_1 = P_w \delta_0$ where δ_0 corresponds to displacement at $P_a = 0$. Thus, both values of W_0 and W_1 can be determined from the measured P_a- δ curve. It has been demonstrated [**Shailendra** and **Barai (2011)**] that the value of W_2 is approximately equal to the value of W_1. Therefore, the total fracture energy of the beam, W_t is

$$W_t = W_0 + 2P_w \delta_0$$

By assuming that energy absorption takes place only in the fracture zone, the fracture energy per unit projected area is given as[1-2]:

$$G_f = \frac{W_t}{(D-a)t} = \frac{W_0 + 2P_w\delta_0}{(D-a)t}$$

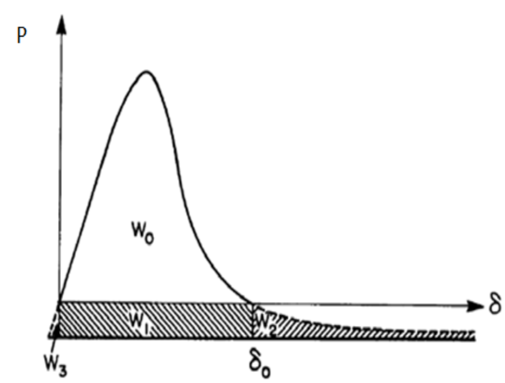

Fig.3.2 Load-displacement curve **[Shailendra** and **Barai (2011)]**

3.3 Material property, specimen preparation and experimental setup

The fracture test on geometrically similar (same length to depth ratio) TPB plain concrete beam specimens, made of aggregates, sand, cement and water, were performed by **Raghu Prasad (2009)** and **Muralidhara (2010)**. The mix proportion of M45 concrete grade prepared at BARC, Tarapur site is given in **Table 3.1**. The cement used was 43 grades Portland cement conforming to Indian Standard IS: 8112-1689. The dimensions of geometrically similar beams designated as D1, D2 and D3 are as shown **Table 3.2**. The geometrical sketch for one of the beam D3 is shown in **Fig**. **3.3**. The casting of D1 and D2 beam was carried out at Tarapur site where as the large size D3 beams casting was done at IISc, Banglore. Two different concrete mixes were prepared for both D1 and D2 using the maximum aggregate size of 12.5 mm and 20 mm. Further, three identical beams for each a/D value (**Table 3.2**) were cast for each D1 and D2 specimen. For D3, three identical specimens were prepared for each *a/D*, namely, 0.25 and 0.33 using the concrete mix prepared with maximum aggregate size of 20 mm only. The technical details of specimens are shown in **Table 3.3** along with the nomenclature of the beams tested. The maximum size of the aggregates (mm) is used in the specimen nomenclature indicated by numbers 12.5 and 20 mentioned in **Table 3.3**. The nomenclature employed for various types of beam is as follows: for example, in D1P12.5A, the first two letters (e.g. D1 here) represent the beam name (i.e. D1 or D2 etc.), P and T indicate pour mix and trial mix respectively, the number 12.5 indicate the maximum size of the aggregate (mm), beams with *a/D* = 0.05, 0.25 and 0.33 are designated by A, B and C respectively.

Table 3.1: Quantity of materials per cubic meter of concrete **[Raghu Prasad (2009)]**

Property	Mix-with 20 mm and down size coarse aggregates	Mix-with 12.5 mm and down size coarse aggregates
Cement (kg) (c)	400	435
Coarse aggregate (kg) (CA) 20 mm	492	-
Coarse aggregate (kg) (CA) 12.5 mm	492	946
Fine aggregate (kg) (FA)	902	870
Water (kg)	152	165
Superplasticizer (% weight of cement content)	1.4	1.4
Water/cement ratio	0.38	0.38
Mix proportion (c:FA:CA)	1:2.26:2.46	1:2:2.18

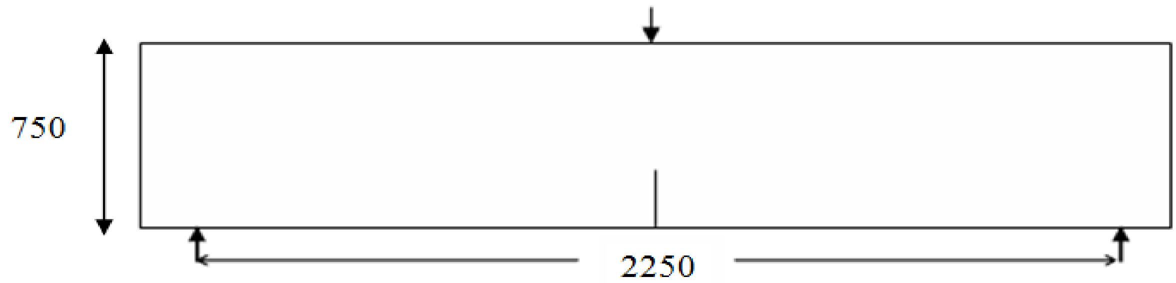

Fig.3.3 Dimensions of D3 beam in mm for a/D = 0.33

Table 3.2: Geometrical dimensions of beam

Type	Length (mm)	Depth (mm)	Width (mm)	Span (mm)	a/D
D1	375	94	47.5	282	0.05,0.25,0.33
D2	750	188	95	564	0.05,0.25,0.33
D3	3000	750	375	2250	0.25,0.33

Table 3.3: Technical details of beam types **[Raghu Prasad (2009)]**

Sl.No	ID. No.	No. of specimens	Compressive Strength MPa		E value (MPa)
			7 days	28 days	
1	D1T20	9	36.0	50.4	24638
2	D1T12.5	9	38.3	50.3	24248
3	D1P20	9	40.3	50.6	25689
6	D2T20	9	36.0	50.4	24638
7	D212.5	9	38.3	50.3	24248
8	D2P20	9	40.3	50.6	25689

D1 is the smallest size specimen among all beam types whose notches were made using 2mm thick tile cutting circular blade. The 5mm thick circular blade was used to cut the notches in D2 beams. The notches for the D3 specimens were made with the help of motorized mobile cutter, fitted with diamond edged steel disc of 750mm diameter. Each beam tested under crack mouth opening displacement control mode were fixed with 5 mm thick 50mm x 60mm mild steel plates on either side of notch using metal paste to support clip gauge. To measure the central deflection, Linear Variable Differential Transducer (LVDT) was used. D1 and D2 beams were tested in servo controlled Dartec machine of 500kN capacity under three point bend condition. The servo controlled MTS machine of 1200 kN capacity was employed for D3 beam testing and each beam was carefully placed on the roller supports. After the preparation of the test setup, load, crack opening displacement and time data were acquired at certain interval of time. The acquisition of load and displacement parameters was simultaneous. The complete load vs. load point displacement and load vs. Crack opening displacement (COD) response were obtained through a closed loop servo controlled testing machine. D3 specimen being largest among all, only limited numbers of specimens were tested due to its heavy weight and handling issues. Hence, the focus of present study has been put mainly on D1 and D2 beams having plenty data sets to characterize the parameters required for concrete fracture mechanics.

3.4 Concrete fracture model

The nonlinear fracture mechanics models for quasi-brittle materials are classified as fictitious crack approach and an equivalent elastic crack approach based on different energy dissipation mechanisms. Fracture mechanics models using Dugdale- Barenblatt energy dissipation mechanism are usually referred as the fictitious crack approach, whereas fracture mechanics models using Griffith-Irwin energy dissipation mechanism are usually referred as the effective elastic crack approach [**Hillerborg et. al. (1976) and Shah et. al. (1995)**]. Fictitious Crack Model (FCM) and Crack Band Model (CBM) belong to fictitious crack approach. The two-parameter fracture model, size-effect model and effective crack model belong to effective elastic crack approach. FCM for fracture of concrete characterizes the material behavior in the fracture process zone through strain-softening constitutive relation only. CBM model characterizes the material behavior in the fracture process zone not only through strain-softening constitutive relation, but also imposes a fixed width (h) of the front of the strain-softening zone (crack band). The constant width of crack band avoids spurious mesh sensitivity, assuring that the energy dissipation due to fracture per unit length is constant, equal to the fracture energy of the material (G_f). Once the shape of the strain-softening is fixed, the CBM is fully characterized by three material parameters: G_f, material tensile strength (f_t) and h (although the influence of h is weak for situations with isolated cracks). FCM has only two basic parameters: G_f and f_t. The extra parameter in CBM is important only in situations when there are parallel cracks. FCM because of its lack of the extra parameter *h*, gives results that are mesh sensitive in situations with parallel closely spaced cracks. CBM and FCM give essentially the same results, except when closely spaced parallel cracks occur [**Bazant and Planas (1998), and ACI (1999)]**. However, in practical consideration, the structures consist of multidirectional cracking in which CBM and microplane model are preferred. The material behavior in the microplane model is characterized independently on planes of various orientations [**Bazant and Ozbolt (1989)]** and it further overcomes the limitations of conventional fracture models for complex problems with a large number of multiple cracks with different orientations.

RILEM approach was originated from the Fictitious Crack Model (FCM). Therefore, nonlinear fracture model based on the fictitious crack approach is used in present finite element simulation to determine the response of the notched plain concrete beams. The cracking and compressive behaviour of concrete are incorporated by the uni-axial test response. The post-failure behaviour associated with the strain-softening behaviour is incorporated by applying a fracture energy cracking criterion in the analysis **[Bangash** and **Telford (2001)]**. FCM based on linear strain softening stress-crack opening displacement (σ-w) relationship is used in the present numerical simulation. In the fictitious crack model, the tensile strength, fracture energy and stress-crack opening displacement relationship are incorporated to study the fracture behaviour of plain concrete. σ-w relation is one of the fundamental properties required to introduce the non-linearity in FCM. The fracture behavior of concrete is greatly influenced by the Fracture Process Zone (FPZ) characterized by the toughening mechanism. The toughening mechanisms in the FPZ are modeled by the cohesive pressure acting on the crack surfaces. The constitutive law that relates the cohesive stress (σ) across the crack faces and the corresponding crack opening displacement

w, i.e., $\sigma = f(w)$ is also known as softening function. The cohesive pressure $\sigma(w)$ is a monotonically decreasing function of crack opening displacement (w) and it tends to close the crack. The value of $\sigma(w)$ is equal to material tensile strength f_t for $w = 0$ at the crack tip. A typical sketch of σ–w curve is shown in **Fig. 3.4a** where the terminal point w_c is the maximum widening of the crack opening displacement. FCM assumes that energy (fracture energy ~G_f) produced by the applied load is completely balanced by the cohesive pressure as:

$$G_f = \int_0^w \sigma(w)dw$$

The cohesive crack model requires a unique $\sigma(w)$ curve to quantify the value of energy dissipation. The linear softening law by **Hillerborg et. al. (1976)** as shown in **Fig. 3.4b** is used in the present analyses considering f_t and G_f as the material properties. In **Fig. 3.4b**, f_t is the mean tensile strength and w_c is the maximum crack opening before the crack ceases to transfer stresses. The linear softening curve utilized in the present study is:

$$\sigma = f_t\left(1 - \frac{w}{w_c}\right), \text{ for } 0 \le w \le w_c$$

$$\sigma = 0, \text{ for } w \ge w_c \text{ and } w_c = \frac{2G_f}{f_t}$$

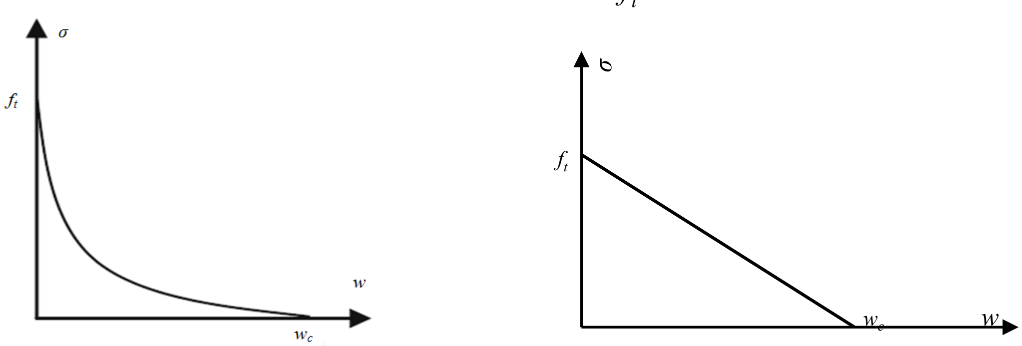

(a) (b)

Fig. 3.4 (a) Typical sketch of concrete softening (b) Linear σ-w relationship

3.5 Numerical investigation

In the present study, the parameters required to characterize the fracture behavior of concrete are evaluated by Finite Element Analysis (FEA) and compared with the reported literatures of **Sancho et. al. (2007)**, **Muralidhara (2010)**, and **Shailendra** and **Barai (2011)**. FEA of TPB concrete beam is performed by incorporating the fracture energy based softening model that yields the mesh insensitive result. The typical sketch of TPB beam is shown in **Fig. 3.5**, where "a", "D", "S", "P" and "a/D" are notch depth, beam depth, beam span, applied load and notch to depth ratio respectively.

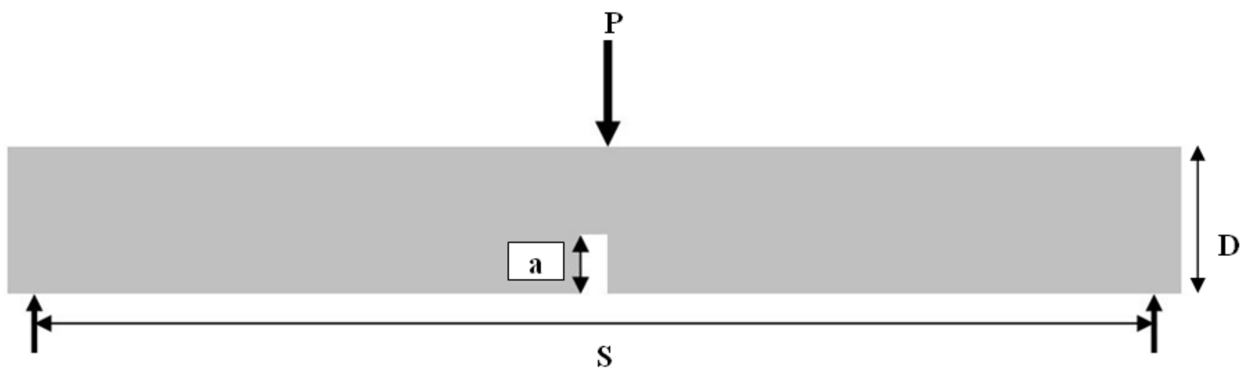

Fig. 3.5 Typical sketch of three point bend (TPB) beam specimen

3.5.1 Kinks in TPB specimens

The superiority of triangular elements as discussed in the previous chapter is demonstrated here for TPB specimens. The two dimensional modeling of concrete could be simulated using the four-node quadrilaterals, three-node constant strain triangles, six-node linear strain triangles and the eight-node quadrilateral elements. However, for the similar computational costs, the lower order elements produce the most narrow failure band. The constant strain triangles elements based on single point integration scheme are adequate in this respect because they permit the fracture to jump to adjacent rows of elements without spreading the corresponding deformation to a substantial neighboring element. The interpolating functions of triangular elements contain complete polynomial expressions, and hence automatically have a balanced field. However, the shape functions of a quadrilateral elements possess an incomplete polynomial terms. The complete polynomial expansion of interpolation function for triangular elements avoids the kinks formation and intrinsic directional bias **[Cook et. al. (2007)]**.

The two dimensional finite element method with Constant Strain Triangle (CST) elements is adopted for analyses of the concrete beams. FEA of the TPB, D2 type notch beam (**Table 3.2**) having size of 188 mm (depth) x 94 mm (thickness) x 752 mm (length) with span of 564 mm is carried out. The material property of concrete as is shown in **Table 3.4** is incorporated. Numerous numerical simulations of the four node bilinear and eight node bi-quadratic schemes with varying *a/D* have been performed and in each formulation, the result shows the kinks. **Figs. 3.6a-b** respectively represent the two results of: (i) 391 number of elements and (ii) 2945 number of elements. It is clear that these results are due to kinks resulting from intrinsic directional bias in particular it becomes prevalent when smeared cracks propagate. D2 type beam having the same material property as that of **Table 3.4** is analyzed numerically using the CST element with *a/D* = 0.25 for the various mesh size as shown in **Fig. 3.7**. Nowhere the kinks are observed in deformed meshes shown in **Fig. 3.7**. As a result, the performance of triangular elements has been found to be superior over the quadrilateral elements.

Table 3.4: Material parameters for numerical simulation

Material Parameters	Value
f_{ck} (MPa)	45
E(N/m^2)	2.5e10
Poisson ratio (ν)	0.2
f_t (MPa)	3.5
Fracture energy(N/m)	100

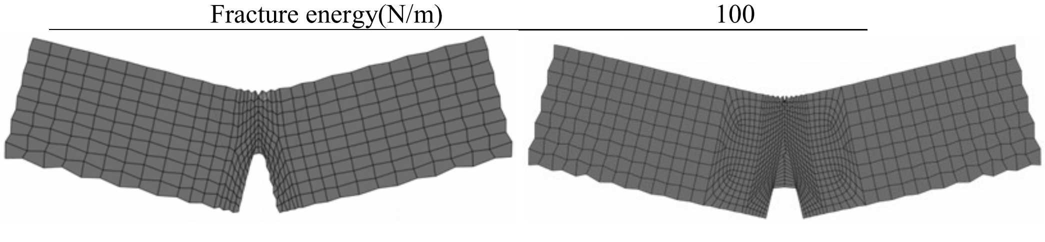

(a) (b)

Fig. 3.6 Deformed D2 beam for (a) four node bilinear scheme with *a/D* = 0.33 and (b) eight node bi-quadratic scheme with *a/D* = 0.25

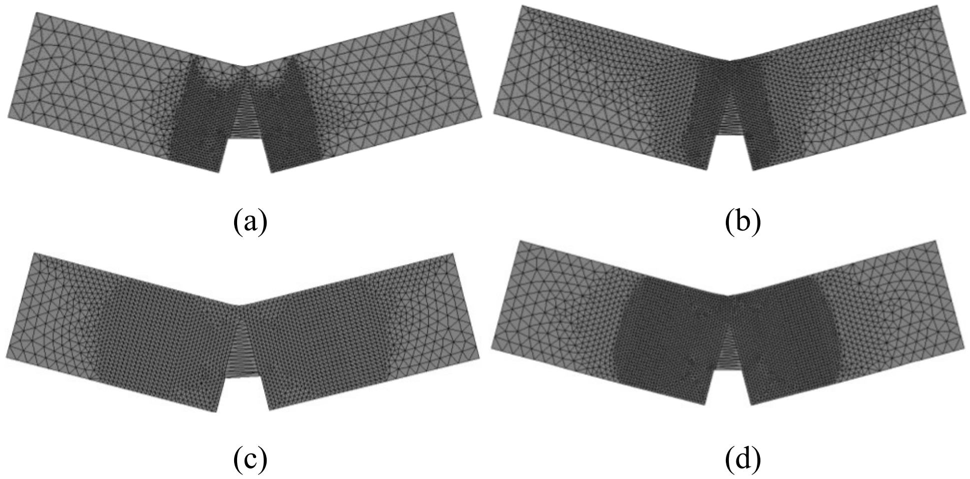

Fig. 3.7 Deformed shapes obtained through CST elements using coarse to fine meshes for D2 type beam with *a/D* = 0.25: (a) 3152 (b) 4563 (c) 6203 and (d) 7538 elements

3.6 Numerical examples

To demonstrate the effectiveness of the present formulation based on triangular element, the numerical analyses of the three benchmark problems are performed. In the first example, the numerical analysis has been carried out to predict the deflected profile of one set of TPB specimens free from the kinks, further the mesh sensitivity studies and the comparison of numerical result with that of reported literature **[Sancho et. al. (2007)]** is presented. In the second case, the numerical results predicted are compared with the literature results **[Shailendra** and **Barai (2011)]** for another set of TPB specimens. The third problem consists of the detailed numerical simulation of beams D1, D2, D3 (**Table 3.2)** including the mesh sensitivity study and the comparison of predicted result with the experimental response.

3.6.1 Case 1: TPB beam specimen analysis [Sancho et. al. (2007)]

The numerical simulation of TPB specimen is performed by incorporating the concrete material properties as mentioned in **Table 3.5**. The span (S), depth (W), width, and notch depth ratio (*a/D*) are 2000 mm, 500 mm, 100 mm and 0.4 respectively. **Fig**. **3.8a-c** illustrates the FE model with 1196 to 6206 number of elements where all the deflected FEA models are free from kinks. **Fig. 3.8d** shows the mesh sensitivity study, in which the predicted load-load line displacement response for different number of elements is found to be mesh insensitive. **Fig. 3.9** compares the load-load line displacement response predicted by FEA using 3152 number of elements with the reported result by **Sancho et. al. (2007)**. The numerically predicted response is in reasonably good agreement with the reported literature.

Table 3.5: Material properties of TPB concrete beam

Uni-axial compressive strength of concrete (MPa)	23
Uni-axial tensile strength of concrete (MPa)	2.5
Young's modulus of concrete (MPa)	20000
Poison ratio	0.17
Uni-axial ultimate compressive strain in concrete	0.0035
Fracture energy (N/m)	100

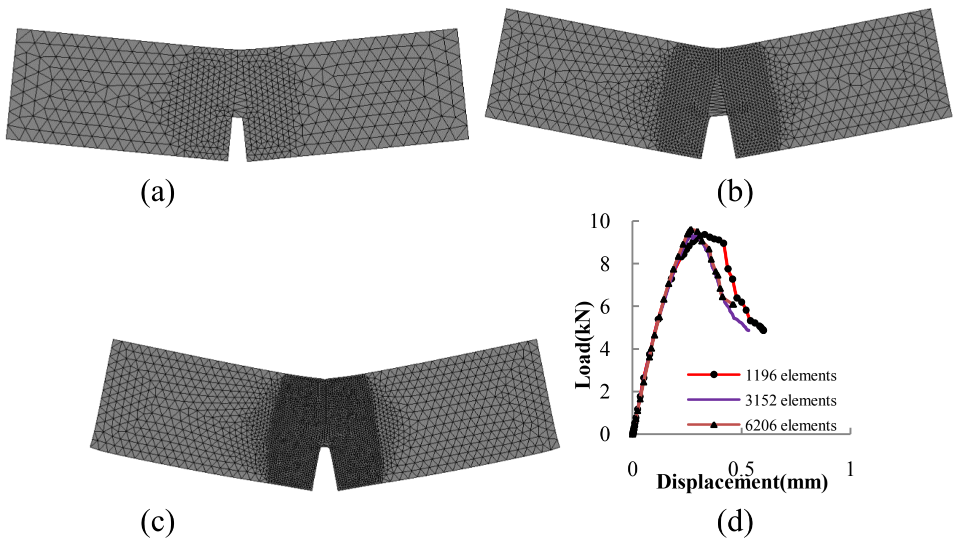

Fig.3.8 FEA mesh sensitivity study: mesh with (a) 1196 (b) 3506 (c) 6206 number of elements (d) Comparison of load-load line displacement response for various mesh size

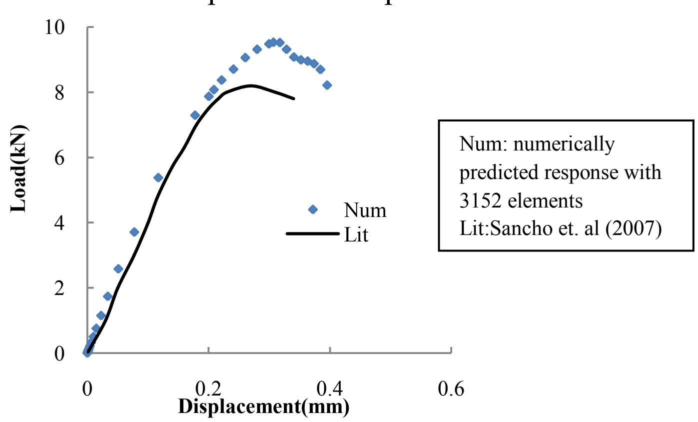

Fig. 3.9 Comparison of numerical prediction of load-displacement with the study of **Sancho et. al. (2007)**

3.6.2 Case 2: TPB beam specimen analysis [Shailendra and Barai (2011)]

Finite element simulation of the TPB beam specimen is performed by incorporating the material properties as given in **Table 3.6**. The span (S), depth (W), width and notch depth ratio (*a/D*) are 1000 mm, 250 mm, 83 mm and 1/3 respectively. **Fig. 3.10** compares the numerically predicted load-COD response with the reported literature [**Shailendra** and **Barai (2011)**]. A reasonably good agreement may be observed.

Table 3.6: Material properties of TPB concrete beam

Uni-axial compressive strength of concrete (MPa)	45
Uni-axial tensile strength of concrete (MPa)	4.5
Young's modulus of concrete (MPa)	32000
Poison ratio	0.2
Uni-axial ultimate compressive strain in concrete	0.0035
Fracture energy (N/m)	167

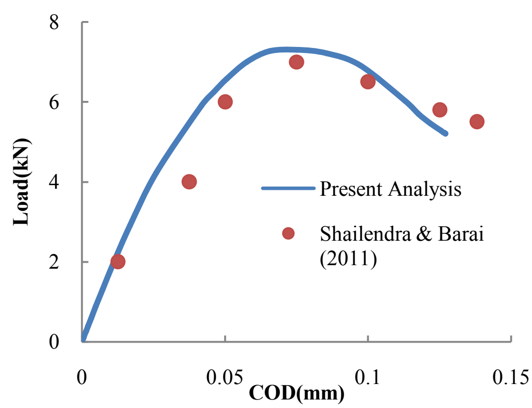

Fig.3.10 Numerical response comparison with the reported study

3.6.3 Case 3: Finite Element modeling of various types of beam for a range of *a/D*

The detailed finite element modeling of the geometrically similar TPB specimens D1, D2 and D3 (**Table 3.2**) with the varying *a/D* have been carried out. The parameters such as load-load line displacement responses, load-COD responses, maximum loads, and displacements at maximum load are predicted in the numerical simulations. The numerically predicted responses are compared with the experimental results [**Raghu Prasad (2009)**]. Brief descriptions follow:

3.6.3.1 Mesh Sensitivity

The previous section shows the performance of triangular elements to be better than the quadrilateral elements for inelastic analysis of fracture test on heterogeneous quasi-brittle materials like concrete. Hence, in this section mesh sensitivity study is limited to the CST elements. The concrete numerical modelling incorporating the strain based softening model yields the mesh sensitive results. Mesh insensitive solutions could be easily achieved by incorporating the fracture energy based softening model of concrete as proved in literature by **Singh et. al. (2009)** and **Trivedi et. al. (2013)**. To study the mesh sensitivity, the numerical modelling of TPB beam (D1 type, **Table 3.2**) having size of 94 mm (depth) x 47.5 mm (thickness) x 375 mm (length) with span of 282 mm for a/D = 0.25 is performed by incorporating the fracture energy based softening model. The material property of plain concrete beam samples as shown in **Table 3.4** is incorporated. In **Fig. 3.11** the response of coarse mesh (nominal element size ~20 mm), intermediate mesh (nominal element size ~15 mm) and fine mesh (nominal element size ~8 mm) is found to be almost mesh insensitive within the reasonable numerical error band. Similar to D1 type beam, the numerical simulation using the nonlinear FEA is performed to establish the mesh sensitivity for D2 and D3 type beams by incorporating the unique concrete material behavior through fracture based softening model. **Figs. 3.12–3.13** present the detailed mesh insensitive results through the load-load point displacement of D2 beams for a/D = 0.05 and 0.33. In **Figs. 3.11–3.13**, the numerically predicted responses for different mesh sizes such as 8 mm, 12 mm and 20 mm are shown. Excellent mesh insensitive results are observed in almost all the cases.

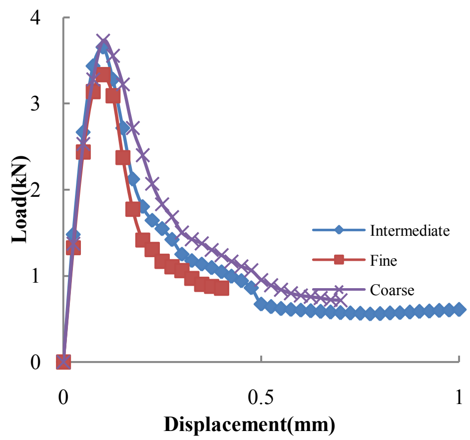

Fig. 3.11 Mesh sensitivity for D1 beam with *a/D* =0.25 through Load-displacement comparison

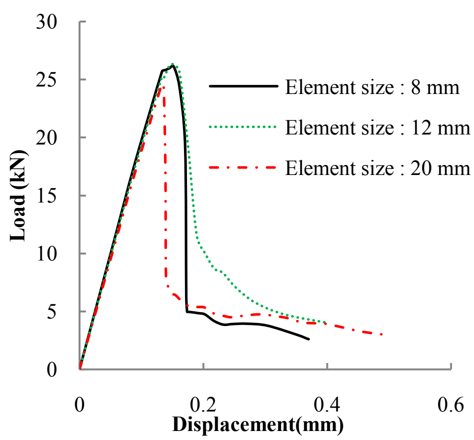

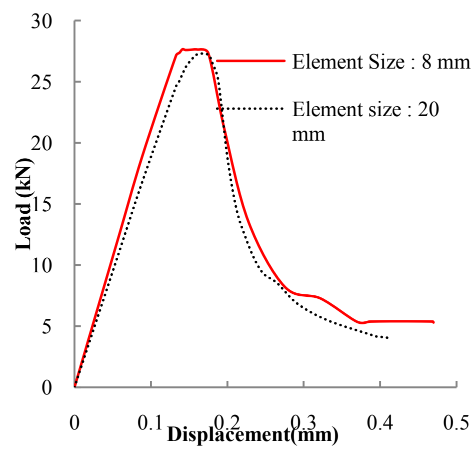

(a) (b)

Fig. 3.12 D2 beam load-displacement numerical response for *a/D* = 0.05, with aggregate size of (a) 12.5 mm (b) 20 mm

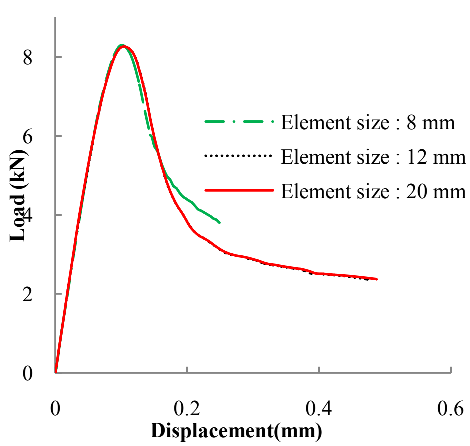

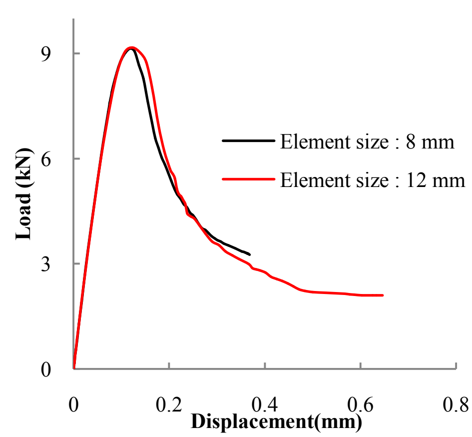

(a) (b)

Fig. 3.13 D2 beam load-displacement numerical response for *a/D* = 0.33, with aggregate size of (a) 12.5 mm (b) 20 mm

3.6.3.2 Maximum load and corresponding displacement

In **Tables 3.7-3.9** the nomenclature employed for various types of beam is as explained in section 3.3 with additional numbers (e.g. 1,2,3) at the end indicating the the serial number of identical samples. The maximum loads predicted in the numerical analysis and recorded through load cell for D1, D2 and D3 type of beams are found to be in reasonably good agreement as shown in **Tables 3.7-3.9**. Also the central deflection of beams at maximum load for D1, D2 and D3 type beams, measured in the experiment is found to be in good agreement with the numerical prediction in most of the cases as clear from **Tables 3.7-3.9**, where the legends **"**Exp" and "FEM" designate the results of experiment and finite element method respectively. "Max" and "Disp" stand for the maximum and displacement respectively.

Table 3.7 Experimental and Numerical results for D1 type beam

	Exp. Max Load-kN	**FEM. Max Load-kN**	**Exp. Disp at Max load-mm**	**FEM. Disp at Max load-mm**
D1P12.5A1	6.89		0.15	
D1P12.5A2	6.31	6.85	0.12	0.12
D1P12.5A3	6.7		0.14	
D1P12.5B2	3.89		0.115	
D1P12.5B3	3.6		0.09	
D1T12.5B2	3.77	3.1	-	0.092
D1T12.5B3	3.58		0.13	
D1P12.5C1	2.4		0.10	
D1P12.5C2	2.5		0.05	
D1P12.5C3	2.6		-	
D1T12.5C1	3.08		0.08	
D1T12.5C2	3.48	2.53	0.113	0.082
D1T12.5C3	3.15		0.108	
D1P20A2	7.5		0.061	
D1T20A2	6.49	7.24	-	0.1
D1P20B1	3.2		0.05	
D1P20B3	3.24		0.043	
D1T20B1	3.2		-	
D1T20B2	3.48	3.4	-	0.09
D1T20B3	3.24		0.09	
D1P20C1	2.7		0.11	
D1P20C2	2.69		0.053	
D1P20C3	2.73		-	
D1T20C2	2.63	2.8	0.05	0.083
D1T20C3	3.1		0.12	

Table 3.8 Experimental and Numerical results for D2 type beam

	Exp. Max Load-kN	FEM. Max Load-kN	Exp. Disp at Max load-mm	FEM. Disp at Max load-mm
D2P12.5A1	21	25	0.2	0.14
D2T12.5A2	25.2		-	
D2T12.5A3	26		-	
D2P12.5B1	10.33	10.4	0.13	0.105
D2P12.5B2	10.48		0.12	
D2P12.5B3	10.57		0.108	
D2T12.5B1	9.3		0.11	
D2T12.5B2	9.8		-	
D2T12.5B3	10.65		-	
D2P12.5C1	9.35	8.3	0.16	0.11
D2P12.5C2	8.7		0.18	
D2P12.5C3	9.7		0.13	
D2T12.5C1	7.5		0.158	
D2T12.5C3	7		-	
D2P20A1	23.7	27	-	0.17
D2P20B2	7.4	11.28	0.19	0.13
D2T20B2	9.5		0.11	
D2T20B3	9.8		-	
D2P20C2	8	9.16	0.2	0.14
D2P20C3	8		0.17	
D2T20C1	5.54		0.2	

Table 3.9 Experimental and Numerical results for D3 type beam

	Exp. Max Load-kN	FEM. Max Load-kN	Exp. Disp at Max load-mm	FEM. Disp at Max load-mm
D3T20B1	110.58	114	0.36	0.3
D3T20B2	101		0.4	
D3T20B3	103.4		0.32	
D3T20C1	98.4	93	0.28	0.25
D3T20C2	80.38		0.3	
D3T20C3	84.56		0.33	

3.6.3.3 Load-Load Point Displacement and Load-Crack Opening Displacement (COD) response

Figs. 3.14-3.15 show the response of the D1 beam cast with maximum aggregate size of 12.5 mm and 20 mm for *a/D* = 0.25. Similarly **Figs. 3.16-3.17** illustrate the response of the D1 beam cast with maximum aggregate size of 12.5 mm and 20 mm for *a/D* = 0.33. **Fig. 3.18a** and **Fig. 3.18b** show the load vs. load point displacement response of D2 beam cast with maximum aggregate size of 12.5 mm for *a/D* = 0.05 and 0.25 respectively. **Fig. 3.19a** and **Fig. 3.19b** show the load vs. COD response of D3 beam cast with maximum aggregate size of 20 mm for *a/D* =

0.25 and 0.33 respectively. D3 specimen being largest among all behaves in the brittle manner as clear from **Fig. 3.19a-b**. The details of nomenclatures used in **Figs. 3.14-3.19** are mentioned in **Table 3.10.**

In **Figs. 3.14-3.19**, the pre peak numerical responses of load vs. load line displacement curves and load-COD curves are found to be in excellent agreement with that of experimental prediction. Also in **Figs. 3.14-3.19**, the initial post peak response of numerically predicted and experimentally observed plots of load vs. load point vertical displacement and load vs. COD responses are in reasonably good agreement. RILEM approach was originated from the fictitious crack model. Therefore, fictitious crack model with an assumed softening as described in **Section 3.4** is used in the present study. RILEM approach estimates the fracture energy, for a projected ligament through load vs. load line displacement curve, in an average sense. The fracture energy is governed by failure load of the test specimen. Therefore, initial tangent on post peak response of load vs. load line displacement is plotted in a consistent manner to assess the ultimate displacement. The technique of initial tangent on post peak response (load-deflection) and the curtailment of load-deflection curve are quite common for assessment of ultimate displacement. The ultimate displacement observed from the initial tangent on post peak response of load vs. load line displacement is utilized for the evaluation of RILEM fracture energy.

Table: 3.10 Description of terms used in Figs. 3.14-3.19

D1-12.5num	Numerical result with FE mesh size ~ 8 mm of D1 cast with maximum aggregate size of 12.5 mm
D1-12.5exp1	Experimental result of I identical D1 beam cast with maximum aggregate size of 12.5 mm
D1-12.5exp2	Experimental result of II identical D1 beam cast with maximum aggregate size of 12.5 mm
D1-12.5exp3	Experimental result of III identical D1 beam cast with maximum aggregate size of 12.5 mm
D1-20num	Numerical result with FE mesh size ~ 10 mm of D1 cast with maximum aggregate size of 20 mm
D1-20exp1	Experimental result of Ist identical D1 beam cast with maximum aggregate size of 20 mm
D1-20exp2	Experimental result of Ist identical D1 beam cast with maximum aggregate size of 20 mm
D1-20exp3	Experimental result of Ist identical D1 beam cast with maximum aggregate size of 20 mm
D2-12.5num1	Numerical result with FE mesh size ~ 10 mm of D2 cast with maximum aggregate size of 12.5 mm
D2-12.5num2	Numerical result with FE mesh size ~ 12 mm of D2 cast with maximum aggregate size of 12.5 mm
D2-12.5exp	Experimental result of D2 beam cast with maximum aggregate size of 12.5 mm
D2-12.5num	Numerical result with FE mesh size ~ 12 mm of D2 cast with maximum aggregate size of 12.5 mm
D2-12.5exp1	Experimental result of I identical D2 beam cast with maximum aggregate size of 12.5 mm
D2-12.5exp2	Experimental result of II identical D2 beam cast with maximum aggregate size of 12.5 mm
D3-20num	Numerical result with FE mesh size ~ 20 mm of D3 cast with maximum aggregate size of 20 mm
D3-20exp1	Experimental result of I identical D3 beam cast with maximum aggregate size of 20 mm
D3-20exp2	Experimental result of II identical D3 beam cast with maximum aggregate size of 20 mm
D3-20exp3	Experimental result of III identical D3 beam cast with maximum aggregate size of 20 mm

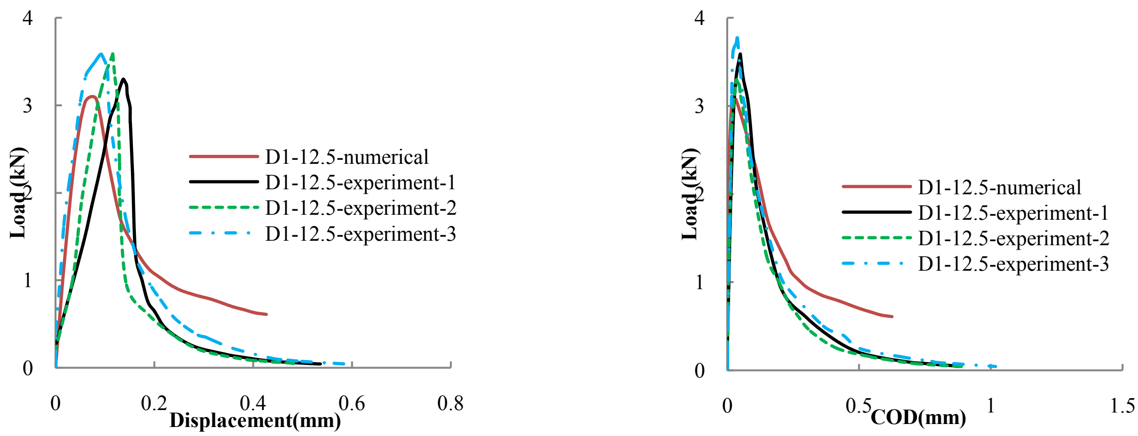

(a) (b)

Fig. 3.14 (a) load-displacement and (b) load-COD response of D1 beam for a/D = 0.25(cast with maximum aggregate size of 12.5 mm)

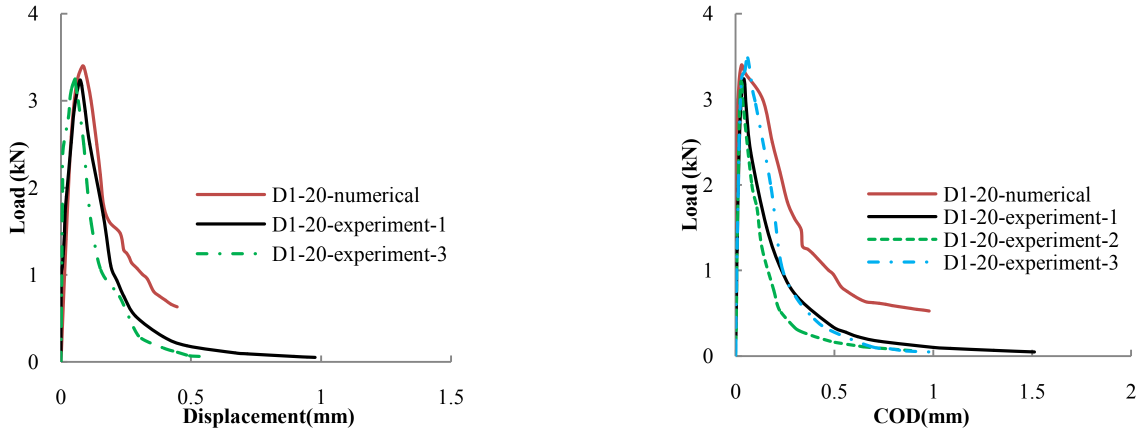

(a) (b)

Fig. 3.15 (a) load-displacement and (b) load-COD response of D1 beam for *a/D* = 0.25(cast with maximum aggregate size of 20 mm)

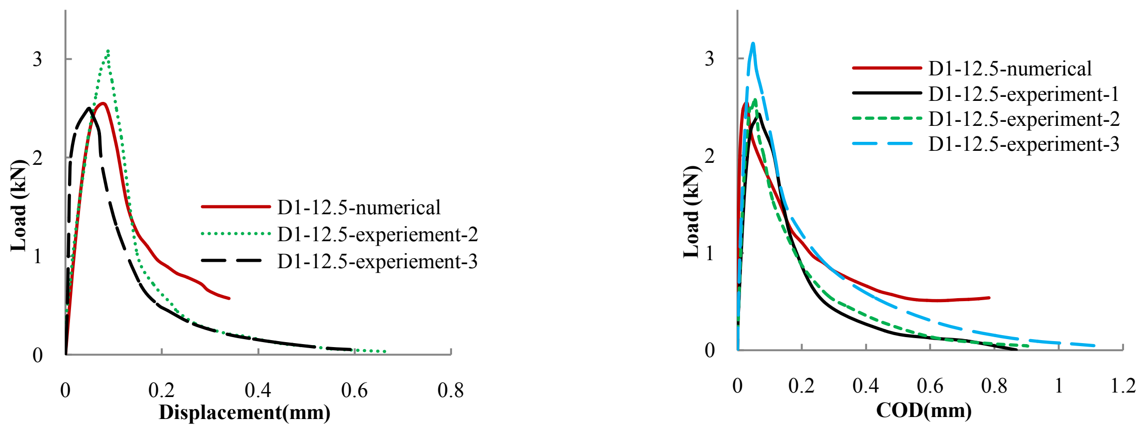

(a) (b)

Fig. 3.16 (a) load-displacement and (b) load-COD response of D1 beam for *a/D* = 0.33 (cast with maximum aggregate size of 12.5 mm)

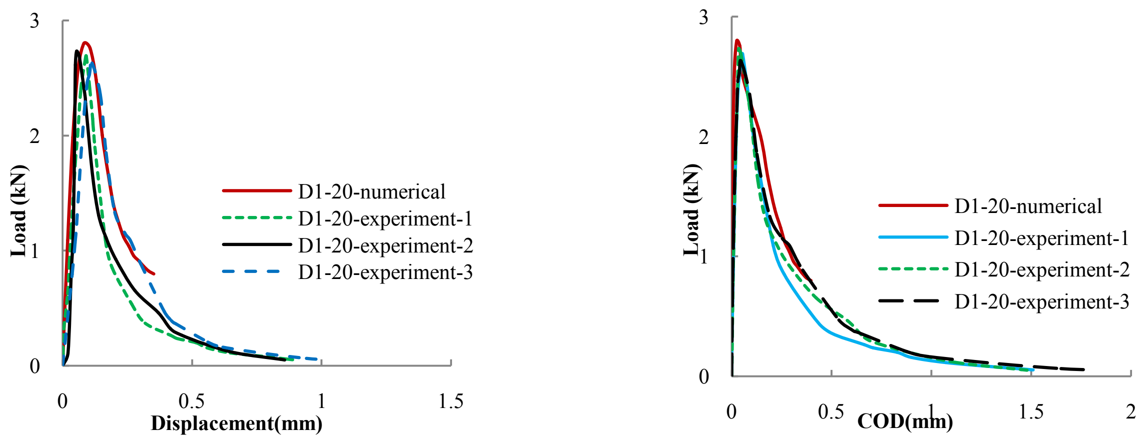

(a) (b)

Fig. 3.17 (a) load-displacement and (b) load-COD response of D1 beam for *a/D* = 0.33 (cast with maximum aggregate size of 20 mm)

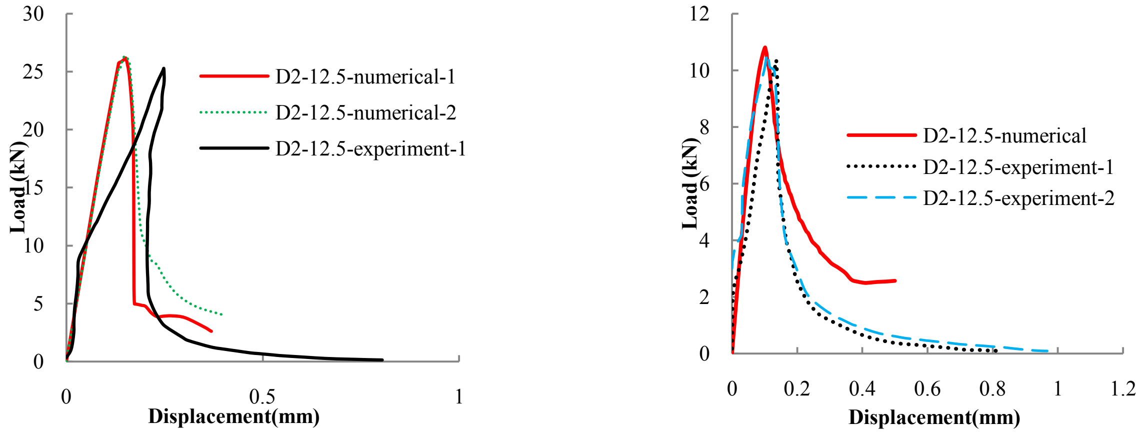

(a) (b)

Fig. 3.18. Load-displacement response of D2 beam (cast with maximum aggregate size of 20 mm) for (a) *a/D* = 0.05 and (b) *a/D* = 0.25

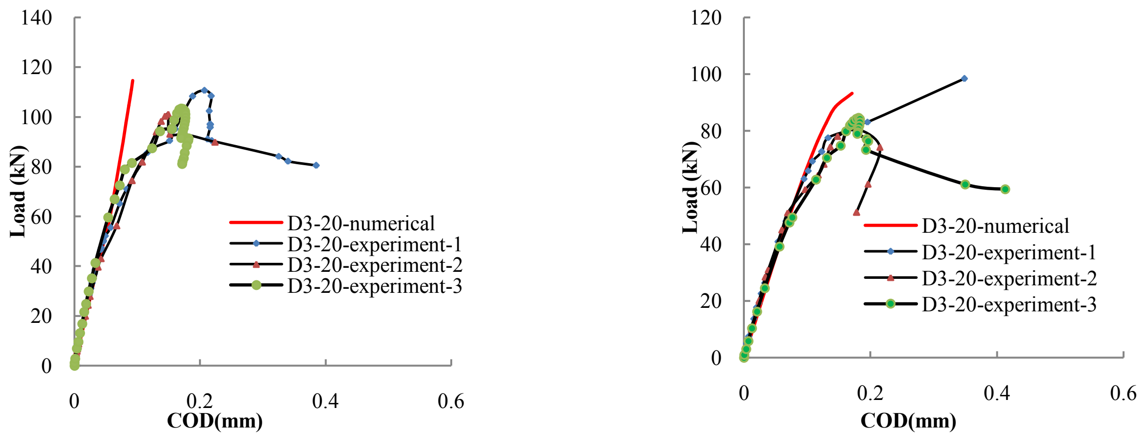

(a) (b)

Fig. 3.19 Load-COD response of D3 beam for (a) *a/D* = 0.25 and (b) *a/D* = 0.33

3.7 Chapter closure

A number of two dimensional numerical simulations of TPB specimens have been performed by non linear FEA to characterize the concrete fracture phenomenon. The performance of triangular elements has been investigated, and observed to be superior to the quadrilateral elements for the simulations of concrete fracture behavior in TPB specimens. Mesh sensitivity, which is an extremely important issue in concrete due to its post peak softening, has been addressed. RILEM fracture energy values evaluated from load vs. load line displacement curve of TPB specimens shows size effects as presented in next chapter. Therefore, next chapter mainly deals with the investigation of size independent fracture energy of concrete.

Chapter 4

ASSESSMENT OF SIZE INDEPENDENT FRACTURE ENERGY

4.1 Theoretical background

The fracture energy of concrete is the most important parameter in the fracture behaviour of concrete that describes the mechanism of cracking. The commonly used method for measuring the fracture energy is the work of fracture method recommended by RILEM **[Shah et. al. (1995), Bazant and Planas (1998)]** which suffers from size effect. Hence it is important to investigate the fracture energy which is free from size effect. The local fracture energy model **[Duan et. al. (2003)** and **Wittmann (2002)]** is the popular method for measuring the size independent fracture energy of concrete. The other two methods based on energy release rate and averaging RILEM fracture energy values are developed for the evaluation of the size independent fracture energy of concrete. Brief descriptions of three methods follow:

4.1.1 Proposed methodology using RILEM fracture test

RILEM technical committee recommended the guidelines for determination of fracture energy of cementitious materials by conducting TPB test on notched beam **[Shah et. al. (1995),** and **Shailendra** and **Barai (2011)]** as shown in **Fig.3.1**. The fracture behaviour of concrete characterized by the RILEM measures the averaged fracture energy over the entire projected ligament area. According to RILEM recommendation, the fracture energy (G_f) is evaluated by dividing the total applied energy with the projected ligament area. Therefore, for a specimen with a depth D and an initial crack length a as shown in **Fig. 3.1**, the G_f is given as:

$$G_f(\alpha, D) = \frac{1}{(D-a)t} \int P d\delta \qquad \text{Eq. (4.1)}$$

where, t is the specimen thickness, $\alpha = a/D$, P is the applied load and δ is the displacement at the loading point. Let us consider geometrically similar TPB specimens with depth D_1, D_2.....D_n. Each specimen having different notch to depth ratios as: $\alpha = \alpha_1$, α_2.....α_m. The α values are to be chosen in such a way that the crack tip is sufficiently away from the boundary. In other words, α value should not be too small or high **[Duan et. al. (2003)]**. RILEM fracture energy values suffers from size effect. The size independent average fracture energy G_F is approximated as:

$$G_F(average) = \frac{1}{mn}\left[\sum_{i=1}^{m}\sum_{j=1}^{n} G_f(\alpha_i, D_j)\right] \qquad \text{Eq. (4.2)}$$

Using the proposed **Eq. 4.2** the size independent fracture energy for around 40 TPB specimens with $\alpha = 0.25$ and 0.33 is estimated and % Coefficient of Variance (COV) is shown in results.

4.1.2 Bi-linear approximation

In bi-linear approximation, the fracture energy at crack tip known as local fracture energy (g_f) is assumed to vary with ligament in a bilinear manner. Local fracture energy method addressed the effect of the free boundary of the specimen on the fracture process zone ahead of a real crack in a concrete structure **[Duan et. al. (2003), Karihaloo (2003) and Cifuentes et. al. (2013)]**. The energy required to create a fresh crack decreases as the crack approaches the free boundary. Initially, when the crack grows from a pre-existing notch, the rate of decrease is moderate, almost a constant, but it accelerates as the crack approaches the end of the un-cracked ligament as reported by **Karihaloo (2003) and Cifuentes et. al. (2013)**. The local fracture energy and the FPZ size were found to decrease rapidly as the crack approaches the back surface of the specimen. The maximum FPZ size is attained when the crack is far away from the boundary. In a large specimen, a region ahead of crack tip exists where the FPZ size is relatively constant resulting in a constant g_f (or G_F). A bilinear approximation is represented in **Fig.4.1** to simplify the boundary-induced reduction in the fracture energy. This bilinear function consists of a horizontal line with the value of the size independent fracture energy and a descending branch that reduces to zero at the back surface of the specimen. G_F shows a transition from a constant value to the rapid decrease at the transition ligament length a_l^*, which is given by the intersection of these two lines. On the basis of the boundary effect method of **Wittmann (2002)**, the measured RILEM fracture energy (G_f) represents the average of the local fracture energy function over the ligament area (dotted line in **Fig.4.1**). The relationship between all the involved variables is given by:

$$G_f(a/D) = \frac{\int_0^{D-a} g_f(x)dx}{D-a} = G_F\left[1 - \frac{a_l^*/D}{2(1-a/D)}\right] \qquad 1 - a/D > a_l^*/D \qquad \text{Eq. (4.3)}$$

$$G_f(a/D) = \frac{\int_0^{D-a} g_f(x)dx}{D-a} = G_F\frac{1-a/D}{2a_l^*/D} \qquad 1 - a/D \le a_l^*/D \qquad \text{Eq. (4.4)}$$

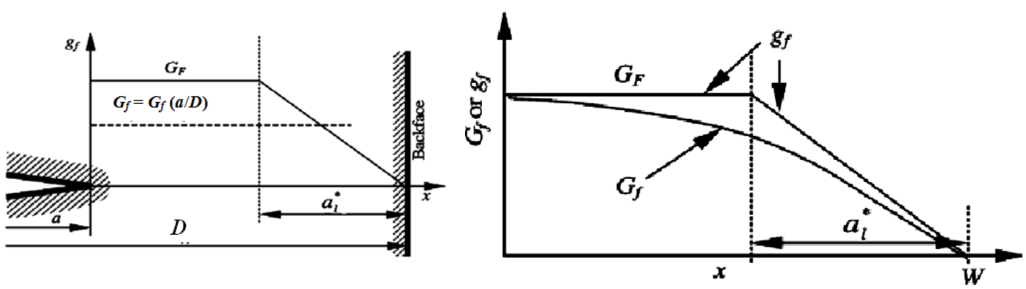

Fig.4.1 Local fracture energy model of **Wittmann (2002)**

where, D is the total depth of the specimens and a is the initial notch depth. To obtain the values of G_F of a concrete, G_f of the specimens of different sizes for a range of the notch to depth (a/D) ratios is first determined using **Eqs.4.3-4.4**. The number of the measured $G_f(a/D)$ values is, therefore, much larger than the two unknowns, G_F and a^*_l in **Eqs.4.3-4.4**. This gives an over-determined system of equations which are solved by a least square method to obtain the best estimates of G_F and is shown later in this chapter.

4.1.3 Energy release rate

Although the size independent fracture energy can be estimated by extrapolating the results of research investigations on laboratory size specimens but the range of specimen sizes is still being debated among various researchers. The concrete material ahead of crack tip develops relatively large FPZ which undergoes progressive softening due to micro-cracking. The assumption made in this approach is that the fracture energy is dissipated in the fracture process zone which exists in the uncracked ligament of TPB specimens as reported by **Muralidhara (2010)**. Based on the RILEM fracture energy values for various *a/D* ratios, a relationship between fracture energy release rate and the uncracked ligament length is developed to estimate G_F. From the developed relationship, the fracture energy is found to reach almost a constant value implying that the fracture energy remains almost constant at larger ligament lengths. In other words, when ligament length becomes sufficiently large to accommodate the fully developed FPZ, fracture energy becomes constant being independent of specimen size and *a/D*. The fracture energy is proportional to the length of the FPZ size (l_{FPZ}) for a given strength of concrete assuming constant width of FPZ. The relationship is given as:

$$G_f \;\alpha\; l_{FPZ} \qquad \text{Eq. (4.5)}$$

Similarly uncracked ligament length: $(D- a)\ \alpha\ D$ Eq. (4.6)

From **Eqs.4.5-4.6**;

$$\frac{G_f}{D-a} = k\frac{l_{FPZ}}{D}$$

where k is a constant, and $\frac{G_f}{D-a}$ is proportional to $\frac{l_{FPZ}}{D}$. A curve of $\frac{G_f}{D-a}$ versus $(D- a)$ is plotted (**Fig.4.2**) from the RILEM fracture energy values and plot is observed to follow a power law and almost asymptotic with the axis representing $(D- a)$ for larger values of $(D- a)$. The equation of the curve is:

$$\frac{G_f}{D-a} = C(D-a)^{-b} \qquad \text{Eq. (4.7)}$$

In which C and b are constants. As the un-cracked ligament length increases $G_f/(D-a)$ almost attains a constant value as is clear from **Fig.4.2**. The size independent fracture energy is estimated by the expression **[Muralidhara et. al. (2013)]**:

$$G_F = \left[\frac{G_f}{D-a}\right]_{(D-a=l\arg e)} (D-a)_{L\arg e} \qquad \text{Eq. (4.8)}$$

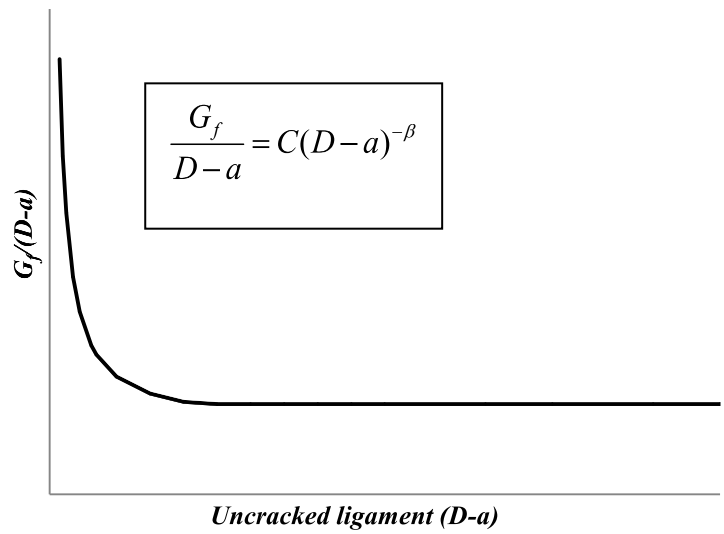

Fig.4.2 Typical curve following the power law

4.2 RILEM fracture energy values

The RILEM fracture test on geometrically similar (constant length to depth ratio) TPB plain concrete beams were conducted by **Raghu Prasad (2009)** and **Muralidhara (2010)**. The present work involves the numerical modelling of those tested TPB beams for investigation of size independent fracture energy. Finite element method with CST elements is adopted for analyses of the concrete beams. The material behaviour is incorporated by smeared crack approach based on fracture energy cracking criterion in the analysis as explained in previous chapter using **Table 3.4**. The finite element modelling of the TPB geometrical specimens (**Table 3.2**) with the a/D = 0.05, 0.25 and 0.33 have been carried out. The nomenclature employed for various types of beam in **Table 4.1-4.3** is same as that explained in **Chapter 3**. Based on the numerically predicted and experimentally observed load vs. load point displacement response of TPB specimens shown in previous chapter, the RILEM fracture energy (G_f) values are evaluated. The fracture energy is governed by failure load of the test specimen. Therefore, initial tangent on post peak response of load vs. load line displacement is plotted in a consistent manner to assess the ultimate displacement, which is utilized for the evaluation of RILEM fracture energy. The fracture energy estimated through the load vs. load line displacement response obtained from the finite element simulation and set of experiments for D1, D2 and D3 type beam is presented in **Tables 4.1-4.3** where, the **"**Exp" and "FEM" designate the results of experiment and finite element method respectively. RILEM fracture energy values are observed to be size dependent as is clear from **Tables 4.1-4.3**.

Table 4.1 Experimental and Numerical results for D1 type beam

	Exp G_f**(N/m)**	**FEM** G_f**(N/m)**
D1P12.5A1	212	213
D1P12.5A2	-	
D1P12.5A3	-	
D1P12.5B2	122	136
D1P12.5B3	116	
D1T12.5B2		
D1T12.5B3	162	
D1P12.5C1	107	130
D1P12.5C2	121	
D1P12.5C3	-	
D1T12.5C1	142	
D1T12.5C2	150	
D1T12.5C3	144	
D1P20A2	-	240
D1T20A2	-	
D1P20B1	212	154
D1P20B3	185	
D1T20B1	-	
D1T20B2	-	
D1T20B3	146	
D1P20C1	153	152
D1P20C2	159	
D1P20C3	-	
D1T20C2	-	
D1T20C3	137	

Table 4.2 Experimental and Numerical results for D2 type beam

	Exp G_f**(N/m)**	**FEM** G_f**(N/m)**
D2P12.5A1	-	200
D2T12.5A2	-	
D2T12.5A3	-	
D2P12.5B1	130	121
D2P12.5B2	114	
D2P12.5B3	141	
D2T12.5B1	122	
D2T12.5B2	-	
D2T12.5B3	-	
D2P12.5C1	132	113
D2P12.5C2	125	
D2P12.5C3	135	
D2T12.5C1	140	
D2T12.5C3	-	
D2P20A1	-	226
D2P20B2	144	123
D2T20B2	151	
D2T20B3	-	
D2P20C2	140	118
D2P20C3	158	
D2T20C1	85	

Table 4.3 Experimental and Numerical results for D3 type beam

	Exp G_f**(N/m)**	**FEM** G_f**(N/m)**
D3T20B1	168	83
D3T20B2	109	
D3T20B3	124	
D3T20C1	145	64
D3T20C2	95	
D3T20C3	141	

4.3 Size independent fracture energy: Averaging of G_f

The limited number of D3 specimens were tested due to its heavy weight and handling issues. Hence, focus has been put mainly on D1 and D2 beams having plenty of data sets to estimate the size independent fracture energy. Too small *a/D* and too large *a/D* are not preferable for concrete fracture test, which is reported in literature by **Duan et. al. (2003)**. Since the *a/D* = 0.25 and 0.33 ensures crack tip away from the boundary; it is, therefore best suited to estimate the size independent fracture energy. RILEM fracture energy predicted numerically and experimentally is presented in **Fig.4.3**. Averaging the numerical values of RILEM fracture energy of all the specimens with *a/D* = 0.25 and 0.33, G_F is found to be 134 N/m and 128 N/m respectively shown in **Table 4.4**. Similarly the various band of the size independent fracture energy along with COV are estimated by averaging the RILEM fracture energy presented in **Table 4.4**.

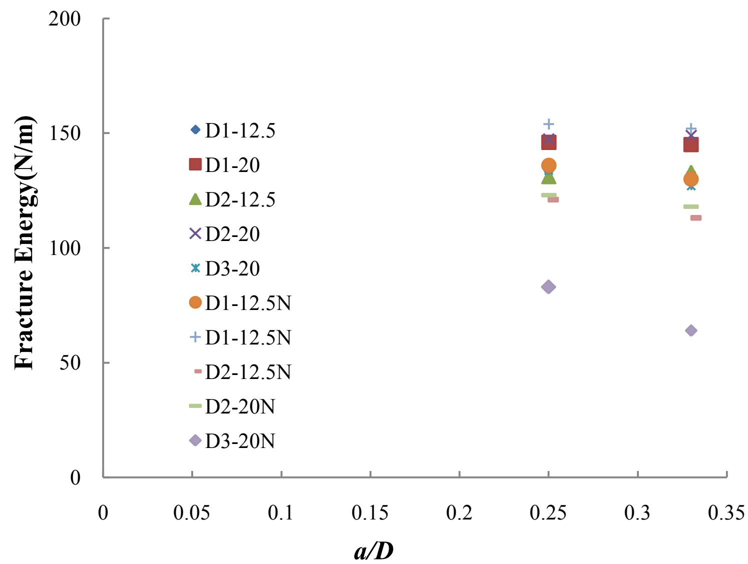

Fig. 4.3 Experimentally and numerically observed RILEM fracture energy considering all data sets

Table 4.4: Assessment of size independent fracture energy (G_F)

Combinations	**Mean fracture energy(N/m) =G_F and Coefficient of variation = COV**			
	***a/D* = 0.25**		***a/D* = 0.33**	
	G_F	**% COV**	**G_F**	**% COV**
All Numerical results	134	11.5	128	13.7
Numerical results excluding D3	123	21	115	28
All experimental results	145	8.6	139	10
Experimental results excluding outliers	138	5.5	137	6.7
Experimental results excluding outliers and D3	139	5.8	140	5.8
Experimental and Numerical results	131	15	126	20
Experimental and Numerical results excluding outliers and D3	136	11	134	10

4.4 Size Independent fracture energy: Bilinear approximation

The RILEM fracture energy for around 49 beam specimens having three different depths and three different *a/D* ratios are determined as illustrated in **section 4.1** using **Eq. 4.1** . In **Eqs. 4.3-**

4.4 the number of unknowns are two, namely, G_F and a^*_l, whereas the measured $G_f(a/D)$ values are more. For this reason, the over determined system of equations is solved by a least square method to obtain the best estimates of G_F. **Tables 4.5-4.7** show the G_F values with COV for various combinations of *a/D* values. Too small *a/D* is not preferable for concrete fracture test as reported in literature **[Duan et. al. (2003)]** which is clear from **Table 4.7** where the G_F value for *a/D* =0.05 is observed to be 215 N/m with high COV.

Table 4.5: Estimated G_F from experimental G_f including all outlier

***D*-mm**	**G_f (N/m) values for *a/D*=0.25**	**G_f (N/m) values for *a/D*= 0.33**	**G_f (N/m) values for *a/D*= 0.25 and 0.33**
94	122,116,162, 212,185,188,89	107,121,170,142,150, 144,153,159,164,137	122,116,162, 212,185,188,89, 107, 121,170,142,150,144,153,159,164,137
188	112,114,141,122, 174,198,144,151,190	132,125,135,140, 159,140,158,85	112,114,141,122,174,198,144,151,190, 132,125,135,140,159,140,158,85
750	168,109,124	145,95,141	168,109,124, 145,95,141
G_F (N/m)	137	124	132
% COV	18	11.4	10.7

Table 4.6: Estimated G_F from experimental G_f excluding outlier

***D*-mm**	**G_f (N/m) values for *a/D*= 0.25**	**G_f (N/m) values for *a/D*= 0.33**	**G_f (N/m) values for *a/D*= 0.05, 0.25 and 0.33**	**G_f (N/m) range for *a/D*= 0.25 and 0.33**
94	122,116,162, 212,185	107,121,142,150, 144,153,159,137	212,179,122,116,162, 212,185,107,121,142, 150,144,153,159,137	122,116,162, 212,185,107,121,142, 150,144,153,159,137
188	114,141,122,144, 151	132,125,135,140, 158,85	114,141,122,144,151, 132,125,135,140,158, 85	114,141,122,144,151, 132,125,135,140,158,8 5
750	168,109,124	145,95,141	168,109,124, 145,95,141	168,109,124, 145,95,141
G_F (N/m)	124	124	127	126
% COV	18	11.4	11	11.2

Table 4.7: Estimated G_F from experimental G_f and FEA G_f excluding outlier

***D*-mm**	**G_f (N/m) values for *a/D*= 0.05**	**G_f (N/m) values for *a/D*= 0.25**	**G_f (N/m) values for *a/D*= 0.33**	**G_f (N/m) values for *a/D*= 0.05, 0.25 and 0.33**	**G_f (N/m) values for *a/D*= 0.25 and 0.33**
94	213,240, 212,179	136,154, 122,116, 162,212, 185	130,152,107, 121,142,150, 144,153,159, 137	213,240,212,179, 136,154,122,116, 162,212,185,130,152, 107,121,142,150,144, 153,159,137	136,154,122,116, 162,212,185,130, 152,107,121,142, 150,144,153,159, 137
188	200,226	121,123,114, 141,122, 144,151	113,118,132, 125,135,140, 158,85	200,226,121,123,114, 141,122,144,151,113, 118,132,125,135,140, 158,85	121,123,114,141, 122,144,151,113, 118,132,125,135, 140,158,85
750	-	83,168, 109,124	64,145,95, 141	83,168,109,124, 64,145,95,141	83,168,109,124, 64,145,95,141
G_F (N/m)	215	113	110	125	113
% COV	23	15	12.8	12.4	10

4.5 Size Independent fracture energy: Energy release rate

The estimated RILEM fracture energy (G_f) and $\frac{G_f}{D-a}$ values of about 49 beams, having three different depths and three different *a/D* ratios (**Table 3.2)**, are shown in **Table 4.8**. The size independent fracture energy G_F is evaluated based on the relationship between $\frac{G_f}{D-a}$ versus (D - a). $\frac{G_f}{D-a}$ Versus (D - a) data points are plotted and relationship between them is derived. **Fig.4.4a** depicts the relationship between $G_f/(D- a)$ and ($D- a$) from experimental and FEA data sets of G_f whereas **Fig. 4.4b** illustrates the same for experimental data sets of G_f only. Two power law equations generated by best fit of these data in **Figs. 4.4a-b** are as follows:

$$\frac{G_f}{D-a} = 260.7 * (D-a)^{-1.13} \qquad \text{Eq. (4.9)}$$

$$\frac{G_f}{D-a} = 192.9 * (D-a)^{-1.06} \qquad \text{Eq. (4.10)}$$

From the $\frac{G_f}{D-a}$ versus (D- a) data, slope $\frac{d(G_f/(D-a))}{d(D-a)}$ is calculated by differentiating **Eqs.4.9-4.10**, which are extrapolated beyond test range till (D - a) = 1800. **Tables 4.9-4.10** show the values of slope and fracture energy for different ligament lengths (D - a) for the datasets in **Figs.4.4a-b** respectively. Data of **Tables 4.9-4.10** are plotted in the form of variation of $\frac{d(G_f/(D-a))}{d(D-a)}$ versus (D - a) and shown in **Fig. 4.5a-b**. From **Fig. 4.5a-b**, the rate of decrease of slope of the curve approaches to almost zero and hence the G_f/ (D - a) (i.e. fracture energy release rate) is considered almost constant at large values of (D - a). This implies that the fracture energy variation over larger values of (D - a) is negligibly small. In other words, the fracture energy reaches almost a constant value. This is due to the fact that when ligament length becomes sufficiently large to accommodate the fully developed FPZ, fracture energy becomes constant being independent of specimen size and *a/D*. From **Fig. 4.5a-b** it is clear that the slope almost tends to zero for ligament (D - a) size of around 1000 mm.

Table 4.8: Numerically and experimentally observed values of G_f *and* $G_f/D\text{-}a$

	Beam type	***a/D***	***D-a* (mm)**	**G_f (N/m)**	**G_f/D-a(N/m^2)**
FEA	D1P12.5A	**0.05**	89.3	213	2.385218
	D1P12.5B	**0.25**	70.5	136	1.929078
	D1P12.5C	**0.33**	62.98	130	2.064147
	D1P20A	**0.05**	89.3	240	2.68757
	D1T20B	**0.25**	70.5	154	2.184397
	D1P20C	**0.33**	62.98	152	2.413465
	D2T12.5A	**0.05**	178.6	200	1.119821
	D2T12.5B	**0.25**	141	121	0.858156
	D2P12.5C	**0.33**	125.96	113	0.89711
	D2P20A	**0.05**	178.6	226	1.265398
	D2P20B	**0.25**	141	123	0.87234
	D2T20C	**0.33**	125.96	118	0.936805
	D3T20B	**0.25**	562.5	83	0.147556
	D3T20C	**0.33**	502.5	64	0.127363
Experimental	D1P12.5A1	**0.05**	89.3	212	2.37402
	D1P12.5A2	**0.05**	89.3	179	2.004479
	D1P12.5B2	**0.25**	70.5	122	1.730496
	D1P12.5B3	**0.25**	70.5	116	1.64539
	D1T12.5B3	**0.25**	70.5	162	2.297872
	D1P20B1	**0.25**	70.5	212	3.007092
	D1P20B3	**0.25**	70.5	185	2.624113
	D1T20B3	**0.25**	70.5	146	2.070922
	D1P12.5C1	**0.33**	62.98	107	1.698952
	D1P12.5C2	**0.33**	62.98	121	1.921245
	D1T12.5C1	**0.33**	62.98	142	2.254684
	D1T12.5C2	**0.33**	62.98	150	2.381708
	D1T12.5C3	**0.33**	62.98	144	2.28644
	D1P20C1	**0.33**	62.98	153	2.429343
	D1P20C2	**0.33**	62.98	159	2.524611
	D1T20C3	**0.33**	62.98	137	2.175294
	D2P12.5B2	**0.25**	141	114	0.808511
	D2P12.5B3	**0.25**	141	141	1
	D2T12.5B1	**0.25**	141	122	0.865248
	D2P12.5B1	**0.25**	141	130	0.921986
	D2P20B2	**0.25**	141	144	1.021277
	D2T20B2	**0.25**	141	151	1.070922
	D2P12.5C1	**0.33**	125.96	132	1.047952
	D2P12.5C2	**0.33**	125.96	125	0.992379
	D2P12.5C3	**0.33**	125.96	135	1.071769
	D2T12.5C1	**0.33**	125.96	140	1.111464
	D2P20C2	**0.33**	125.96	140	1.111464
	D2P20C3	**0.33**	125.96	158	1.254366
	D2T20C1	**0.33**	125.96	85	0.674817
	D3T20B1	**0.25**	562.5	168	0.298667
	D3T20B2	**0.25**	562.5	109	0.193778
	D3T20B3	**0.25**	562.5	124	0.220444
	D3T20C1	**0.33**	502.5	145	0.288557
	D3T20C2	**0.33**	502.5	95	0.189055
	D3T20C3	**0.33**	502.5	141	0.280597

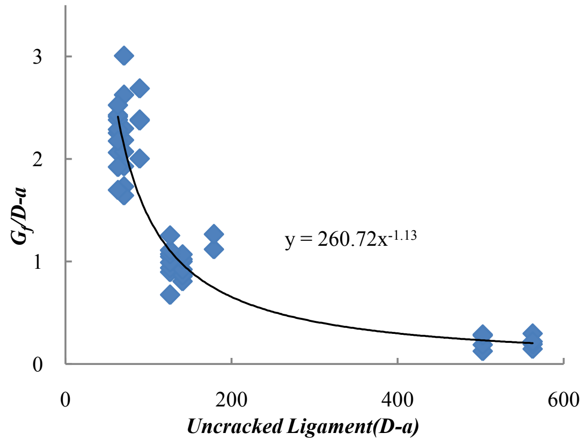

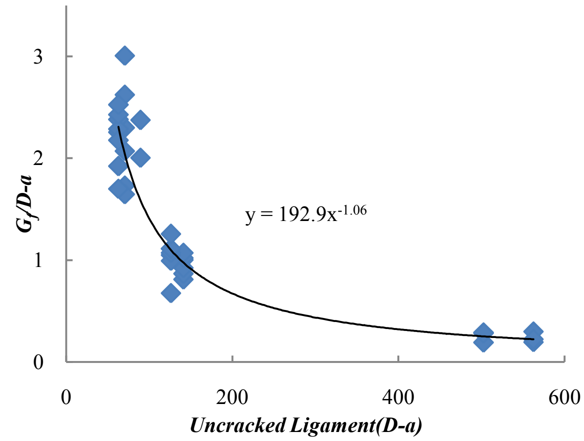

(a) (b)

Fig.4.4 Plot of $G_f/(D-a)$ versus $(D-a)$ consisting (a) Experimental and FEA G_f data (b) Purely experimental G_f data

Table 4.9: Values of slope and fracture energy for different values of ligament length using the curve in Fig. 4.4a.

***D-a* (mm)**	***G_f* (N/m)**	***G_f/D-a* (N/m^2)**	***d{G_f/D-a}/d(D-a)* (N/m^3)**
40	161.3887	4.034719	-0.08992
50	156.7743	3.135486	-0.04959
70	150.0646	2.14378	-0.0265
90	145.2411	1.61379	-0.0143
125	139.1691	1.113353	-0.00892
140	137.1338	0.979527	-0.00542
200	130.9203	0.654602	-0.00241
300	124.1982	0.413994	-0.00115
400	119.6391	0.299098	-0.00067
500	116.2184	0.232437	-0.00043
600	113.4962	0.18916	-0.0003
700	111.2444	0.158921	-0.00022
800	109.33	0.136662	-0.00017
900	107.6687	0.119632	-0.00013
1000	106.204	0.106204	-9.1E-05
1300	102.6428	0.078956	-5.9E-05
1500	100.751	0.067167	-4.2E-05

Table 4.10: Values of slope and fracture energy for different values of ligament length using the curve in Fig. 4.4b.

***D-a* (mm)**	***G_f* (N/m)**	***G_f/D-a* (N/m^2)**	***d{G_f/D-a}/d(D-a)* (N/m^3)**
40	154.5997	3.864992	-0.08141
50	152.5436	3.050872	-0.04576
70	149.4949	2.135641	-0.02497
90	147.2576	1.636195	-0.01375
125	144.3835	1.155068	-0.00872
140	143.4051	1.024322	-0.00537
200	140.3687	0.701844	-0.00245
300	136.9951	0.45665	-0.0012
400	134.6507	0.336627	-0.00071
500	132.8599	0.26572	-0.00047
600	131.4145	0.219024	-0.00033
700	130.2046	0.186007	-0.00025
800	129.1656	0.161457	-0.00019
900	128.256	0.142507	-0.00015
1000	127.4478	0.127448	-0.0001
1300	125.4572	0.096506	-6.8E-05
1500	124.3846	0.082923	-4.9E-05
1800	123.0314	0.068351	-3.6E-05

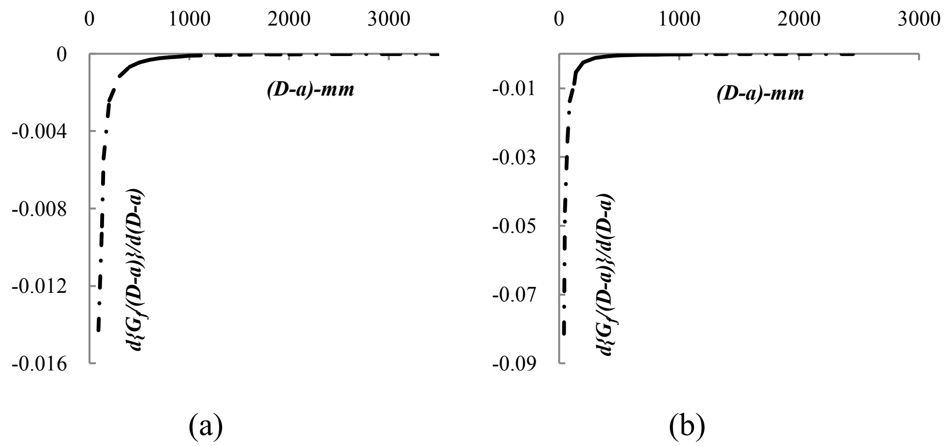

Fig.4.5 A plot of $d\{G_f/(D\text{-}a)\}/d(D\text{-}a)$ versus *(D-a)* from the results of (a) Table 4.9 (b) Table 4.10

4.6 Chapter observations and closure

The range of size independent fracture energy (G_F) from the bi-linear approximation is observed to be in range 113-126 N/m. Through the concept of energy release rate, G_F is estimated to be in a range of 106-125 N/m which is valid beyond the test range (up-to 2000 mm). Another approach, based on averaging of RILEM fracture energy, evaluates G_F in a range of 126-136 N/m. It is seen that fracture energy values evaluated by these three different methods are reasonably close to each other. The prediction of fracture parameters based on various size effect laws are shown in next chapter.

Chapter 5

PREDICTION OF FRACTURE PARAMETERS THROUGH SIZE EFFECT

5.1 Introduction to size effect law

The structural size effect is the most important issue in the fracture mechanics of quasi-brittle material. Therefore, it is important to relate the size effect behavior to the fracture properties of material. The size effect law for geometrically similar specimens containing a pre-existing stress free crack represents a smooth transition from a horizontal line for small sizes (corresponding to plasticity or strength theory) to an inclined asymptote of slope (-1/2) for large-sizes (corresponding to LEFM). It is expressed by the Bazant size effect law **[Bazant (1985), Shah et. al. (1995)** and **Bazant** and **Planas (1998)]**:

$$\sigma_{Nu} = \frac{Bf_t}{\sqrt{1+\frac{D}{D_0}}} \qquad \text{Eq.(5.1)}$$

Here, σ_{Nu} is the nominal stress at failure of a structure. Bf_t and the transitional structure size D_0 are empirical parameters to be identified by optimum fitting of measured σ_{Nu} values over a broad size range. The coefficients of **Eq.5.1** have been shown to be approximately related to the LEFM fracture characteristics as follows **[Bazant (1985), Shah et. al. (1995)** and **Bazant** and **Planas (1998)]**:

$$\sigma_{Nu} = \sqrt{\frac{EG_f}{g_0' c_f + g_0 D}} \qquad \text{Eq. (5.2)}$$

in which $g_0 = g(\alpha_0) = k_0^2$ = dimensionless energy release rate function of linear elastic fracture mechanics (LEFM) and $g'_0 = g'(\alpha_0) = 2k_0k'_0$, $k_0 = k(\alpha_0)$. The function $k(\alpha)$ introduces the effect of geometry. The nominal strength is measured from the size effect tests. Further, the fracture parameters can be estimated using the above equations and are expressed in terms of size effect parameters Bf_t, D_0 and LEFM function $g(\alpha_0)$ as:

$$G_f = \frac{K_{Ic}^2}{E} = \frac{(Bf_t)^2 D_0 k_0^2}{E}$$

$$c_f = \frac{k_0}{2k_0'} D_0$$

$$K_{Ic} = Bf_t \sqrt{D_0 k_0} \qquad \text{Eq. (5.3)}$$

where G_f, c_f and K_{Ic} are fracture energy, effective length of fracture process zone and critical stress intensity factor. The size effect involves the testing of a number of geometrically similar notched specimens for the estimation of peak load. RILEM recommended that the size effect can be analyzed by Bazant size effect laws and Jenq-Shah model. Based on this, the fracture parameters can be estimated using the **Eq**. **5.3**. The assessment of fracture parameters from Bazant size effect laws based on the analysis of linear regression I, linear regression II, and weighted linear regression and Jenq-Shah model are as discussed below.

5.1.1 Linear regression I and II based on Bazant size effect law

The linear regression I and linear regression II are the best approach to identify the empirical parameters D_0 and Bf_t. The dependency of nominal strength σ_{Nu} on characteristic dimension of specimen D for geometrically similar structure is estimated from the size effect experiments. From measurement, a series of nominal strength values σ_{Nuk} corresponding to the sizes D_k (for k = 1,2,…n, where n is number of test conducted) can be estimated. The size effect can be algebraically rearranged to linear regressions I as follow **[Bazant (1985), Bazant** and **Planas (1998)]**:

$$Y = AX + C \qquad \text{Eq. (5.4)}$$

In which $X = D$; $Y = (1/\sigma_{Nu}^2)$; $Bf_t = 1/\sqrt{C}$; $D_0 = C/A$. From **Eq**. **5.3** the fracture parameters are expressed as:

$$K_{Ic} = k_0 \frac{1}{\sqrt{A}} \qquad G_f = \frac{k_0^2}{E}\left(\frac{1}{A}\right) \qquad c_f = \frac{k_0}{2k_0'}\left(\frac{C}{A}\right) \qquad \text{Eq. (5.5)}$$

Another algebraic rearrangement of size effect from linear regression II is as follow :

$$Y' = A'X' + C' \qquad \text{Eq. (5.1.3)}$$

In which $X' = (1/D')$; $Y = (1/(\sigma_{Nu}^2 D'))$; $Bf_t = 1/\sqrt{A'}$; $D_0 = A'/C'$. From **Eq**. **5.3** the fracture parameters are expressed as:

$$K_{Ic} = k_0 \frac{1}{\sqrt{C'}} \qquad G_f = \frac{k_0^2}{E}\left(\frac{1}{C'}\right) \qquad c_f = \frac{k_0}{2k_0'}\left(\frac{A'}{C'}\right) \qquad \text{Eq. (5.6)}$$

5.1.2 Weighted linear regression based on Bazant size effect law

The maximum load $P_1, P_2 \ldots P_n$ for the specimens of various sizes of $D_1, D_2 \ldots D_n$ are required to estimate the fracture parameters. The P_1^0, P_2^0……….. P_n^0 are the corrected maximum load by taking in account the weight of the specimen. Here n is the number of test conducted. For j = 1,2…..n, a linear regression $Y = A_B X + C_B$ **[Shah et. al. (1995)]** can be plotted by introducing the X_j , Y_j , the slope A_B and the intercept C_B given as :

$$Y_j = \left(\frac{D_j t}{P_j^0}\right)^2 \qquad X_j = D_j \qquad \text{Eq. (5.7)}$$

$$A_B = \frac{\sum_{j=1}^{n}\left(X_j - \overline{X}\right)\left(Y_j - \overline{Y}\right)}{\sum_{j=1}^{n}\left(X_j - \overline{X}\right)^2} \qquad \text{Eq. (5.8)}$$

$$C_B = \overline{Y} - A_B \overline{X} \qquad \text{Eq. (5.9)}$$

$$\bar{X} = \frac{1}{n}\sum_{j=1}^{n} X_j \qquad \bar{Y} = \frac{1}{n}\sum_{j=1}^{n} Y_j \qquad \text{Eq. (5.10)}$$

Where the **Eq**. **5.10** represents the centroid of all data points. The geometric factor $g(\alpha_0)$ is calculated as:

$$g(\alpha_0) = \left(\frac{S}{D}\right)^2 \pi\alpha_0[1.5g_1(\alpha_0)]^2 \qquad \text{Eq. (5.11)}$$

Where $\alpha_0 = a/D$ and S is span of beam. The value of $g_1(\alpha_0)$ is determined based on ratios of S/D and is available **[Shah et. al. (1995) and Bazant** and **Planas (1998)]**. The values of material fracture energy G_f is determined as:

$$G_f = \frac{g(\alpha_0)}{EA_B} \qquad \text{Eq. (5.12)}$$

The length of FPZ for an infinitely large specimen c_f is further obtained as:

$$c_f = \frac{g(\alpha_0)}{g'(\alpha_0)}\left(\frac{C_B}{A_B}\right) \qquad \text{Eq. (5.13)}$$

where $g'(\alpha_0)$ is the value of the first derivative of $g(\alpha_0)$ with respect to at $a = a_0$. The statistical calculations are required to estimate the coefficient of variation of the slope of the regression line, ω_A, and the relative width of the scatter band ‘m’ which are estimated and shown in results.

5.1.3 Size effect from Jenq and Shah model

Jenq and Shah proposed an equivalent crack model [**Shah et. al. (1995)**] which predicts the peak load of pre-cracked specimen of any geometry and size. However, it cannot predict the complete post peak response of the structure. Jenq and Shah two parameter model replaces an actual crack by an equivalent crack whose length is determined from the condition that its crack opening displacement (w) is equal to certain critical value w_c. This w_c displacement is defined as opening of the crack at initial crack tip of the traction free crack, that is at the beginning of inelastic zone. The criterion for crack propagation is expressed by two parameters (1) the critical value of the stress intensity factor of the equivalent LEFM crack tip, K_{Ic} and (2) w_c. The value of K_{Ic} from this model has been shown to be essentially independent of geometry of the specimen. RILEM technical Committee has proposed a recommendation to measure the fracture parameters K_{Ic} and w_c using a three point bend beam based on two parameter fracture model by Jenq and Shah **[Shah et. al. (1995)** and **Bazant** and **Planas (1998)]**. The critical stress intensity factor K_{Ic} is calculated as **[Shah et. al. (1995)]**:

$$K_{Ic} = 3(P_c + 0.5W_h)\frac{S\sqrt{\pi a_c}\, g_1\left(\frac{a_c}{D}\right)}{2D^2 t} \qquad \text{Eq. (5.14)}$$

Where P_c is the peak load, W_h is the self-weight of the beam and $g_1(a_c/D)$ is geometric function **[Shah et. al. (1995)]**. The critical crack tip opening displacement w_c is then calculated as **[Shah et. al. (1995)]**:

$$w_c = \frac{6(P_c + 0.5W_h)Sa_c g_2\left(\frac{a_c}{D}\right)}{ED^2 t}\left[(1-\beta)^2 + \left(1.081 - 1.149\frac{a_c}{D}\right)\left(\beta_0 - \beta_0^2\right)\right]^{0.5} \qquad \text{Eq. (5.15)}$$

Where $\beta = a/a_{\mathrm{c}}$ and $g_2(a_c/D)$ is another geometric function . Size effect has been explained by showing the dependency of structural strength on the structure size in the result's section. Further based on various regressions and Jenq-Shah model the fracture parameters are evaluated and discussed.

5.2 Results based on size effect studies

Another important objective of the present work involves the assessment of fracture parameters from Bazant size effect laws based on the analysis of linear regression I, linear regression II, weighted linear regression and Jenq-Shah model. There are two extremes of size-effect law: (i) strength criteria and (ii) LEFM size effect. The former yields no size effect and is only applicable for relatively small size structures. On the other hand, the latter shows the strong size effect and may only be used for relatively large size structures. A quasi-brittle material like concrete exhibits a transitional size effect between the two extremes of size effects. The experimental program **[Raghu Prasad (2009), Muralidhara (2010),** and **Muralidhara et. al. (2010)]** on displacement control test of geometrically similar concrete beams is utilized to perform the size effect studies. The parameters fracture energy (G_f), effective length of fracture process zone (c_f) and critical stress intensity factor (K_{Ic}) are estimated.

Fig. **5.1** illustrates the size effect of all beams cast with 12.5 mm and 20 mm maximum aggregate size for a/D = 0.25 and 0.33 using linear regression I. **Fig**. **5.2** shows the size effect of beams cast with 20 mm maximum aggregate size only for a/D = 0.25 and 0.33 using linear regression II. The size effect using the linear regression II for all beams cast with 12.5 mm and 20 mm maximum aggregate size for a/D = 0.25 is shown in **Fig**. **5.3**. The relationship between the failure stress and size of the structures for geometrically similar TPB beams using the linear regression I and II are shown in **Figs. 5.1-5.3**. **Figs. 5.1-5.3** predicts a transitional size effect showing the decrease of the fracture stress with increasing structure size.

Similarly the size effect based on weighted linear regression for a/D = 0.25 and 0.33 respectively is shown in **Figs**. **5.4a** and **5.5a**. **Fig**. **5.4b** and **Fig**. **5.5b** consist of horizontal line based on strength criterion showing no size effect and is only applicable for relatively small size structures. **Fig**. **5.4b** and **Fig**. **5.5b** consist of inclined line having slope -1/2, which is governed by the LEFM criterion, showing the strong size effect, and this criterion is only used for relatively large size structures. **Fig**. **5.4b** and **Fig**. **5.5b** shows the transition behavior of concrete beams for geometrically similar TPB beams having ligament size ranging from 94 mm to 750 mm in the present analysis.

The fracture parameters using the linear regression I and II of all the beams cast with 12.5 mm and 20 mm maximum aggregate size for a/D = 0.05, 0.25 and 0.33 are evaluated and shown in **Table 5.1**. Further the fracture parameters using the linear regression I and II of the beams for a/D = 0.05, 0.25 and 0.33 are evaluated separately for the concrete mix having 12.5 mm and 20 mm maximum aggregate size as shown in **Table 5.2**. The fracture parameters using the weighted linear regression are estimated and shown in **Table 5.3**. **Table 5.4** represents the estimated fracture parameters from RILEM recommendation based on Jenq-Shah model. **Fig. 5.6** depicts the fracture toughness (K_{Ic}) vs. a/D for Jenq-Shah model and linear regression I and II.

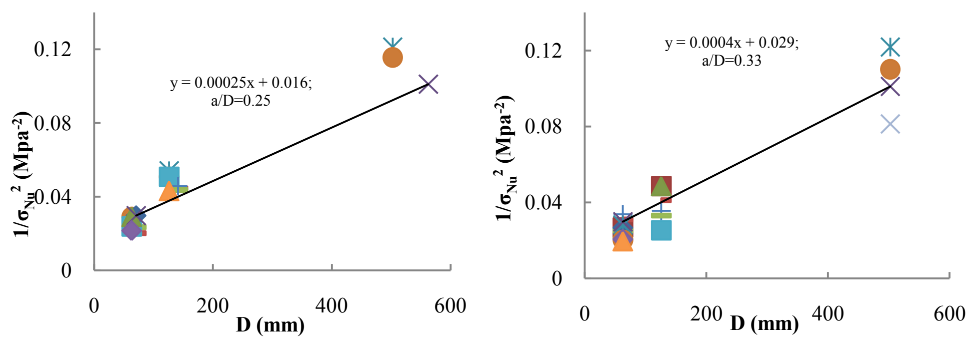

(a) (b)

Fig. 5.1 Size effect linear regression I: concrete beams cast with 12.5 and 20 mm aggregate size for (a) a/D =0.25 and (b) a/D = 0.33

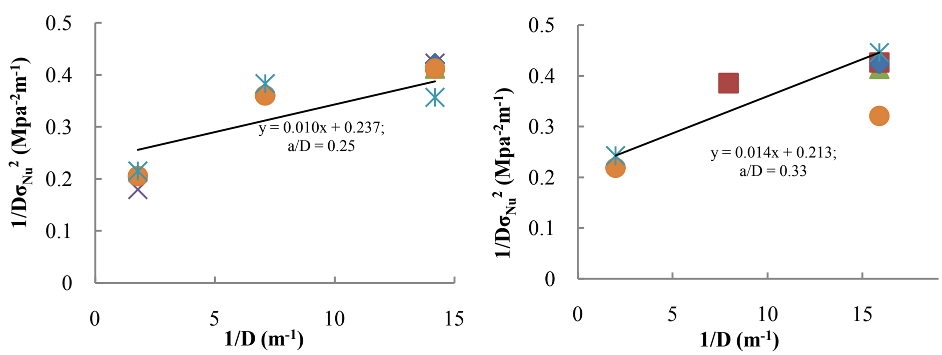

(a) (b)

Fig. 5.2 Size effect linear regression II plot: concrete beams cast with 20 mm aggregate size for (a) a/D =0.25 and (b) a/D = 0.33

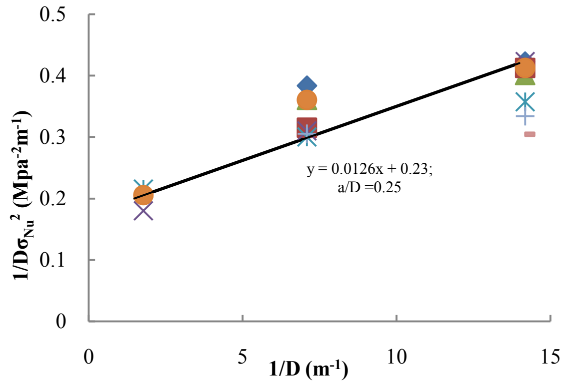

Fig. 5.3 Size effect linear regression II: concrete beams cast with 12.5 and 20 mm aggregate size for a/D =0.25

Table 5.1: Estimate of length of fracture process zone and fracture energy: Together concrete beams cast with 12.5 and 20 mm aggregate size

	Linear Regression-I					**Linear Regression-II**				
a/D	***A***	***C***	***K_{Ic} (Mpa-$m^{0.5}$)***	***G_f(N/m)***	***c_f(mm)***	***A***	***C***	***K_{Ic} (Mpa-$m^{0.5}$)***	***G_f(N/m)***	***c_f(mm)***
0.05	0.0001	0.002	1.903	145	3	0.001032	0.107	1.840	135	1.4
0.25	0.00025	0.016	1.729	119	12	0.012669	0.23	1.802	130	10.6
0.33	0.0004	0.029	1.676	112	14	0.023185	0.37	1.743	121	12

Table 5.2: Estimate of length of fracture process zone and fracture energy: Separate concrete beams cast with 12.5 and 20 mm aggregate size

		Linear Regression-I					**Linear Regression-II**				
a/D	***Aggregate size -mm***	***A***	***C***	***K_{Ic} (Mpa-$m^{0.5}$)***	***G_f(N/m)***	***c_f(mm)***	***A***	***C***	***K_{Ic} (Mpa-$m^{0.5}$)***	***G_f(N/m)***	***c_f(mm)***
0.05	20	0.0001	0.0007	1.903	145	1	0.0012	0.102	1.885	142	1.7
0.25		0.00027	0.0091	1.663	111	6.5	0.0127	0.25	1.729	120	9.7
0.33		0.0004418	0.018	1.594	102	7.8	0.0232	0.42	1.636	107	10.6
0.05	12.5	0.0000991	0.0008	1.912	146	1.2	0.0016	0.1	1.904	145	2.3
0.25		0.00025	0.008	1.729	120	6.2	0.0121	0.27	1.664	111	8.6
0.33		0.00043	0.017	1.616	105	7.6	0.021	0.39	1.697	115	10.3

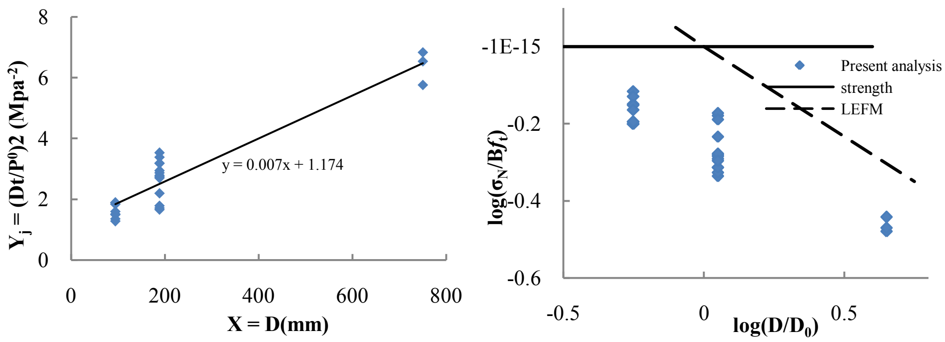

(a) (b)

Fig. 5.4 (a) Weighted linear regression and (b) Size effet from maximum load for a/D = 0.25

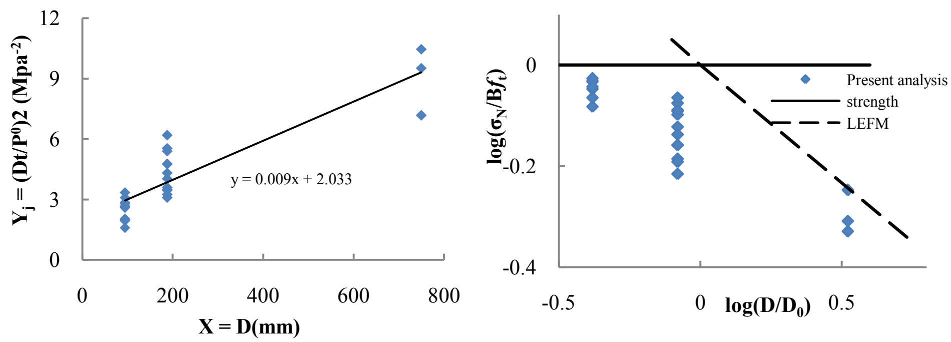

(a) (b)

Fig. 5.5 (a) Weighted linear regression and (b) Size effet from maximum load for a/D = 0.33

Table 5.3: Size effect parameters from weighted mean

	A_B	C_B	$G_f(N/m)$	$c_f(mm)$	ω_A	m
0.05	0.001	0.305	156	5	-	-
0.25	0.0057	1.174	105	13	0.18	0.16
0.33	0.009	2.033	110	14	0.16	0.14

Table 5.4: Fracture parameters from RILEM recommendation on Jenq-Shah model

Dimensions (mm)			*a/D*	a_c /D	K_{Ic} (Mpa $m^{1/2}$)	w_c (mm)	G_f (N/m)
S	D	t					
282	94	47	0.05	0.1595	1.5055	0.0147	68
282	94	47	0.05	0.1276	1.2430	0.0112	52
282	94	47	0.05	0.1340	1.3492	0.0120	58
282	94	47	0.25	0.4955	2.1339	0.0150	51
282	94	47	0.25	0.4860	1.9177	0.0143	46
282	94	47	0.33	0.6240	2.0851	0.0162	43
282	94	47	0.33	0.5497	1.6437	0.0137	38
282	94	47	0.33	0.5155	1.5234	0.0160	47
282	94	47	0.05	0.0744	1.1649	0.0089	72
282	94	47	0.25	0.4042	1.3420	0.0154	47
282	94	47	0.25	0.4860	1.7267	0.0180	52
282	94	47	0.33	0.5929	2.0748	0.0162	48
282	94	47	0.33	0.5513	1.7776	0.0150	44
282	94	47	0.33	0.5152	1.5975	0.0134	41
282	94	47	0.25	0.3923	1.5287	0.0138	51
282	94	47	0.25	0.4574	1.7484	0.0177	57
282	94	47	0.33	0.6096	2.5233	0.0149	51
282	94	47	0.33	0.5319	2.1494	0.0144	55
282	94	47	0.33	0.5050	1.7823	0.0125	44
282	94	47	0.05	0.1595	1.4183	0.0147	64
282	94	47	0.25	0.4042	1.3420	0.0157	48
282	94	47	0.25	0.4893	1.8733	0.0141	43
282	94	47	0.25	0.4310	1.4656	0.0130	38
282	94	47	0.33	0.6155	2.2074	0.0133	39
282	94	47	0.33	0.5785	2.2557	0.0120	41
564	188	94	0.05	0.0911	1.2639	0.0128	60
564	188	94	0.25	0.3450	1.3143	0.0131	38
564	188	94	0.25	0.4333	1.6981	0.0145	35
564	188	94	0.25	0.4548	1.8239	0.0169	40
564	188	94	0.33	0.4938	1.8198	0.0123	33
564	188	94	0.33	0.4784	1.6157	0.0127	32
564	188	94	0.33	0.4784	1.7990	0.0104	29
564	188	94	0.05	0.1755	2.0455	0.0169	70
564	188	94	0.05	0.1436	1.9154	0.0151	69
564	188	94	0.25	0.4127	1.4235	0.0177	39
564	188	94	0.25	0.5277	2.1269	0.0213	46
564	188	94	0.25	0.4548	1.8375	0.0179	43
564	188	94	0.33	0.6163	2.2547	0.0174	36
564	188	94	0.33	0.6027	1.9965	0.0169	33
564	188	94	0.05	0.1276	1.6549	0.0141	62
564	188	94	0.25	0.3327	0.9157	0.0148	32
564	188	94	0.33	0.4148	1.2341	0.0127	36
564	188	94	0.33	0.4487	1.3603	0.0111	28
564	188	94	0.25	0.4620	1.6768	0.0168	36
564	188	94	0.25	0.3686	1.3283	0.0116	29
564	188	94	0.33	0.5246	1.2009	0.0153	24
2250	750	375	0.25	0.5643	3.6027	0.0124	21
2250	750	375	0.25	0.4352	2.1931	0.0130	20
2250	750	375	0.25	0.4571	2.3897	0.0134	21
2250	750	375	0.33	0.4272	1.7354	0.0102	18
2250	750	375	0.33	0.6242	3.5279	0.0106	17

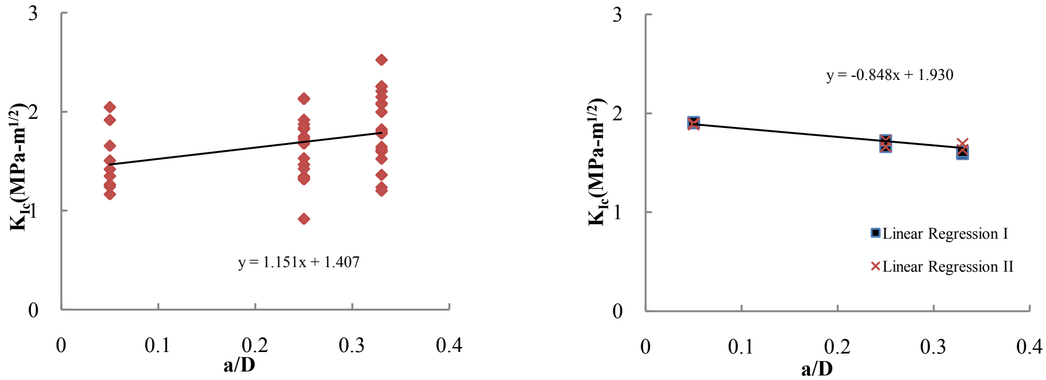

(a) (b)

Fig. 5.6 Fracture toughness (a) Jenq-Shah (b) Linear regression I and II

5.3 Chapter observations and closure

The fracture energy values (G_f) are observed to be in the range of 156 ~ 135 N/m, 105 ~ 130 N/m and 102 ~ 121 N/m for a/D =0.05, 0.25 and 0.33 respectively from Bazant size effect laws. The process zone lengths are found to be 1 ~ 3 mm, 6.5 ~ 12 mm and 7.6 ~ 14 mm for a/D =0.05, 0.25 and 0.33 respectively from Bazant size effect laws. The range of fracture energy value (G_f) is 102 ~ 130 N/m from a/D = 0.25 and 0.33. Also from the Jenq-Shah model, fracture energy value is found to be in range from 69 ~ 52 N/m, 20 ~ 51 N/m and 17 ~ 51 N/m for a/D =0.05, 0.25 and 0.33 respectively.

Size effect laws are derived based on assumption that the fracture energy dissipated at the failure is a smooth function of structural dimensions and size of FPZ. Therefore, size effect studies evaluates the size independent fracture energy in an approximate manner. This law describes the transition from the strength criterion for which there is no size effect to LEFM criterion for which the size effect is strong. An important advantage of the size effect method is that it yields not only the fracture energy of the material but also the effective length of the fracture process zone. The reason of size effect in concrete structures is due to the existence of large and variable length of FPZ ahead of the crack tip. FPZ depends on the specimen size and is strongly influenced by the proximity of the specimen boundary. Therefore, next chapter mainly deals with the investigation of characteristics of FPZ.

Chapter 6

FRACTURE PROCESS ZONE: OPTICAL CHARACTERIZATION

6.1 Digital Image Correlation (DIC) for optical characterization of Fracture Process Zone (FPZ)

In engineering structures, the strain measurements are extremely important because they help in investigating the full-fledged development of concrete fracture process zone. In-depth investigations are required to improve the study of the behavior of materials and structural components under mechanical loads. There exist various experimental methods such as holographic interferometry, the dye penetration, the scanning electron microscopy, the acoustic emission, etc to detect the fracture process **[Elices** and **Planas (1996), Shah et. al. (1995)**, **Shailendra** and **Barai (2011)]**. These methods provide the qualitative analysis on micro-features on concrete from which it is very difficult to detect the crack profile. Digital Image Correlation (DIC) experimental technique overcomes several limitations of the above-mentioned methods by providing detailed information on complex deformation states that lead to the initiation and propagation of fracture until complete failure. DIC technique is insensitive to massive rigid body motions, and can capture large deformations in a single measurement as long as the object remains in the field of view of the cameras **[Skarzynski** and **Tejchman (2010), Fayyad** and **Lees (2014),** and **Alam et**. **al**. **(2014)]**. DIC works on the principles similar to human depth perception by viewing the same object from different angles so that the precise shape of the object in three-dimensional space can be resolved. Digital images of the specimen are collected at pre-determined time intervals throughout the test out of which, the first image represents the un-deformed (reference) configuration. DIC considers the two digital images, first image taken before deformation (reference image) and the second image taken after the deformation, which represents the positions of an object at these moments. A small subset in the reference image, taken before deformation, is matched to a similar subset in the target image, taken after deformation. The idea behind the method is to infer the displacement and strain of the structure under the test by tracking the deformation of a random speckle pattern applied to the component's surface in digital images acquired during the loading.

DIC is an important non-intrusive experimental technique to measure the displacement and strain field. DIC has been successfully used for metals and composites. However, its utilization in concrete structures is very limited. In this work, DIC has been used to map the full field of displacement and strain for visualizing the fracture growth, fracture propagation and formation of Fracture Process Zone (FPZ) in notched concrete beams under bending. However, for the quantification of the concrete fracture properties, a new scheme called Optical Crack Profile (OCP) is developed as described in this chapter. The fracture parameters such as crack opening displacement, width of FPZ, length of FPZ and fracture energy of concrete structures are obtained by the OCP approach originated through DIC experiments.

6.1.1 Experimental details

The three sizes of geometrically similar (constant length to depth ratio) beams were cast, from the two different concrete mixes prepared using the maximum aggregate size of 12.5 mm and 20 mm for M45 concrete grade, at BARC-Tarapur site. The dimensions of geometrically similar beams designated as D1, D2 and D3 are as shown in **Table 3.2**. The cross section of the specimens was rectangular and beams were notched at mid-span. Initially the fracture tests were conducted on beams using the servo-hydraulic machine under closed-loop by **Raghu Prasad (2009)** and **Muralidhara (2010)**. DIC experiments on the concrete beams under displacement control mode in three point bend condition were performed. Images were captured using the camera with a resolution of 3840 X 2160 pixels. Further, the scheme of OCP technique was developed on plain concrete beam, which is one of the main objectives of the present study.

Stored images were processed using Vic-2D software, which has the option of pixel thresholding so that the computation of strain field over discontinuity or traction free zone can be prevented. The parameters such as critical crack opening displacement (w_c), the length of FPZ, width of FPZ, and fracture energy variation along the projected ligament are investigated using the OCP technique, which is not commonly available in the open literature.

6.1.2 Surface preparation and typical test setup on beam using DIC technique

The area of measurement was first sprayed with a white acrylic paint as shown in **Fig**. **6.1a**. Once the paint was dried, speckles were marked using a marker pen. The special care was taken to ensure that the size of the speckles was maintained uniformly and the speckles were random as clear from **Fig**. **6.1b**. A series of initial experiments were conducted on concrete beams to perfect the technique of DIC as is clear from **Fig**. **6.2**. The DIC technique based test setup of D2 beam using 500 kN capacity servo-hydraulic machine under crack mouth opening displacement control mode test is shown in **Fig**. **6.3a**. The notch to depth ratio, a/D is equal to 0.25 for this test. To quantify the fracture process zone of concrete, the visibility of clear speckles close to notch is important as shown in **Fig**. **6.3b**.

(a) (b)

Fig.6.1 Concrete surface with (a) acrylic paint (b) random speckles over the acrylic paint

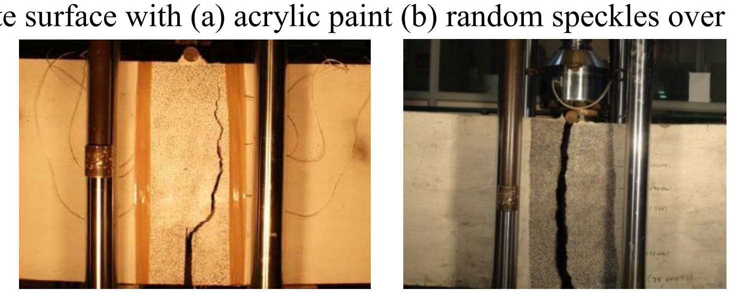

Fig.6.2 Trial test to perfect the DIC technique.

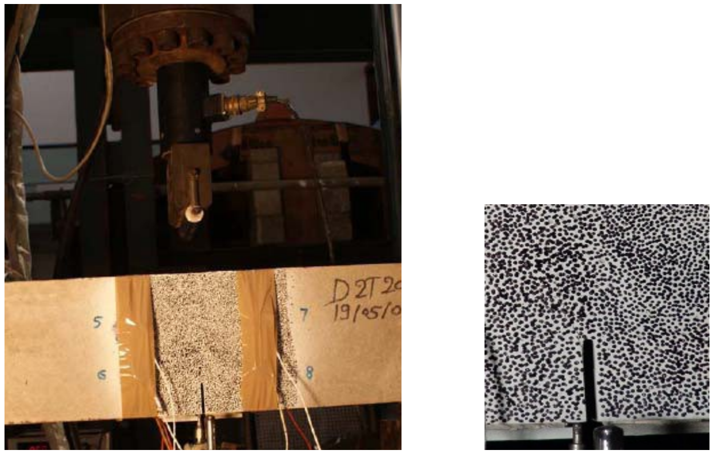

(a) (b)

Fig.6.3 D-2 beam with a/D =0.25: (a) Full beam test set up (b) Clear random speckles pattern

6.1.3 OCP methodology to investigate the width and length of Fracture Process Zone (FPZ) of concrete

The mode I crack propagation is investigated in the present study using OCP technique. FPZ in concrete is quite complex due to the development of both micro cracks and major cracks. FPZ consists of two regions - an inner strain-softening zone and an outer micro-fracture zone as reported by **Hu** and **Wittmann (2002)**. The size of FPZ is mostly governed by the strain softening of concrete in the inner strain-softening zone. The outer micro-cracks in fracture zone that are not interconnected and do not contribute to the concrete softening. The length of FPZ due to inner softening zone and outer micro-fracture zone is quantified at peak load and at various post peak loads using OCP technique.

Fig. 6.4 represents the lateral X and vertical Y axes close to the notch of concrete beam under displacement control test. The region selected for OCP is only shown in **Fig**. **6.4**. The crack growth starts at the tip of the notch toward the boundary of the beam. As is clear from **Fig**. **6.4** that the length and width of FPZ will be along vertical Y axis and lateral X axis respectively. **Fig. 6.5** illustrates the sketch of lateral X direction strain vs. lateral X axis i.e. perpendicular to the projected ligament, at critical/fracture load. The strain in the region ABG and CDE in **Fig. 6.5** is less than f_t/E which indicates the elastic regime or the presence of micro-cracks that are not inter-connected i.e. absence of concrete softening. The region BCEFG of **Fig. 6.5** show the strain is more than f_t/E indicating the softening zone of concrete governed by the complicated toughening mechanism which is responsible for FPZ. This scheme to identify FPZ is conceptualized for an idealized case wherein the main crack formation takes place above the notch, which normally could propagates along the vertical path of Y axis during post peak softening. However, the crack propagation, along the vertical path where micro-cracks have been formed, is at, times restricted due to presence of concrete aggregate resulting into aggregate interlock or aggregate shielding resulting in crack propagation on a deflected path as reported in the DIC experiment by Alam et. al. (2014). In view of this, a wider band above the notch was selected for strain mapping with DIC in the present experiment.

Fig. 6.6 illustrates the schematic sketches of lateral X direction strain vs. vertical Y axis, i.e. along the projected ligament, at critical load. The sketches TYZ and XYZ in **Fig. 6.6** are as per the idealized principle of fracture mechanics of homogeneous material, where the crack is free to propagate without any influence of aggregate and experimental observations with crack tunneling effect due to presence of aggregate due to concrete heterogeneity respectively. There exists an uncertain zone (i.e. OPYT) for FPZ identification close to the notch due to the aggregate interlock. The region X_1X_2 of **Fig. 6.6** indicating the softening zone of concrete, significantly contributes to the length of FPZ.

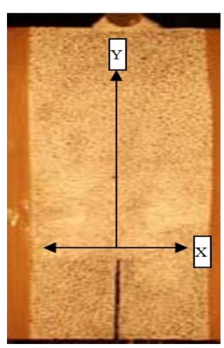

Fig. 6.4 Sketch showing lateral (X) and vertical (Y) axes

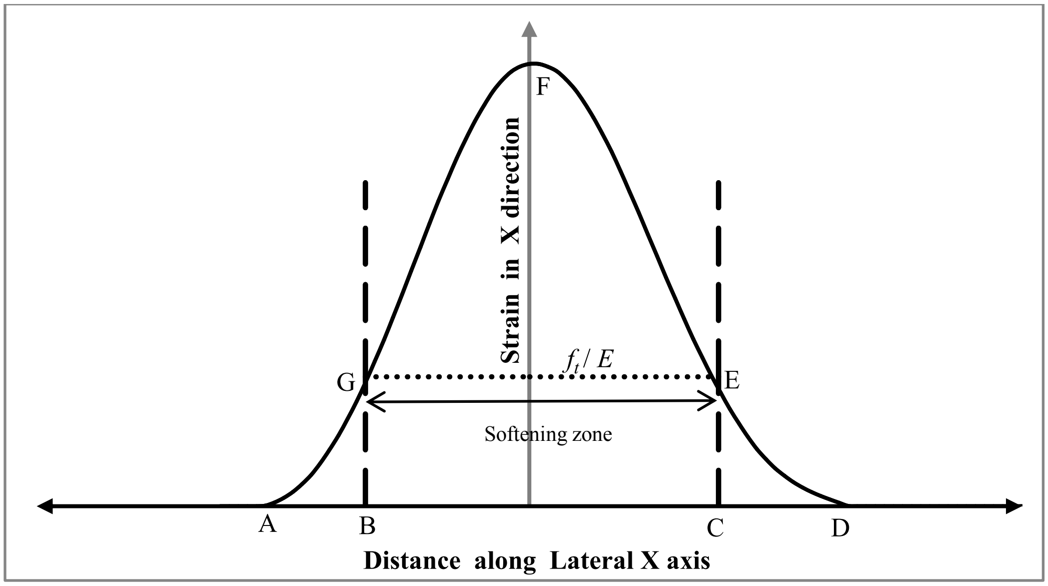

Fig. 6.5 New scheme to investigate the width of FPZ from the lateral X direction strain vs. lateral X axis

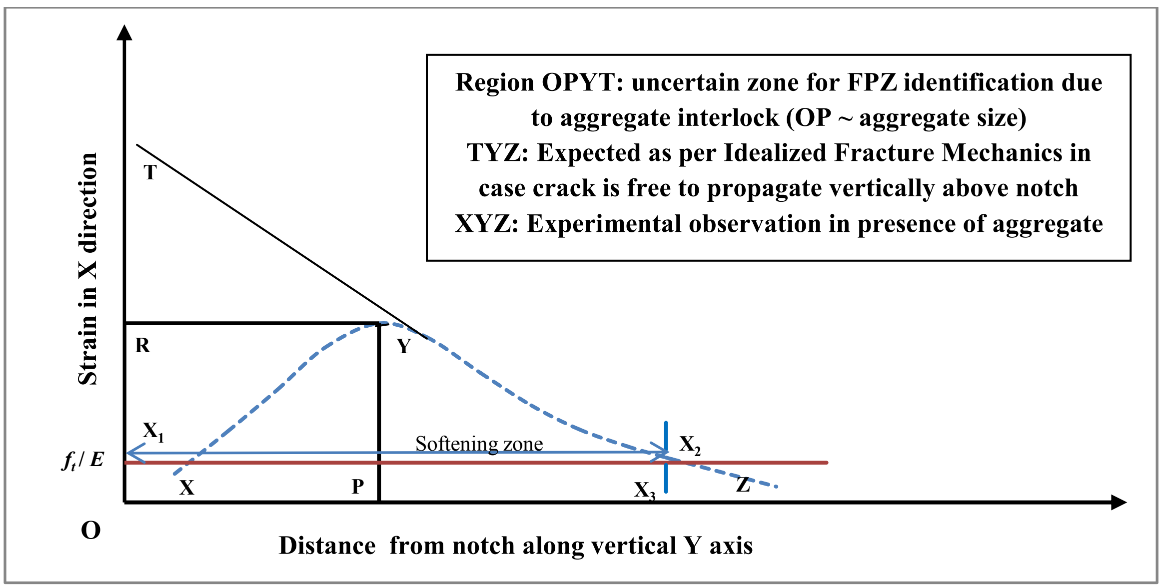

Fig. 6.6 New scheme to investigate the length of FPZ from the lateral X direction strain vs. vertical Y axis

6.1.4 OCP methodology for estimation of fracture energy

The correlation algorithm in VIC-2D [**Cintron** and **Saouma (2008)**] determines the location of each sub pixel in the surface of concrete beam marked with the random speckle pattern. It provides the displacement and strain fields on the surface of the specimen at different loading stages. Displacement fields enable to locate crack easily due to displacement discontinuity. Crack openings can be obtained from the displacement jump across the two sides of the crack **[Alam et. al. (2014)]**. The indirect way of strain integration over the width of FPZ also provides the crack opening displacement. The crack opening displacement *w*:

$$w = \int \varepsilon \, dl$$

where ε is the strain perpendicular to the crack growth direction.

FPZ transmit stresses due to the crack bridging effect of material heterogeneities **[Luigi** and **Gianluca (2008)]**. These bridging stresses (σ) are assumed to be a monotonically decreasing function of the crack opening displacements (w) in the FPZ as shown previously in **Fig**. **1.3**. The bulk material outside the FPZ is assumed to behave elastically. The softening curve shows the relationship between bridging stresses versus crack opening displacement. The area under the initial tangent of the softening curve represents the fracture energy which is governed by the failure/fracture load of concrete beam. As the crack grows the σ-w relation changes along the projected ligament. The crack growth along the projected ligament i.e. vertical Y axis is analyzed to estimate the crack opening displacement. At critical load the bridging stress is close to f_t. Using this, the σ-w relation at various stages of crack growth along the projected ligament is established from OCP technique. Thus, the approximate variation of fracture energy along the projected ligament using the concept of area under the initial tangent of the softening curve is estimated for D-2 beam and is discussed in the results.

6.2 Softening models

The constitutive laws that relates the cohesive/bridging stresses across the crack faces and the corresponding crack opening displacements, i.e., $\sigma = f(w)$ are known as softening functions. The assessment of the fracture behavior of a concrete structure is influenced by using different softening functions (σ-w). The cohesive stress (σ) and critical crack opening displacement (w_c)

are the fundamental properties required for FPZ of concrete. The cohesive stress is a monotonically decreasing function of crack opening displacement and it tends to close the crack. The value of σ is equal to material tensile strength f_t at the crack tip. The softening functions are based on the assumption that the energy (fracture energy ~ G_f) produced by the applied load is completely balanced by the material softening. The various softening functions (σ-w) such as linear, bilinear, exponential, nonlinear are available in the literature **[Shah et. al. (1995), Bazant** and **Planas (1998)**, and **Shailendra** and **Barai (2011)]**. The critical crack opening displacements (w_c) for linear, exponential, non linear, bilinear based on Petersson, Wittmann and CEB-FIP Model are expressed in **Table 6.1**.

Table 6.1: Softening functions

Type of Softening function	**Critical crack opening displacement, w_c**
Linear	$w_c = \frac{2G_f}{f_t}$
Exponential	$w_c = \frac{4.6517G_f}{f_t}$
Non linear	$w_c = \frac{5.136G_f}{f_t}$
Bilinear-I by Petersson	$w_c = \frac{3.6G_f}{f_t}$
Bilinear-II by Wittmann	$w_c = \frac{5G_f}{f_t}$
Bilinear-III by CEB-FIP Model Code	$w_c = \frac{6.475G_f}{f_t}$

6.3 Discussion of results

OCP analyzes a series of images of the D-2 beam having a random speckles pattern. These patterns monitored during the load application by a digital camera and stored in a computer in a digital format. These stored images are processed using the correlation algorithm in VIC-2D.

The parameters such as crack opening displacement, width and length of FPZ, strain profile and fracture energy value are evaluated. Further, the crack path is traced in the projected ligament at various post peak loads. The results are discussed subsequently as below:

6.3.1 Peak and post peak response: The main objective is to analyze the progression of cracking in the D-2 beam at different loading conditions. The overall response of the beam at different stages of fracture behavior is described in **Figs**. **6.7a-b**. **Figs**. **6.7a-b** represent the growth of strain in X direction (i.e. perpendicular to crack growth direction). The significant formation of FPZ occurs at locations where the strain value exceeds f_t/E. The strain, in the post peak region corresponding to softening, is orders of magnitude higher than f_t/E strain value. The beam portion, having non-violet colour and white colour corresponding to the strain levels higher than f_t/E, shows the spread of FPZ in **Fig**. **6.7a** and **Fig**. **6.7b** respectively very close to the notch. At peak load of 11.46 kN the strain close to the notch, where FPZ becomes prominent, is observed to be 810 με, which is well above f_t/E. At 78% of the post peak response with load of ~ 9 kN the strain level increases approximately by a factor of 2 with respect to the strain level observed at peak load. Further, at 52 % of the post peak response with load of ~ 6 kN, the strain level increases by a factor of 3 with respect to the strain level observed at peak load. However, there is not significant change in the size of FPZ. At 26% of the post peak response with load of ~ 3 kN and 9% of the post peak load the size of FPZ increases significantly. In addition, the strain levels at these loads are observed to be 7000 and 8000 με. Another important observation in Figs 6.7a-b is that though crack initiation and formation takes place above the notch in FPZ, but the crack propagation is observed along the inclined path showing the tunneling effect that indicates presence of aggregate. This is further described in the next paragraph.

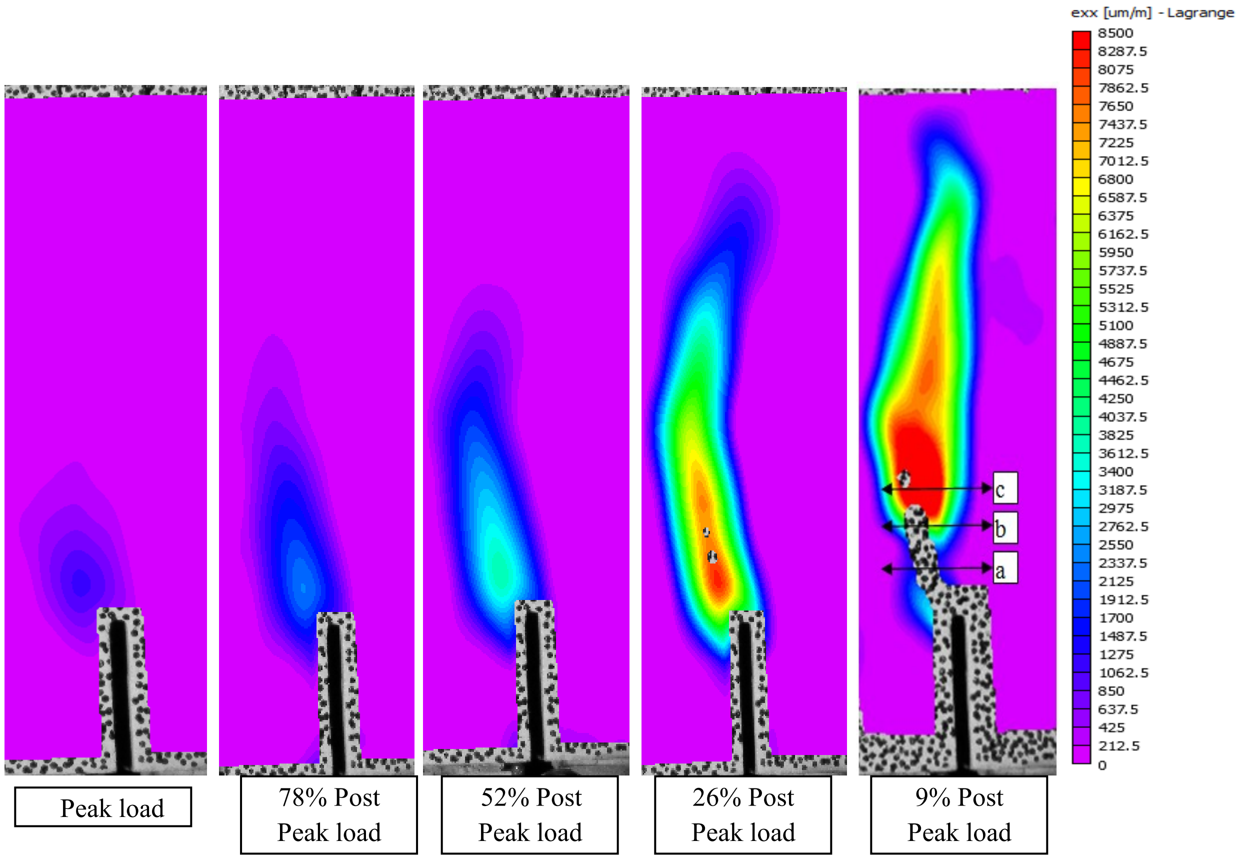

Fig.6.7 (a) Growth of peak strain in X direction

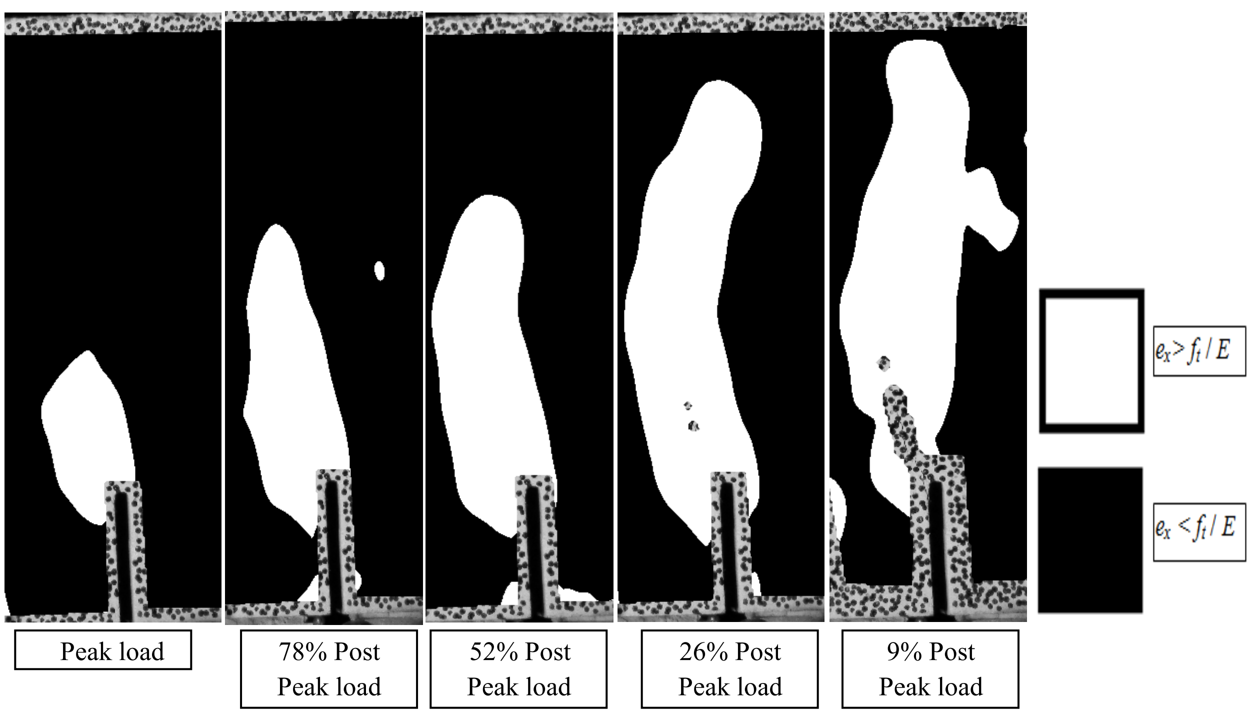

Fig.6.7 (b) Growth of strain in X direction conforming the formation of FPZ

6.3.2 Analysis of FPZ size and its comparison with the literature study: The growth of FPZ width and FPZ length in the different loading phase of peak and post peak response are evaluated. **Fig. 6.8a-b** illustrates the growth of length of FPZ at peak load and various post peak loads. The curves T'Y'Z' and TYZ in **Fig. 6.8a-b** are as per the idealized principle of fracture mechanics, wherein the crack should propagate along the vertical path just above the notch in the FPZ for a homogeneous material. The curves X'Y'Z' and XYZ in **Fig. 6.8a-b** are as per the present experimental observation of heterogeneous concrete material. There exist uncertain zones (i.e. OPYT and OQY'T') close to the notch due to the aggregate interlock or aggregate shielding resulting into crack tunnelling and the crack path is not aligned vertically along the notch. It may be noted from this graph that this uncertain zone size is around 25-30 mm, which is of the same order as the aggregate size of 20 mm used for casting this beam. From **Fig. 6.8a-b**, the length of FPZ is estimated using the proposed methodology as described in **Fig. 6.6**. **Table 6.2** presents the maximum local strain and length of FPZ length at peak load and various post peak loads. The fracture process zone becomes prominent at f_t/E strain and starts growing in size. The minimum local strain is 1124 με and 10000 με at peak load and 9% of post peak load respectively. The length of FPZ is observed to be in the range from 80-160 mm starting from peak load to 9% of the post peak load. In terms of aggregate size, the FPZ length falls in range from 4-8 times d_a where d_a is the maximum size of aggregate. Crack growth begins at the notch of D2 beam. Close to the notch, methodology as discussed above is implemented to estimate the width of FPZ. **Fig. 6.9** represents the X direction strain with the X axis. The FPZ width is found to be in range 25~33 mm. OCP results assess the width and length of FPZ to be 1.25-1.65d_a and 4-8d_a respectively. The lengths of FPZ are roughly 12d_a and FPZ width range is from d_a to 6d_a as reported **[ACI (1999)]**. The order of length and width of FPZ predicted using OCP is found to be in reasonable agreement with approximate value.

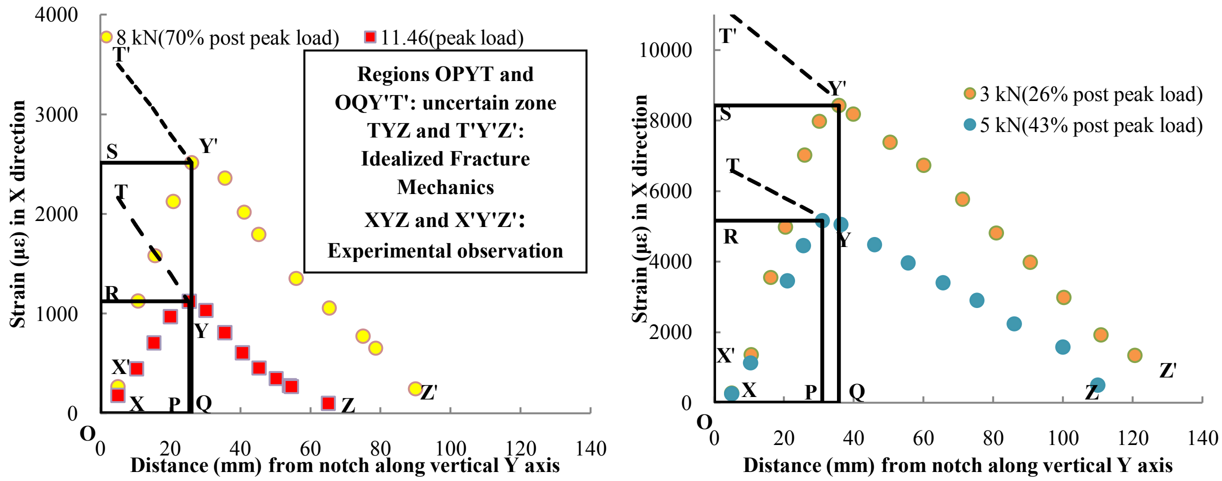

(a) (b)

Fig. 6.8 FPZ lengths: strain vs. vertical Y axis at (a) peak load and 70% of post peak load (b) 26% and 3% of the post peak load

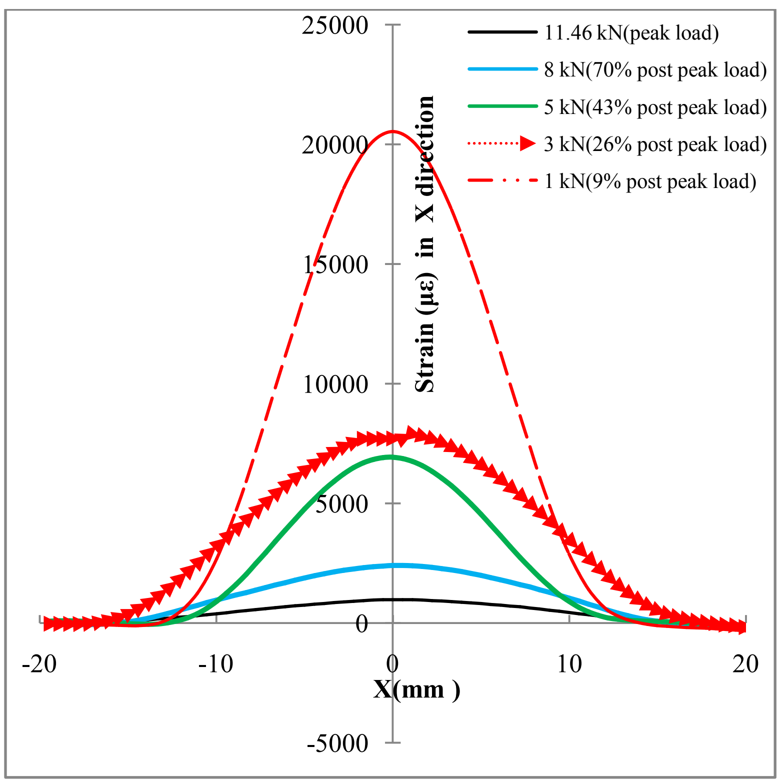

Fig. 6.9 FPZ width: Strain vs. lateral X axis at various post peak load

Table 6.2: Length of FPZ in the present study

Load(kN)	Maximum strain -με	FPZ full length-mm
11.46-peak	1101	80
9-post peak	2323	100
8-post peak	2616	110
6-post peak	3750	118
5-post peak	5116	138
4-post peak	6760	145
3-post peak	8523	151
2-post peak	9260	155
1-post peak	10249	160

The concrete properties and D2 beam size used in the present study are very similar to the reported study of **Alam et. al. (2014)**. Therefore, study by **Alam et. al. (2014)** is best suited for comparing the characteristics of FPZ with the present study. The comparison of lengths of FPZ, at peak load and various post peak loads (80%, 70%, 52%, 43%, 17% and 9%), predicted in the present study with the study of **Alam et. al. (2014)** are shown in **Table 6.3**. From **Table 6.3**, FPZ lengths at post peak loads predicted in the present study are found to be in reasonably good agreement with the study of **Alam et. al. (2014)**. However, at peak load there is some discrepancy, which may be perhaps due the aggregate interlock observed in the study of **Alam et. al. (2014)**. The width of FPZ at peak load is observed to be ~ 40 mm in the study of **Alam et. al. (2014)**, which is in reasonable agreement with the value of ~30 mm in the present study. In the similar way, the widths of FPZ at various post peak loads predicted in the present study (~ 40-50 mm) are observed to be in reasonably good agreement with the study (~50-60 mm) of **Alam et. al. (2014)**.

Table 6.3: Comparison of FPZ with the study of **Alam et. al. (2014)**

Load	**FPZ length (mm) in study of Alam et. al. (2014)**	**FPZ length (mm) in present study**
peak	37	80
80% post peak	88	100
70% post peak	100	110
52% post peak	120	118
43% post peak	126	138
17% post peak	130	155
9% post peak	145	160

6.3.3 Crack opening displacement and fracture energy and its comparison with the literature study: Fig. **6.7a** represents the location of investigating lines a, b, and c for assessment of crack opening displacement (w).The load data was also recorded during the experiments. Through OCP, the w during pre-peak and post-peak loads are estimated, at various investigating lines along Y-axis. Thus at every investigating lines, the plot of load (P) vs. crack opening displacement (w) is obtained showing pre-peak and post-peak response. For D2 beam, P vs. w plots for a, b, and c investigating lines are shown in **Fig. 6.10a**. The maximum load (P_c) corresponds to the bridging stress equal to the tensile strength of concrete **[Bazant** and **Planas (1998), Luigi** and **Gianluca (2008)]**. In other words, at this load, the cohesion/traction (σ) is maximum. After this, fracture propagation occurs and load starts reducing resulting in loss of traction. Here, load (P) vs. w plot for a, b, and c investigating lines is transformed to maximum traction/ bridging stress (σ) vs. w plot, in which σ is made equal to the tensile strength (f_t) of concrete at maximum load (P_c). At other loads, the bridging stress is made equal to: $\sigma = P \times (f_t/P_c)$. This is how cohesive law is developed as shown in **Fig. 6.10b**. Further, in the post-peak part of softening curve, shown in **Fig. 6.10b**, an initial tangent is plotted in a consistent manner to evaluate the fracture energy of concrete at one particular investigating line using the concept shown in **Fig. 1.3**. Similarly, at various investigating lines, fracture energy of concrete is evaluated. The fracture energy variation along the projected ligament is shown in **Fig. 6.10c** from which the average fracture energy value (G_f) is evaluated. Fracture energy value estimated based on optical crack profile scheme has been observed to be ~102 N/m. The average fracture energy obtained from OCP is found to be lower than the value of 136 N/m of **Table 4.4**. This is expected as explained in next section. In addition, the load vs. crack opening displacement (w) plot close to notch of the beam estimated through OCP, is compared with the experimental data of **Muralidhara et. al. (2010)** and reported study of **Alam et. al. (2014)** as shown in **Fig**. **6.11**. Using the linear, bilinear, exponential and non linear softening functions, critical crack opening displacements (w_c) are evaluated using two extreme values of fracture energy obtained through OCP and RILEM averaging approach as shown in **Table 6.4**. The experimentally observed values of w_c are in range from 0.03 ~ 0.04 mm as is clear from **Fig**. **6.11**. It is also clear from the **Table 6.4** that w_c estimated from liner softening are in reasonable agreement with value of 0.03 ~ 0.04 mm predicted from **Fig**. **6.11**. However, the prediction of w_c from the other softening model does not compare well with the prediction of **Fig**. **6.11**. This is perhaps due to the fact the initial tangent of softening curve represents the fracture energy which is governed by the failure load and is exactly similar to the linear softening model.

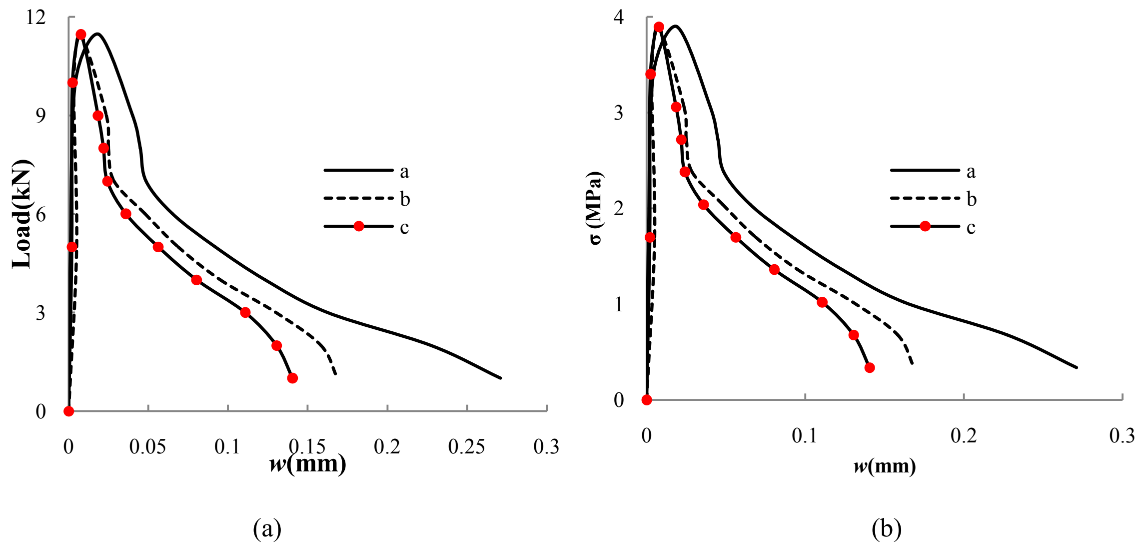

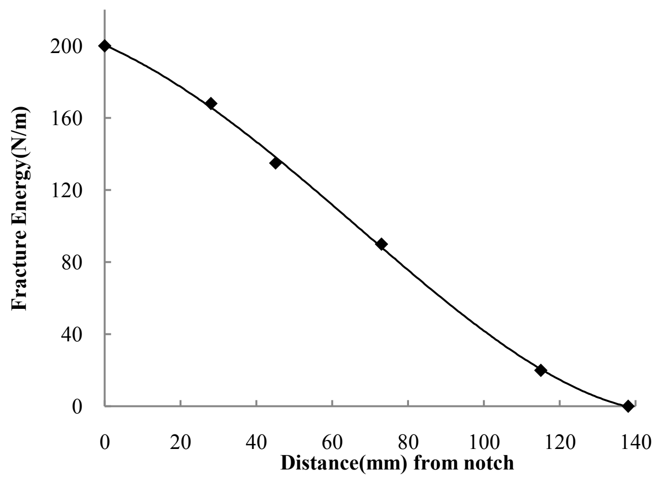

(c)

Fig. 6.10 (a) Load vs. *w* in reference lines a, b, c (please see Fig. 6.7e) (b) *σ*-*w* relation in reference lines a, b, c and (c) fracture energy variation along the projected ligament of D2 beam for a/D = 0.25

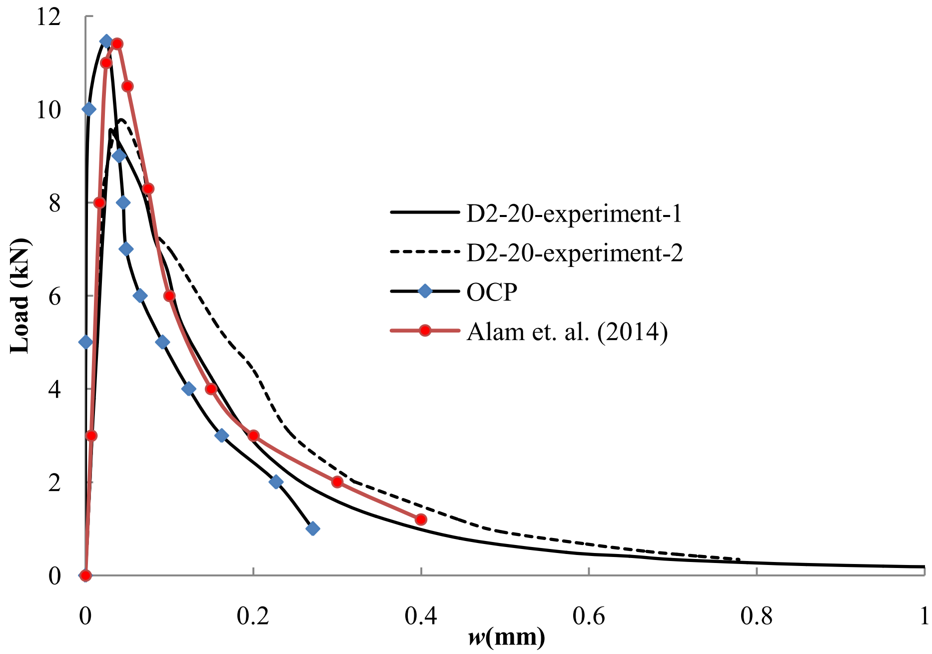

Fig. 6.11 Load-crack opening displacement (w)

Table 6.4: Critical crack opening displacements

Softening Law	w_c (mm) for G_f = 102 N/m	w_c(mm) for G_f = 136 N/m
Linear	0.058	0.077
Biliear-1	0.104	0.138
Biliear-1	0.145	0.192
Biliear-1	0.188	0.249
Exponential	0.135	0.179
Non linear	0.149	0.198

6.3.4 FPZ confirmation by strain gauge: The two strain gauges were mounted on the back surface of beam as shown in **Fig**. **6.12**. As the load reaches 50% of the peak load, the isolated and randomly distributed micro-cracks starts localizing. The localized zone, formed above the notch of beam at the peak load, is termed as FPZ. At peak load, high tensile strain of 1000 με is observed through strain gauge mounted at Location '1' as shown in **Fig**. **6.13**. FPZ begins to form above the notch at Location '1' and propagates toward the boundary. FPZ formed at peak load results in the fracture propagation, and further leading to the formation of large cracking zone at decreasing post peak load values. At peak load the fracture has not propagated to

Location '2'. Therefore, the tensile strain at peak load is found to insignificant at Location '2' as is clear from **Fig. 6.13**. As the load reduces during post peak softening, the fracture propagates toward Location '2', which is close to the boundary. The significant tensile strains of 500, 3500 and 4200 με are observed at decreasing loads of 5, 3 and 2 kN at Location '2' as shown in **Fig. 6.13**. This further confirms that tensile failure occurred almost up to the top of the beam.

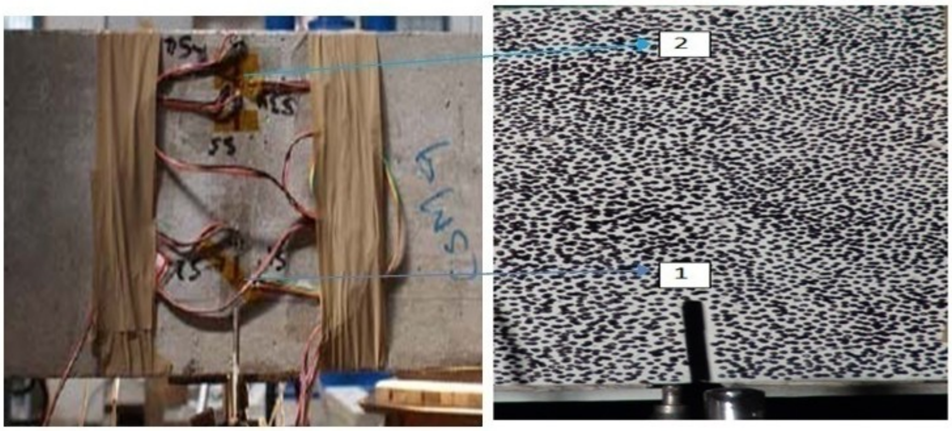

Fig. 6.12 Showing strain gauge location

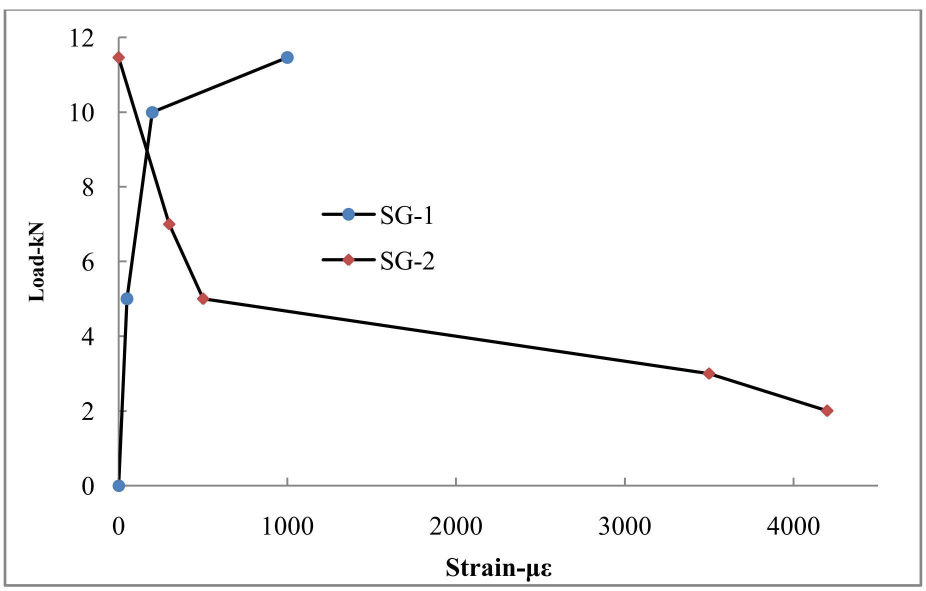

Fig. 6.13 Depicts the FPZ growth through the strain variation at location 1 and 2 with the load

6.4 Chapter closure

The Optical Crack Profile (OCP) technique is a very effective method to determine the strain field on the surface of concrete with a large accuracy and without any physical contact. The fracture propagation at peak and various post peak loads along the projected ligament of notched bam is captured using OCP. The propagation of FPZ captured using OCP is verified with conventional instrumentation approach using electrical resistance strain gauge and observed to be in reasonable agreement. The methodology to assess the length and width of Fracture Process Zone (FPZ), fracture energy, and crack opening displacement is investigated using OCP. The characteristics of FPZ is observed to be in agreement with guidelines of **ACI (1999)** report.

Chapter 7

THE SIZE INDEPENDENCE OF FRACTURE ENERGY AND INNOVATIVENESS IN THE PRESENT RESEARCH

The fracture energy values predicted through load deflection response of TPB concrete beams as per RILEM recommendation are beset with size effects. Therefore, the present research attempts to determine fracture energy that is independent of size. The fracture energy values obtained through the various methodologies are shown in **Table 7.**

Table 7: Fracture energy values from various methodologies

Approaches	**Fracture energy (N/m)**
Size effect law (Jenq-Shah)	20-51
Size effect laws (Bazant)	102-130
Bi-linear model	113-126
Presently developed relation of energy release rate	106-125
Presently developed methodology on averaging RILEM fracture energy	126-136
Optical characterization	102

In Jenq-Shah size effect law, the fracture energy values (20-51 N/m) are found to be very low because the post peak response of the structures is not accounted for. Bazant's size effect laws evaluate the fracture energy in range of 102-120 N/m, through the extrapolation of nominal strength of limited number of specimens by regression analysis. In an approximate way with various assumptions, Bazant's size effect laws evaluate the fracture energy that is independent of size in an overall average sense, which may further be improved for the exact assessment of size independent fracture energy by addressing the boundary effect with considerations of concrete cohesive laws, presence of FPZ in large characteristic dimensions/projected ligament, and load-deflection response of RILEM test for various notch to depth ratios.

The popular bi-linear model has been referred by various investigators, but the implementation of existing model equation for assessment of size independent fracture energy is not very commonly available in the open literature. On the basis of the boundary effect method using bi-linear model, the size independent fracture energy is found to be in the range of 113-126 N/m from the present set of specimens of M45 grade concrete.

Further, the three new schemes to assess size independent fracture energy and an advanced methodology for quantification of characteristics of FPZ are proposed in this work. Through the concept of energy release rate, the estimated size independent fracture energy is observed to be in a range of 106-125 N/m. The energy release rate method is valid beyond the test range (up-to 2000 mm of ligament size) and thus having an added advantage. Another approach based on averaging of RILEM fracture energy evaluates the size independent fracture energy in a range of 126-136 N/m and is simple to apply.

Fracture energy value estimated based on optical crack profile scheme has been observed to be ~102 N/m. This is relatively lower than values evaluated by other methods because the measurement area cannot be selected exactly near to the notch tip due to the experimental limitation. The uniqueness of optical approach is that the cohesive relation (traction separation law) is established to estimate the fracture energy. The quantification of FPZ characteristics and fracture energy assessment through optical scheme has not been carried out before in the open literature.

The bi-linear, energy release rate and fracture energy averaging methods and optical scheme are more sophisticated than the Bazant's size effect laws although the fracture energy values are not much different. It is, therefore, concluded that either method (except Jenq-Shah) can be used to obtain a unique value of the size-independent fracture energy of concrete due to consistent trend of fracture energy values evaluated by all the methods.

Chapter 8

SUMMARY, CONCLUSIONS AND FUTURE WORK

8.1 Summary and Conclusions

The fracture energy of concrete is an important material parameter in the numerical analysis of concrete structures which is investigated in the present work. The study presents robust techniques for the determination of characteristics of Fracture Process Zone (FPZ) and the size independent fracture energy (G_F) of concrete. The summary from the above study are as follows:

a) A number of numerical simulations of Three Point Bend (TPB) specimens have been performed through non-linear FEA by incorporating the concrete properties based on fracture energy softening model. The numerically observed necessary parameters for characterizing the concrete fracture such as maximum load, vertical displacement at maximum load, load-load line displacement and load-crack opening displacement responses are found to be in reasonably good agreement in most of the cases with the reported literature. Consequently, the computational approach is adopted for evaluating the parameters required to characterize the concrete fracture phenomenon since experimental approach is not always a practicable solution.

b) FEA of various TPB specimens for different a/D ratios is performed incorporating the fracture energy based softening model and the predicted response is observed to be mesh insensitive. Thus mesh sensitivity, which is an extremely important issue in concrete due to its post peak softening, has been addressed in this work.

c) Based on the completeness of interpolation function and discretization technique, the effectiveness of triangular elements is explained by considering the finite element simulations of TPB concrete specimens. The performance of triangular elements has been found to be superior to the quadrilateral elements for prediction of fracture response in notched TPB specimens.

d) RILEM fracture energy *(G_f)* values of concrete predicted through load-load line displacement curves are found to be size dependent. The size independent fracture energy (G_F) of concrete is investigated by the popular Hu and Wittmann bi-linear model. A new methodology is developed to assess G_F by averaging size dependent RILEM fracture energy values, over various a/D values for geometrically similar beams. The relationship between fracture energy release rate and uncracked ligament is developed. Using the developed relationship, the size independent fracture energy of concrete is also evaluated. Thus G_F is investigated from two presently proposed methods in this study and one existing method.

e) The Optical Crack Profile (OCP) technique evolved in this study is very effective to determine the strain field on the surface of concrete with a large accuracy and without any physical contact. The fracture propagation and progression of cracking at peak and various post peak load along the projected ligament of notched bam is captured using OCP. The propagation of FPZ captured using OCP is verified with conventional approach of strain gauge and observed to be in reasonable agreement. The methodology to assess the length and width of FPZ, fracture energy, and crack opening displacement is investigated using OCP. The characteristics of FPZ obtained through OCP are observed to be in agreement with the ACI guideline.

f) The fracture energy value obtained from OCP is found to be lower than those obtained by other methods (see **Table 4.4**) as measurement area cannot be very near to the notch tip due to the experimental limitation. Two extreme values of fracture energy obtained through OCP and RILEM averaging approach are utilized in various softening functions to estimate the values of w_c. In addition, the load-crack opening displacement response predicted using OCP is observed to be in agreement with reported experiment **[Muralidhara et. al. (2010)]**. It is observed that the OCP technique provides detailed information on the initiation and propagation of fracture until complete failure.

g) The size effect studies based on Bazant size effect laws (linear regression I, linear regression II, weighted linear regression) and Jenq-Shah model are performed. The parameters such as fracture energy, effective length of fracture process zone and critical stress intensity factor are estimated from these size effect laws. A comparative analysis of fracture energy values based on various model is done. It is concluded that any method (except Jenq-Shah) can be used to obtain a unique value of the size independent fracture energy of concrete.

8.2 Scope for further research

1. Develop the improved experimental methods for evaluating the size independent fracture energy of concrete.

2. Application of concrete fracture parameters in analysis and design of concrete structures.

3. Assessment of fracture process zone for reinforced concrete structures.

4. Quantification of material damage parameter using optical crack profile and acoustic emission technique.

BIBLIOGRAPHY

A

Abdalla. H. M and Karihaloo. B. L. 2004. A method for constructing the bilinear tension softening diagram of concrete corresponding to its true fracture energy. Magazine of Concrete Research. Vol. 56. No. 10. pp. 597–604.

ACI Committee 446 Report. 1999. Fracture Mechanics of Concrete: Concepts, Models and Determination of Material Properties. Chairman: Bazant Z. P.

Alam S. Y, Saliba Jacqueline and Loukili Ahmed. 2014. Fracture examination in concrete through combined digital image correlation and acoustic emission techniques. Construction and Building Materials. Vol. 69. pp. 232-242.

B

Bangash M. Y. H. and Telford Thomas. 2001. Manual of numerical methods in concrete.Thomas Telford Publishing Ltd.

Bazant Z. P. 1985. Fracture mechanics of concrete: Structural application and numerical calculation. Martinus Nijhoff Publishers.

Bazant Z. P. and Oh B. H. 1988. Crack band theory for fracture of concrete. Materials and Structures. Vol. 16. pp. 155-177

Bazant Z. P and Ozbolt J. 1989. Nonlocal Microplane Model for Fracture, Damage and Size Effect in Structures. Center for Advanced Cement-Based Materials. Northwestern University. Evanston. Report 89-10/498n.

Bazant Z. P and Planas J. 1998. Fracture and Size Effect in Concrete and other Quasi-brittle Materials. CRC Press. Florida.

C

Cedolin Luigi and Cusatis Gianluca. 2008. Identification of concrete fracture parameters through size effect experiments. Cement & Concrete Composites. Vol. 30. pp. 788-797.

Cifuentes H, Alcalde M and Medina F. 2013. Measuring the size-independent frcature energy of concrete. An Int. Journal of Experimental Mechanics. Vol. 49. pp. 54–59.

Cintron Rommel and Saouma Victor. 2008. Strain Measurements with the Digital Image Correlation System Vic-2D. Department of Civil Environmental and Architectural Engineering. University of Colorado.

Cook R. D, Malkus D.S, Plesha M. E. and Witt R. J. 2007. Concepts and Applications of Finite Elements Analysis. John Wiley & Sons Publishing Ltd. Fourth Edition.

D

Duan Kai, Hu Xiaozhi and Wittmann F.H. 2003. Boundary effect on concrete fracture and non-constant fracture energy distribution. Engineering Fracture Mechanics. Vol. 70. pp. 2257-2268.

E

Elices Manuel and Planas Jaime. 1996. Fracture Mechanics Parameters of Concrete. Advanced Cement based Materials. Vol. 4. pp. 116-127.

F

Fayyad Tahreer M. and Lees Janet M. 2014. Application of Digital Image Correlation to reinforced concrete fracture. Procedia Materials Science. Vol. 3. pp. 1585 – 1590.

G

Griffith. A.A. 1920. The phenomena of rupture and flow in solids. Philosophical Transactions. Series A. Vol. 221. pp. 163 – 198.

Gencturk Bora, Hossain Kazi, Kapadia Aadit, Labib Emad, Mo Yi-Lung. 2014. Use of digital image correlation technique in full-scale testing of prestressed concrete structures. Measurement. Vol. 47. pp. 505-515.

H

Hanson James H, Ingraffea Anthony R. 2003. Using numerical simulations to compare the fracture toughness values for concrete from the size-effect, two-parameter and fictitious crack models. Engineering Fracture Mechanics. Vol. 70. pp. 1015-1027.

Hillerborg A, Modeer M, Petersson P. E. 1976. Analysis of crack formation and crack growth in concrete by means of fracture mechanics and finite elements. Cement Concrete Research. Vol. 6. pp. 773-782.

Hoover G. Christian, Bazant Z. P, Vorel Jan, Wendner Roman and Hubler H. Mija. 2013. Comprehensive Concrete Fracture Tests: Description and Results. Engineering Fracture Mechanics. Vol. 114. pp. 92-103.

Hoover G. Christian and Bazant Z. P . 2013. Comprehensive concrete fracture tests: Size effects of Types 1 & 2, crack length effect and postpeak. Engineering Fracture Mechanics. Vol. 110. pp. 281-289.

I

Irwin. G.R. 1948. Fracture Dynamics. Fracturing of Metals. American Society for Metals. Cleveland. pp. 147 – 166.

K

Karihaloo. B. L. 1995. Fracture Mechanics and Structural Concrete (Concrete Design and Construction Series). Longman Pub Group.

Karihaloo B. L, Abdalla H.M. and Imjai T. 2003. A simple method for determining the true specific fracture energy of concrete. Magazine of Concrete Research. Vol. 55 No 5.pp. 471–481.

Karihaloo B. L, Abdalla H.M. and Xiao Q.Z. 2003. Size effect in concrete beam. Engineering Fracture Mechanics. Vol. 70. pp. 979–993.

Karihaloo B. L, Abdalla H.M. and Xiao Q.Z. 2006. Deterministic size effect in the strength of cracked concrete structures. Cement and Concrete Research. Vol. 36 pp. 171–188.

Karihaloo B. L, Murthy A. Ramachandra, and Iyer Nagesh R. 2013. Determination of size-independent specific fracture energy of concrete mixes by the tri-linear model. Cement and Concrete Research. Vol. 49. pp. 82-88.

Kim Jin-Keun, Yun Lee and Yi Seong-Tae. 2004. Fracture characteristics of concrete at early ages. Cement and Concrete Research. Vol. 34. pp. 507–519.

Koji Otsuka. Hidehumi Date. 2000. Fracture process zone in concrete tension specimen. Engineering Fracture Mechanics. Vol. 65.pp. 111-131.

Kozicki Jan and Tejchman Jacek. 2007. Experimental Investigations of Strain Localization in Concrete using Digital Image Correlation (DIC) Technique. Archives of Hydro-Engineering and Environmental Mechanics. Vol. 54. No. 1. pp. 3–24.

Kumar Mehta, P. Monteiro and Taulo J.M. 1997. Concrete Microstructure Property and Materials. McGraw-Hill, Third Edition.

Kumar Shailendra and Barai V. Sudhirkumar. 2011. Concrete fracture models and applications. Springer-Verlag Berlin Heidelberg.

M

Muralidhara S. 2010. Fracture energy and process zone in plain concrete beams. PhD dissertation, Indian Institute of Science, Banglore.

Muralidhara S, Raghu Prasad B.K, Eskandari Hamid and Karihaloo B. L. 2010. Fracture process zone size and true fracture energy of concrete using acoustic emission. Construction and Building Materials. Vol. 24. pp. 479-486.

Muralidhara S, Raghu Prasad B.K, Singh R. K. 2013. Size independent fracture energy from fracture energy release rate in plain concrete beam. Engineering Fracture Mechanics. Vol. 98. pp. 284-295.

R

Raghu Prasad B. K. 2009. Experimental evaluation of fracture properties of concrete. Interim progress report under Collaborative research project between BARC and Indian Institute of Science, Banglore.

Ragip Ince. 2004. Prediction of fracture parameters of concrete by Artificial Neural Networks. Engineering Fracture Mechanics. Vol. 71. pp. 2143–2159.

Roesler Jeffrey, Paulino Glaucio H. and Park Kyoungsoo. 2007. Cristian Gaedicke. Concrete fracture prediction using bilinear softening. Cement & Concrete Composites. Vol. 29. pp. 300–312.

S

Sancho J.M, Planas J, Cendon D. A, Reyes E. and Galvez J. C. 2007. An embedded crack model for finite element analysis of concrete fracture. Engineering Fracture Mechanics. Vol. 74, pp.75-86.

Shah S. P, Swartz Stuart E. and Ouyang Chengsheng. 1995. Application of fracture mechanics to concrete, rock and other quasi-brittle materials. Wiley Interscience. New Jersey. U.S.

Singh R. K, Basha S. M, and Singh Rajesh K. 2009. Fracture Energy and Size Effect Studies for Nuclear Concrete Structures. Proc. SMiRT-20, Espoo, Espoo, Finland.

Skarzynski L and Tejchman J. 2010. Calculations of fracture process zones on meso-scale in notched concrete beams subjected to three-point bending. European Journal of Mechanics A/Solids. Vol. 29. pp. 746-760

Sundara K. T, Iyengar Raja, Raghu Prasad B. K, Nagaraj T. S. and Patel Bharti. 1996. Parametric sensitivity of fracture behaviour of concrete Fracture Mechanics Parameters of Concrete. Nuclear Engineering and Design. Vol. 163. pp. 397-403.

T

Trivedi N. and Singh R. K. 2013. Prediction of Impact Induced Failure Modes in Reinforced Concrete Slabs through Nonlinear Transient Dynamic Finite Element Simulation. Annals of Nuclear Energy. Vol. 56. pp. 109-121.

W

Wittmann. F. H. 2002. Crack formation and Fracture Energy of normal and high strength concrete. Sadhana. Part-4. Vol. 27. pp. 413-423.

Z

Zhimin Wu. Shutong Yang, Xiaozhi Hu and Jianjun Zheng. 2006. An analytical model to predict the effective fracture toughness of concrete for three-point bending notched beams. Engineering Fracture Mechanics. Vol. 73. pp. 166–2191.

Zienkiewicz O. C. and Taylor R. L. 2000. The Finite Element Method: The Basis. Butterworth Heinemann Publishing Ltd. Vol. 1. Fifth edition.